Lehrstuhl für Elektrische Energiespeichertechnik
Fakultät für Elektrotechnik und Informationstechnik
Technische Universität München

Practical feasibility of Kalman filters for the state estimation of lithium-ion batteries

Dipl.-Ing. Univ. Christian Campestrini

Vollständiger Abdruck der von der Fakultät für Elektrotechnik und Informationstechnik der Technischen Universität München zur Erlangung des akademischen Grades eines

Doktor-Ingenieurs (Dr.-Ing.)

genehmigten Dissertation.

Vorsitzender:		Prof. Dr. Jörg Conradt
Prüfer der Dissertation:	1.	Prof. Dr.-Ing. Andreas Jossen
	2.	Prof. Dr.-Ing. Jürgen Götze

Die Dissertation wurde am 12.06.2017 bei der Technischen Universität München eingereicht und durch die Fakultät für Elektrotechnik und Informationstechnik am 05.11.2017 angenommen.

Vorwort und Danksagung

Die vorliegende Dissertation basiert auf den Erkenntnissen, die ich während der Bearbeitung der Projekte FORELMO und MiBZ zwischen August 2012 und Juni 2017 am Lehrstuhl für Elektrische Energiespeichertechnik der TU München gewinnen konnte.

Zuerst möchte ich mich besonders bei meinem Doktorvater, Prof. Dr.-Ing. Andreas Jossen, bedanken, der mir die Promotion ermöglichte und mich wissenschaftlich betreute. Zudem gilt mein Dank Prof. Dr.-Ing. Jürgen Götze für das Erstellen des Zweitgutachtens.

Neben der Unterstützung meines Doktorvaters erfuhr ich im Rahmen meiner wissenschaftlichen Tätigkeit und meinen Publikationen viel Rückhalt durch meine Arbeitskollegen:
Zunächst gilt mein Dank hierbei Martin Brand und Alexander Rheinfeld für die Beantragung der beiden Projekte, durch die mein Forschungsvorhaben ermöglicht wurde. Des Weiteren danke ich Max Horsche und Ilya Zilbermann für die Zusammenarbeit beim Erstellen des synthetischen Fahrprofils, Thomas Heil für die mathematische Beratung zum Thema Kalman Filter und Simon Schuster für die fachlichen Gespräche über Alterungseffekte von Lithium-Ionen-Batterien. Ich möchte mich auch bei Peter Keil bedanken, der mich mit zusätzlichen Messdaten und Batterien versorgte sowie bei Stephan Kosch für die vielen fachlichen Diskussionen.

Ein besonderer Dank gilt Korbinian Schmidt für die technische Unterstützung, die beim Durchführen der Messungen auf Modulebene sehr hilfreich war. Auch bei Ralph Karl, der mich beim Modulbau unterstützt hat, möchte ich mich bedanken.

Für das kritische Feedback und die letzten Anmerkungen zu meiner Dissertation gilt mein Dank Ilya Zilberman, Georg Walder, Kamyar Makinejad, Hristo Hristov und Daniel Nitz. Ebenso bedanke ich mich bei Nicola Doubleday für den sprachlichen Feinschliff der Arbeit.

Abschließend möchte ich mich an dieser Stelle auch bei meiner Familie, meinen Freunden und meiner Frau Kathrin Campestrini für den erholsamen Ausgleich und die motivierenden Gespräche bedanken.

München, 22.01.2018 Christian Campestrini

Kurzfassung

Eines der Hauptprobleme für die gehemmte Akzeptanz von Elektrofahrzeugen ist die geringe Reichweite. Um diese zu erhöhen, sind bezüglich der eingesetzten Lithium-Ionen-Batterien nicht nur elektrochemische Verbesserungen notwendig, es bedarf auch einer genaueren Zustandsschätzung. Durch eine exaktere Bestimmung des Batteriezustandes kann die Ausnutzung der Batterie erhöht werden, z. B. durch berechnen des Ladezustands basierend auf der aktuellen Kapazität und nicht auf der nominalen, oder durch verwenden des Ladezustandes als Abbruchkriterium beim Laden und Entladen anstatt der Zellspannung.

Die Literatur stellt für diese nicht direkt messbaren Zustände verschiedene Algorithmen zur Verfügung, wobei der Kalman Filter eine weit verbreitete Methode der Zustandsschätzung ist. In bisherigen Studien wird der Kalman Filter unter Laborbedingungen meist nur bei einer bestimmten Temperatur und bei Laufzeiten von wenigen Stunden untersucht. In der Praxis jedoch, muss der Algorithmus innerhalb eines weiten Temperaturbereichs und über mehrere Jahre hinweg zuverlässig und genau arbeiten. Deshalb ist das Ziel dieser Arbeit, die praktische Umsetzbarkeit des Kalman Filters auf Zell- und Modulebene zu untersuchen.

Um notwendige reale Testbedingungen zu bestimmen, wird das Batterieverhalten auf Abhängigkeiten von Temperatur, Ladezustand, Strom und Alter hin untersucht. Basierend auf diesem Batterieverhalten wird eine generische Validierungs- und Bewertungsmethode vorgestellt, die Algorithmen bei verschiedenen Temperaturen und Lastdynamiken testet. Um reale Bedingungen zu schaffen, werden die Daten für die Validierung von einem Batterie Management System gemessen.

Anhand dieser Methode werden verschiedene Kalman Filter verglichen, wobei der Fokus auf den variierenden Modellparametern liegt. Es wird eine sehr starke Abhängigkeit der Schätzperformanz von den Parametern gezeigt, die wiederum durch Filtereinstellungen beeinflusst werden kann. Diese Einstellungen beschreiben die nicht konstanten und nicht linearen Modellunsicherheiten und müssen empirisch für alle Zellzustände bestimmt werden. Beim Vergleich verschiedener Kalman Filtertypen, konnten keine relevanten Abweichungen festgestellt werden.

Neben den Modellparametern zeigt die aktuelle Forschung auch alterungsbedingte Veränderungen der Ruhespannungskennlinie, die die Referenz für den Kalman Filter darstellt. Die Auswirkung der Veränderung auf die Zustandsschätzung wird jedoch nicht gezeigt. Zu diesem Zweck wird in dieser Arbeit eine Untersuchung mit unterschiedlich gealterten Zellen durchgeführt. Dabei wird beobachtet, dass der Einfluss der Ruhespannung auf die Schätzperformanz mit steigendem Alter der Zellen zunimmt. Dieser Effekt wird bei niedrigen Temperaturen

noch weiter verstärkt. Um die Schätzperformanz zu verbessern, können beide Abhängigkeiten wiederum empirisch durch die Filtereinstellungen beeinflusst werden.

Des Weiteren wird eine Alterungsstudie auf Zell- und Modulebene durchgeführt, um diese Veränderungen der Ruhespannung genauer untersuchen zu können. Dabei soll die Untersuchung auf Modulebene die Skalierbarkeit der Alterung und somit der Zustandsschätzung zeigen. Auf Zellebene wird eine ladezustandsabhängige Veränderung der Ruhespannung beobachtet, die unabhängig von der Alterung ist, aber mit der Kapazitätsabnahme korreliert. Werden die Ruhespannungen der gealterten Zellen und Module verglichen, zeigen sich auf beiden Ebenen ähnliche Veränderungen. Somit kann die Skalierbarkeit der Alterung bestätigt werden.

Das Fazit dieser Arbeit ist, dass der Kalman Filter in der Praxis nicht ohne Weiteres zur Zustandsschätzung von Lithium-Ionen-Batterien verwendet werden kann. Die nicht konstanten Modellparameter und die alterungs- sowie temperaturabhängige Ruhespannung erfordern jeweils eine empirische Anpassung der Filtereinstellungen. Somit ist die Performanz des Kalman Filters in der realen Anwendung verglichen mit dem Laborbetrieb mit seinen sehr eingeschränkten Bedingungen wesentlich geringer.

Abstract

One of the central topics regarding the reduced market acceptance of electric vehicles is the limited driving range compared to conventional vehicles with combustion engines. To increase the driving range, whilst optimising of the electrochemical attributes of lithium-ion cells the state estimation also has to be improved. As a result of a more accurate state estimation, the utilisation of a cell can be increased e. g. by calculating the state of charge based on the actual cell capacity and not the nominal value, or by considering the state of charge as abort criterion during charging and discharging and not the cell voltage.

In literature many algorithms for the un-measurable states are presented, wherein the Kalman filter is one of the most common methods. In recent studies, only the short-term behaviour over several hours, at mostly one temperature, under laboratory conditions has been tested. However, in real applications, the Kalman filter has to perform within a wide temperature range reliably and accurately over several years. On account of this, the aim of this thesis is to investigate the practical feasibility of the Kalman filter at the single cell and module level.

To identify required test conditions the cell behaviour is investigated regarding temperature, state of charge, current and ageing dependencies. Based on the cell behaviour a generic validation and benchmark method is presented for testing algorithms at different temperatures and load dynamics. For a realistic test environment the measurement data for the validation is provided by a battery management system.

The focus of the performed Kalman filter comparison study is the variable cell model parameters. Here, a strong influence of the parameters on the estimation performance is shown, whereby the estimations are further influenced by the filter tuning. The tuning parameters describe the inconstant, non-linear model uncertainties and are to determine for all conditions empirically. Relevant deviations between different Kalman filter implementation are not observed.

In addition to the model parameters recent research also observes a change in open circuit voltage over lifetime. Therefore, the open circuit voltage represents the reference for the Kalman filter. However, the influence of these changes on the state estimation is not shown. Thus, an investigation with cells in different ageing states is performed. It is shown that the influence of the open circuit voltage on the state estimation increases with the progression of ageing. This effect is enhanced at low temperatures. To improve the estimation performance both dependencies can be influenced by the filter tuning.

For a more detailed investigation into the change in open circuit voltage over lifetime, an

ageing study at the single cell and module level is performed. In this context, the module ageing study aims to prove the scalability of ageing and consequently of the state estimation. At cell level, a state of charge dependent change in open circuit voltage is observed, which is independent from the ageing conditions and correlates with the capacity degradation. By comparing the open circuit voltage of the aged cells and modules fairly similar changes are observed, and as a result, the scalability of ageing can be confirmed.

This thesis concludes that the Kalman filter is not necessarily feasible in real applications. The strongly varying model parameters, as well as the temperature and ageing dependent open circuit voltage, require an empirical adaptation of the inconstant and non-linear filter tuning parameters. Hence, the performance of the Kalman filter in a real application is significantly lower compared to the laboratory environment with its high constrains.

List of publications

Conference contributions

Walder, G.; Campestrini, C.; Kohlmeier, S.; Lienkamp, M.; Jossen, A.: Functionality and Behaviour of an Dual Kalman Filter implemented on a Modular Battery-Management-System, In: Bayern Innovativ (Hrsg.): Conference on Future Automotive Technology: Focus Electromobility, 2013

Campestrini, C.; Walder, G.; Jossen, A.; Lienkamp, M.: Temperature Influences on State and Parameter Estimation Based on a Dual Kalman Filter, In: Bayern Innovativ (Hrsg.): Conference on Future Automotive Technology: Focus Electromobility, 2014

Walder, G.; Campestrini, C.; Lienkamp, M.; Jossen, A.: Adaptive State and Parameter Estimation of Lithium-Ion Batteries based on a Dual Linear Kalman Filter, In: Asia Pacific University of Technology and Innovation (APU) (Hrsg.): The Second International Conference on Technological Advances in Electrical, Electronics and Computer Engineering (TAEECE2014), 2014

Campestrini, C.; Karl, R.C.; Keil, P.; Schuster, S.; Jossen, A.: Vergleich der Alterung von Lithium-Ionen-Batterien auf Zell- und Modulebene, In: Design & Elektronik (Hrsg.): 22. Design & Elektronik - Entwicklerforum Batterien & Ladekonzepte, 2015

Campestrini, C.; Karl, R.C.; Keil, P.; Schuster, S.; Jossen, A.: Module ageing of Li-ion cells with active balancing compared to the ageing behaviour on cell level, In: World Electric Vehicle Association (Hrsg.): EVS28 - The 28th International Electric Vehicle Symposium, 2015

Campestrini, C.; Schuster, S.F.; Karl, R.C.; Ni, C.; Andreas, J.: Equivalent circuit based modelling and prediction of the ageing behaviour of lithium-ion cells, In: World Electric Vehicle Association (Hrsg.): EEVC - European Electric Vehicle Congress, 2015

Schuster, S.F.; Brand, M.J.; Campestrini, C.; Gleissenberger, M.: Correlation between capacity and impedance of lithium-ion cells during calendar and cycle life, In: World Electric Vehicle Association (Hrsg.): EEVC - European Electric Vehicle Congress, 2015

Campestrini, C.; Heil, T.; Kosch, S.; Jossen, A.: A comparative study and review of different Kalman filters by applying an enhanced validation method. In: Kompetenznetzwerk Lithium-Ionen-Batterien e. V. (Hrsg.): Batterieforum Deutschland, 2017

Peer-Reviewed journal contributions (lead author)[1]

Campestrini, C.; Keil, P.; Schuster, S.F.; Jossen, A.: Ageing of lithium-ion battery modules with dissipative balancing compared with single-cell ageing, In: Journal of Energy Storage 6, S. 142–152, 2016

Campestrini, C.; Horsche, M.F.; Zilberman, I.; Heil, T.; Zimmermann, T.; Jossen, A.: Validation and benchmark methods for battery management system functionalities – State of charge estimation algorithms, In: Journal of Energy Storage 7, S. 38–51, 2016

Campestrini, C.; Heil, T.; Kosch, S.; Jossen, A.: A comparative study and review of different Kalman filters by applying an enhanced validation method, In: Journal of Energy Storage 8, S. 142–159, 2016

Campestrini, C.; Kosch, S.; Jossen, A.: Influence of change in open circuit voltage on the state of charge estimation with an extended Kalman filter, In: Journal of Energy Storage 12, S. 149–156, 2017

Peer-Reviewed journal contributions (co-author)

Schuster, S.F.; Brand, M.J.; Campestrini, C.; Gleissenberger, M.; Jossen, A.: Correlation between capacity and impedance of lithium-ion cells during calendar and cycle life, In: Journal of Power Sources 305, S. 191–199, 2016

Journal contributions (lead author)

Campestrini, C.: Altern im Vergleich, In: Design & Elektronik 2015 (6), S. 40–44, 2015

[1] These peer-reviewed journal contributions are parts of this doctoral thesis without further referencing in the running text. This especially concerns Chapter 5 to Chapter 9.

Contents

Abbreviations **i**

Symbols **v**

I Literature and Fundamentals

1 Introduction **1**

1.1 Motivation 1

1.2 Literature research 3

1.2.1 Lithium-ion cell modelling 3

1.2.2 Kalman filter 4

1.2.3 Validation of state estimation algorithms 5

1.2.4 Comparative studies of different Kalman filters 7

1.2.5 Influence of change in open circuit voltage on the state of charge estimation 8

1.2.6 Ageing of lithium-ion cells and modules 8

1.3 Objectives and structure of this work 10

2 Fundamentals of lithium-ion cell modelling **13**

2.1 Equivalent circuit based cell modelling 13

2.2 Discretisation of the equivalent circuit model 16

3 Fundamentals of Kalman filtering **21**

3.1 General Kalman filter implementation 21

3.2 Variations of Kalman filter algorithms 23

3.2.1 Extended Kalman filter 23

3.2.2 Adaptive extended Kalman filter 23

3.2.3 Unscented Kalman filter 24

3.2.4 Central difference Kalman filter 25

3.2.5 Square root forms of the unscented and the central difference Kalman filter 25

3.2.6 Dual Kalman filter 25

3.3 Filter tuning 26

II Solution Approach

4 Experimental **27**
4.1 Introduction of examined cells . . . 27
4.2 Design of the battery modules . . . 27
4.2.1 Topology . . . 27
4.2.2 Construction . . . 29
4.2.3 Capacity-based cell matching . . . 29
4.3 Measurement setup at single cell and module level . . . 31
4.4 Methods used for determining equivalent circuit model parameters . . . 33
4.5 Methods used for cell diagnosis . . . 34
4.6 Ageing study at single cell and module level . . . 35
4.7 Overview of experiments . . . 37

5 Validation and benchmark method for state estimation algorithms **41**
5.1 Analysis of driving profiles . . . 41
5.2 Generation of an application-independent test profile . . . 42
5.3 Validation scenarios . . . 44
5.4 Benchmark of state of charge estimation algorithms . . . 47
5.4.1 Estimation accuracy K_{est} . . . 47
5.4.2 Drift behaviour K_{drift} . . . 48
5.4.3 Residual charge determination K_{res} . . . 49
5.4.4 Transient behaviour K_{trans} . . . 50
5.4.5 Failure stability K_{fail} . . . 51
5.4.6 Temperature stability K_{temp} . . . 51
5.4.7 Overview . . . 52
5.5 Conclusion . . . 52

III Results and Discussion

6 Experimental investigation of lithium-ion cell behaviour **55**
6.1 Dependencies of equivalent circuit elements of a new cell . . . 55
6.2 Dependencies of equivalent circuit elements of an aged cell . . . 57
6.3 Dependencies of the open circuit voltage at different ageing states . . . 59
6.4 Conclusion . . . 62

7 Influence of cell behaviour on the state estimation with different Kalman filters **63**
7.1 Initialisation of the Kalman filter . . . 63
7.2 State estimation: single Kalman filter . . . 64
7.3 State estimation: dual Kalman filter . . . 71
7.4 Parameter estimation: dual Kalman filter . . . 74

7.5 Benchmark: summary and comparison . . . 75
7.6 Individual filter tuning and correct equivalent circuit model parameters . . . 76
7.7 Conclusion . . . 77

8 Influence of change in open circuit voltage on the state of charge estimation 79
8.1 State of charge determination by the open circuit voltage . . . 79
8.2 State of charge estimation by the Kalman filter . . . 80
8.3 Conclusion . . . 83

9 Ageing behaviour of open circuit voltage at single cell and module level 85
9.1 Ageing at single cell level . . . 85
9.1.1 Capacity and resistance development . . . 85
9.1.2 Changes of the open circuit voltage . . . 87
9.2 Ageing at module level . . . 90
9.2.1 Capacity and resistance development of modules . . . 90
9.2.2 Capacity and resistance of single blocks . . . 91
9.2.3 State of inhomogeneity during the progress of ageing . . . 94
9.2.4 Correlation of ageing and temperature . . . 95
9.2.5 Energy efficiency . . . 96
9.2.6 Cell balancing . . . 97
9.2.7 Changes of the open circuit voltage . . . 98
9.3 Conclusion . . . 100

IV Final Conclusion

10 Summary and further work 103
10.1 Summary . . . 103
10.2 Recommendation and outlook . . . 107

References 109

List of Figures 125

List of Tables 131

Appendix 133
A Data-sheet of the Panasonic NCR18650PD NCA cell . . . 133
B Measurement equipment . . . 134
C Vehicle model parameters . . . 135
D Kalman filter initialisation . . . 136

Abbreviations

AEKF . . . . . adaptive extended Kalman filter

AKF . . . . . adaptive Kalman filter

BEV . . . . . battery electric vehicle

BMS . . . . . battery management system

BSD . . . . . battery safety device

CAN . . . . . controller area network

CC . . . . . constant-current

CCCV . . . . . constant-current constant-voltage

CDKF . . . . . central difference Kalman filter

CG . . . . . cell group

CMU . . . . . cell measurement unit

CTS . . . . . cell test system

CV . . . . . constant-voltage

DAEKF . . . . . dual adaptive extended Kalman filter

DC . . . . . direct current

DEKF . . . . . dual extended Kalman filter

DFT . . . . . discrete Fourier transformation

DKF . . . . . dual Kalman filter

DOD . . . . . depth of discharge

DVA . . . . . differential voltage analysis

ECM . . . . . equivalent circuit model

EFC . . . . . equivalent full cycles

EIS . . . . . electrochemical impedance spectroscopy

EKF . . . . . extended Kalman filter

EOL . . . . . end of life

EV . . . . . electric vehicle

FFT . . . . . fast Fourier transformation

HPS . . . . . high power system

IC . . . . . incremental

KF . . . . . Kalman filter

LCO . . . . . lithium-cobalt-oxide

LFP . . . . . lithium-iron-phosphate

LIB . . . . . lithium-ion battery

LIC . . . . . lithium-ion cell

LKF . . . . . linear Kalman filter

LUT . . . . . look-up table

M1 . . . . . module 1

M2 . . . . . module 2

NCA . . . . . nickel-cobalt-aluminium

NMC . . . . . nickel-manganese-cobalt

NN . . . . . neuronal network

OCV . . . . . open circuit voltage

PXI . . . . . PCI extensions for instrumentation

RMS . . . . . root mean square

SAEKF . . . . . single adaptive extended Kalman filter

SCDKF . . . . . single central difference Kalman filter

SEI . . . . . solid electrolyte interphase

SEKF . . . . . single extended Kalman filter

SESS . . . . . stationary energy storage system

SKF . . . . . single Kalman filter

SLC . . . . . synthetic load cycle

SLKF . . . . . single linear Kalman filter

SOC . . . . . state of charge

SOH . . . . . state of health

SOI . . . . . state of inhomogeneity

SPKF . . . . . sigma point Kalman filter

SSRCDKF . . . single square root central difference Kalman filter

SSRUKF . . . . single square root unscented Kalman filter

SUKF . . . . . single unscented Kalman filter

UKF . . . . . unscented Kalman filter

XCTS . . . . . extended cell test system

Symbols

α . . . . . state of inhomogeneity of selected single cells [%]

a . . . . . power distribution

A . . . . . dynamic load profile

$\mathbf{A}$ . . . . . system matrix

β . . . . . computed mean state of inhomogeneity [%]

$\mathbf{B}$ . . . . . transition matrix

γ . . . . . state of inhomogeneity based on ideal cell matching [%]

C_{act} . . . . . actual capacity [A h]

C_{block} . . . . . capacity of one block of the battery module [A h]

C_{cell} . . . . . capacity of one cell of one block in the battery module [A h]

C_n . . . . . capacitance of the n RC term [F]

C_{nom} . . . . . nominal capacity [A h]

C_{norm} . . . . . normalised capacity [%]

C_{res} . . . . . residual capacity [A h]

$\mathbf{D}$ . . . . . straight-way matrix

ε . . . . . error [%]

$\mathbb{E}$ . . . . . statistical expectation operator

$\bar{E}_{50\,\mathrm{EFC}}$ . . . . . mean energy throughput within 50 equivalent full cycles [W h]

$\bar{E}_{\mathrm{bal}}$ . . . . . mean balancing energy [W h]

ϕ . . . . . windows size

$\mathbf{\Phi}$ . . . . . fundamental matrix

f_{max} . . . . . maximum sample rate [Hz]

f_{s} . . . . . sample rate [Hz]

G . . . . . gradient

η . . . . . energy efficiency [%]

h . . . . . sigma point of the central difference Kalman filter

$\mathbf{H}$ . . . . . measurement matrix

I . . . . . terminal current [A]

$\mathbf{I}$ . . . . . identity matrix

κ . . . . . relative coefficients of variation

k . . . . . discrete time step

K_{drift} . . . . . drift score

K_{est} . . . . . estimation accuracy score

K_{fail} . . . . . failure stability score

K_{res} . . . . . residual charge score

K_{temp} . . . . . temperature stability score

K_{trans} . . . . . transient behaviour score

$\mathbf{K}$ . . . . . Kalman gain

λ_n . . . . . sigma point n of the unscented Kalman filter

$\mathcal{L}$ . . . . . Laplace transformation

μ . . . . . arithmetic mean value

n . . . . . indexing variable

N . . . . . number of periods

P . . . . . evaluation score

$\mathbf{P}$ . . . . . covariance matrix

Q_{bal} . . . . . balancing charge [A h]

$\bar{Q}_{50\,\text{EFC}}$ . . . . . mean charge throughput within 50 equivalent full cycles [A h]

$\bar{Q}_{\text{bal}}$ . . . . . mean balancing charge [A h]

$\mathbf{Q}$ . . . . . process noise matrix

ρ_{I} . . . . . current offset [%]

ρ_{R} . . . . . resistance offset [%]

ρ_{U} . . . . . voltage offset [%]

r . . . . . measurement noise

R_{block} . . . . . resistance of one block of the battery module [mΩ]

R_{cell} . . . . . resistance of one cell of one block in the battery module [mΩ]

R_{contact} . . . . . contact resistance [Ω]

$R_{\mathrm{dc1\,s}}$ . . . . . resistance measured one second after a current pulse [mΩ]

R_{i} . . . . . ohmic resistance [mΩ]

R_n . . . . . resistance of the n RC term [mΩ]

R_{norm} . . . . . normalised resistance

σ . . . . . standard deviation

s_0 . . . . . initial altitude [m]

$\mathbf{s}$ . . . . . Laplace operator

S . . . . . quantised signal

SOC_0 . . . . . initial state of charge [%]

SOC_{est} . . . . . estimated state of charge [%]

SOC_{ref} . . . . . reference state of charge [%]

SOC_{res} . . . . . state of charge based on the residual charge [%]

SOI_X . . . . . general state of inhomogeneity definition [%]

θ . . . . . parameter vector

τ_{dc} . . . . . time constant [s]

τ_n . . . . . time constant of the n RC term [s]

τ_{s} . . . . . sample time [s]

τ_{sh} . . . . . sample and hold time [s]

t . . . . . time of operation [h]

t_δ . . . . . time within a certain error boundary [h]

t_{E} . . . . . time of temperature cycling end [h]

t_{S} . . . . . time of temperature cycling start [h]

T . . . . . Temperature [°C]

u . . . . . input vector

U . . . . . terminal voltage [V]

U_0 . . . . . open circuit voltage [V]

$\bar{U}_{\text{block}}$ . . . . . mean block voltage [V]

$U_{\max}$ . . . . . maximum allowed cell voltage [V]

$U_{\min}$ . . . . . minimum allowed cell voltage [V]

U_n . . . . . overpotential of the nRC term [V]

v . . . . . Gaussian distributed white noise

v_0 . . . . . initial velocity [$\mathrm{m\,s^{-1}}$]

V^{ϕ} . . . . . average deviation of the measurement [V]

w . . . . . Gaussian distributed white noise

x . . . . . state vector

y . . . . . output vector

z . . . . . regression line

Part I

Literature and Fundamentals

1 Introduction

Initially in this chapter, a motivation is given to define the main topic of this thesis. Afterwards, a literature review concerning Kalman filtering is given. Based on this, four objectives are identified to assess the feasibility of Kalman filters (KF) in real applications. Furthermore, an overview of this work is presented.

1.1 Motivation

For lithium-ion cells (LICs) several state of charge (SOC) estimation algorithms are presented in literature [1]. One of the most common algorithms is the KF, which was invented by Rudolph Kalman [2] in 1960 and originally used to estimate trajectories for manned and unmanned spacecrafts. In 2004, Plett [3–5] introduced a method to use the KF for estimating the SOC of LICs, that is not directly measurable. This method was commonly adapted in later works, resulting in various implementations of state estimation based on KFs. The advantage of KFs is the consideration of model and measurement uncertainties, which results in a robust estimation behaviour.

Before the application of the KF in the field of batteries is shown, an example of an original application field is presented. This example highlights the differences compared to the use with batteries and the subsequent concerns are discussed.

To illustrate the functionality of a KF, it is applied to track a falling object by a radar [6]. This object has an altitude of s_0=100 km and a velocity of v_0=2000 m s^{-1}. Furthermore, the object is only affected by gravity (g=9.81 m s^{-2}), fraction or other braking influences are neglected. The standard deviation of the measurement accuracy of the radar is 300 m. The physical definition of the problem is represented by Eq. 1.1 with velocity $\dot{s}$ (Eq. 1.2) and acceleration $\ddot{s}$ (Eq. 1.3) as states.

$$s = s_0 - v_0 t - \frac{g t^2}{2} \tag{1.1}$$

$$\dot{s} = -v_0 - g t \tag{1.2}$$

$$\ddot{s} = -g \tag{1.3}$$

In this example the initial values for the states altitude and velocity are set to zero. The acceleration is the constant model input. The task for the KF is to estimate these states by minimising the error between the model and the real world by adapting the states.

Fig. 1.1a and Fig. 1.1b show the estimation results for altitude and velocity, respectively, and Fig. 1.1c as well as Fig. 1.1d show the corresponding error.

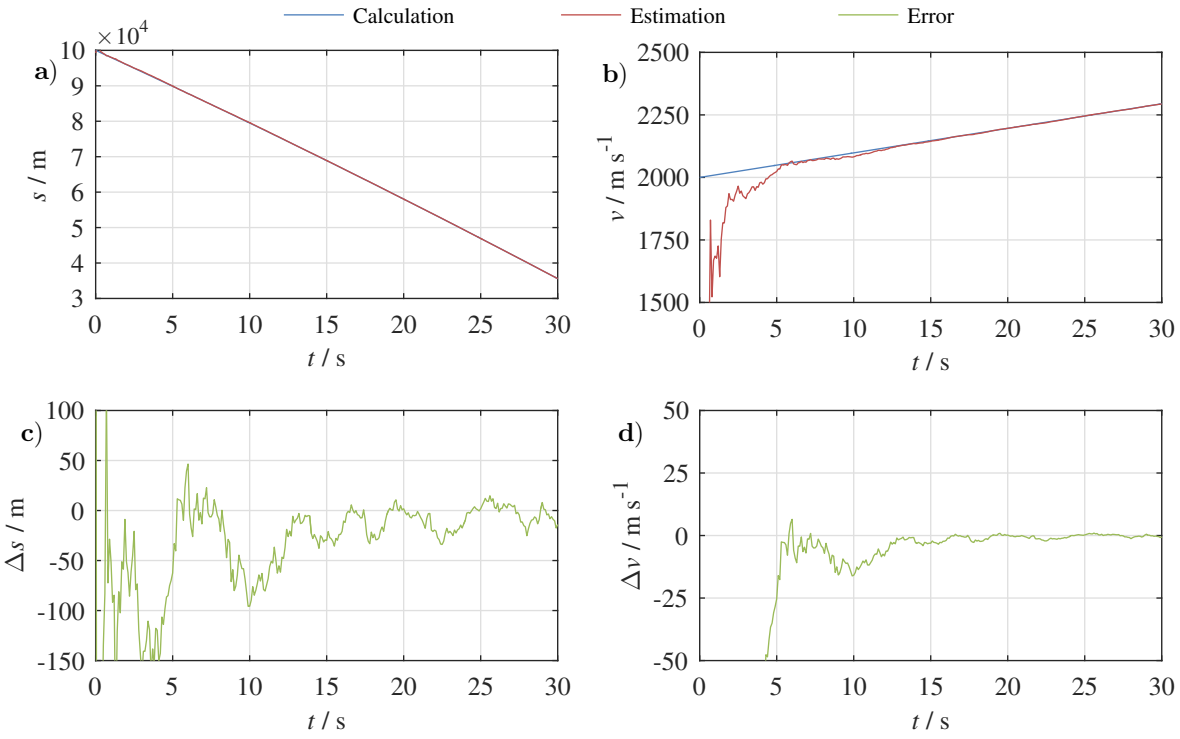

Figure 1.1: Tracking of a falling object: (a) altitude s; (b) velocity v; (c) altitude estimation error; (d) velocity estimation error.

As one can see, the errors of the altitude and velocity estimated by the KF converge to zero after 15 s. This is possible because the linear model implemented in the KF is identical to the linear problem. Moreover, the model parameters are constant, which reduces model uncertainties.

In the field of batteries, the models differ due to the complex, non-linear cell behaviour. These differences are caused by an insufficiently accurate model, or by inexact model parameters. By using a KF without model parameter estimation, in this work referred to as a single Kalman filter (SKF), uncertainties are increased due to constant model parameters. However, as a cell is dependent on SOC, temperature, current and age [7], the model uncertainties vary during operation, because a model is not able to represent all possible conditions. These model uncertainties must be compensated by adding process noise, but in literature these empirically determined values are mostly assumed to be constant. This allows a reliable and accurate estimation only in strictly defined ambient conditions, such as constant temperatures or short running times in order to neglect ageing effects.
To increase the model accuracy, and therefore decreased model uncertainties, a KF with an additional parameter estimation, in this work referred to as a dual Kalman filter (DKF), is used. Compared to the SKF, the parameters are estimated based solely on empirically determined, constant process noise without any model description. However, parameter estimation

is possible in constrained ambient conditions.

Taking this into account, a more detailed investigation of the KF behaviour is required to guarantee a reliable and accurate SOC and parameter estimation in a real application over lifetime, for example in an electric vehicle (EV). Here, the temperature demand can be between $-30\,°C$ and $50\,°C$ [8, p. 31].

To identify required factors for a feasibility study at cell and module level, the next section presents literature research into aspects regarding Kalman filtering.

1.2 Literature research

1.2.1 Lithium-ion cell modelling

The KF uses a cell model to estimate the state of a LIC. Therefore, an introduction to common modelling approaches is given in this section.
In the field of cell modelling, the charge and discharge behaviour of cells is mainly described by three different modelling approaches. The most accurate, but, consequently, most complex method is the electrochemical model. Here, mass and charge transfer reactions in the cell are described on a fundamental level with numerous partial differential equations. With this approach an accurate prediction of the terminal voltage can be achieved. However, the high complexity of the model comes with the price of high parametrisation and computational effort. In [9–12] a KF-based SOC estimation with an electrochemical model is introduced. Here, the state vector of the filter includes more than five state variables.

An additional modelling method is the black box model. Here, no physical knowledge of internal cell processes is required. Examples of black box models are: stochastic models [13], fuzzy logic models [14] or neuronal network (NN) models [15; 16]. To the authors knowledge, for the application with a KF, in literature only NN models are relevant [17; 18].

The most common approach is based on equivalent circuit models (ECMs). Here, the electrochemical behaviour of the cell is approximated by passive electrical elements such as resistors and capacities. Common implementations of this approach, like the Shepherd, Unnewehr and Nernst models, approximate the cell behaviour with a SOC dependent voltage source and additional resistors [4]. In [4; 19–26] these three models are combined and used in a KF. Wang et al. achieved higher estimation accuracy with a combined approach, using the Shepard, Unnewehr and Nernst models in combination and by selecting the particular model required depending on the voltage level [23].

By extending the ECM with additional capacitor and resistor networks (RC terms), model accuracy can be significantly enhanced. However, an increasing amount of RC terms results in higher model complexity and parametrisation effort. In [3; 4; 17; 27–49] different KFs are implemented with one RC term. To achieve higher accuracy in the voltage calculation, [50–64]

implemented different KFs with two RC terms.

Further improvements in model accuracy can be achieved by implementing a charge and discharge dependency of the ECM elements [4; 21; 29; 38] and/or hysteresis effects of the open circuit voltage (OCV) [4; 20; 33; 65].

Hu et al. compared the above mentioned models and their influence on the filter accuracy and came to the conclusion that the ECM with one RC term provides the best compromise between accuracy and complexity [66].

1.2.2 Kalman filter

The KF is based on a set of differential equations (model) to predict the state of a physical, real process. Therefore, it minimises the error between the measured and predicted output of a linear system by adapting the state variables. A common use of the filter in the battery field is to predict the cell voltage based on an ECM and a Coulomb counter. For this purpose, the relation between the SOC and the OCV is considered. The calculated voltage is then compared to the measured cell voltage and the difference is minimised by adapting the SOC and other ECM values. For linear systems a linear Kalman filter (LKF) can be used for state estimation [48; 54].

Due to the non-linear cell behaviour, the LKF is rarely used in literature. By linearising the system and measurement matrices in the actual state by first-order Taylor approximation of the differential equations, the KF can be applied to batteries. This approach is called extended Kalman filter (EKF) [5; 6; 21; 29–31; 35; 51; 53; 55; 67]. However, filter estimation can result in inaccurate behaviour and divergence of the filter, due to the linearisation error and the neglect of the higher-order derivatives of the Taylor approximation [67].

For this reason, the sigma point Kalman filter (SPKF) has been developed. Here, no derivatives are required, the linearisation is approximated by a set of sigma points [28; 67; 68]. Two common types of the SPKF are the unscented Kalman filter (UKF) and the central difference Kalman filter (CDKF).
In [21; 44; 54; 69–72] an UKF based on the unscented transformation is presented. This transformation is a method to approximate the expected value and the covariance of a random variable propagated through a non-linear function by omitting the derivation of system and measurement matrices [67].
The CDKF is based on the interpolation according to Stirling [27; 67; 73]. As in the case of the UKF, the derivation is omitted. The difference between both filters is connected to the implementation of scaling and gain factors. While the CDKF uses only one scaling factor, the UKF uses three.
The disadvantage of both filters is the required square root calculation of the covariance matrix with the Cholesky factorisation in each time step. However, rounding errors can occur and the positive definition of the covariance matrix can not be guaranteed [74]. To reduce

the calculation error, [67; 70] introduced the square root forms of the UKF and CDKF. Here, the Cholesky factorisation is only updated and not calculated in each time step.

The SOC estimation with a KF is highly dependent on the accuracy of the ECM parameters. If these values are not exact or fluctuate over time, the estimation error of the filter increases. A joint or dual estimation can compensate this by adapting the ECM parameters. In the case of the joint estimation, the states and parameters are in the same state-space [75; 76]. Due to the higher order of the resulting system, the computational effort increases with the third order (n^3) of the state vector dimension n [28]. To keep the system's order low, a separate state-space model can be used. Here, both filters work in parallel [3–5; 30; 67; 73; 77], but, consequently, the correlation between the states and parameters may get lost, which may result in higher estimation errors [28].

Due to the serial connection of LIC in battery modules, state estimation of each serial block is required. This can lead to high computational efforts and memory requirements. In order to not have to calculate the state of every single block, in literature two methods with an EKF are proposed. Dai et al. describe a two step method, whereby in the first step the average SOC of the module is estimated, then the differences between the block SOC from the average SOC is derived [52]. The other method is to estimate the lowest SOC in a module by considering the minimal block voltage [78]. In this case, the SOC can't be used for other battery management system (BMS) functions such as balancing.

To guarantee an accurate and stable behaviour of the filters, precise filter tuning is required. Therefore, the correct values of the process (model uncertainties) and measurement noise and the covariance matrices (estimation uncertainty) must be found. Due to the lack of exact noise information, these values are determined empirically. This process is called filter tuning.
To reduce the time-consuming filter tuning procedure, adaptive Kalman filters (AKFs) are introduced [19; 32; 37; 41; 43; 49; 56]. Here, the process and measurement noise is calculated on-line based on the error between measured and predicted output voltage. Although here an initial guess also has to be made.
Saha et al. presented a different approach where the process and measurement noise can be found off-line and is not adapted during progress [79]. Compared with the adapting approaches, the measurement noise can also be set stepwise depending on the SOC [29].

1.2.3 Validation of state estimation algorithms

Within the literature, various algorithms for SOC estimation are validated by different methods without further benchmarking. However, a comparison of the results is not possible, as the area of application is multilateral and the shortcomings of the estimators are often not considered in the validation process.

An important issue in the validation is the determination of a reference SOC to compare the estimated SOC with a reliable value. A common method of measuring the reference SOC is

the Coulomb counter (Eq. 1.4):

$$SOC(t) = SOC_0 + \frac{1}{C_{\text{act}}} \int_{t=0}^{t} i(\tau) d\tau \tag{1.4}$$

where SOC_0 corresponds to the initial SOC, C_{act} to the actual measured capacity of the cell, $i(\tau)$ to the load current and t to the time of operation. Therefore, a positive load current corresponds to charging. One issue is that, mostly, the same current signal is used to calculate the reference SOC and to estimate the SOC with the algorithm [17; 22; 45; 80; 81].
An offset-afflicted measurement causes a drift in the reference, calculated by Eq. 1.4. When the algorithm is not able to correct this drift, the estimation follows the offset-influenced reference. Other algorithms, for example OCV-based algorithms, may correct the error, but, when using only one current sensor, it is not possible to distinguish between the correct and incorrect SOC (Fig. 1.2a).
This shortcoming can be addressed by using two different sensors for the reference and for the algorithm [36; 39; 52; 71]. Therefore, the current sensor for the reference must be more accurate than the sensor for the algorithm. In Fig. 1.2b, this concept is depicted schematically. The estimation based on the current measurement of a BMS (Fig. 1.2b, sensor 1) drifts apart, while the algorithm partly compensates for the error.

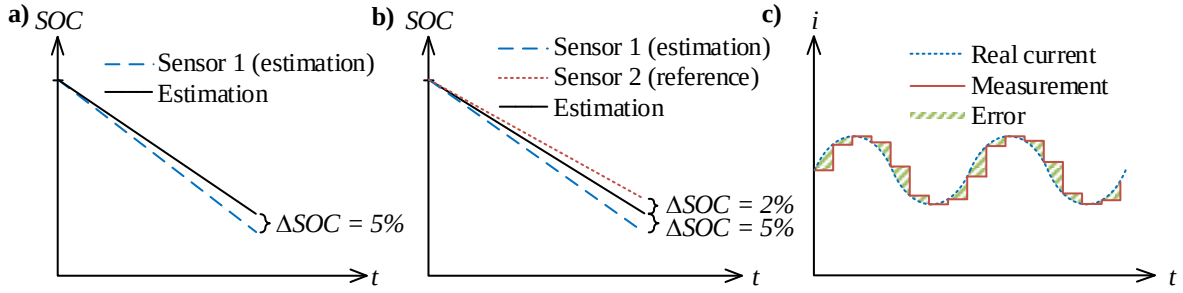

Figure 1.2: Validation issues: (a) validation with one current sensor (constant-current (CC) discharge); (b) validation with an additional, more accurate, current sensor (CC discharge); (c) shortcomings of discretising and resulting error.

By determination of the reference SOC using a Coulomb counter, the finite sample rate causes an error during dynamic loads. In Fig. 1.2c the real current (dashed line) and the discrete current measurement (solid line) is shown. The green area symbolises the resulting error, caused by the discrete measurement. Furthermore, temperature changes and high currents can cause temporary capacity (C_{act}) variations, which can affect the SOC calculation (Eq. 1.4). A potentially more accurate way to define a reference SOC is a residual charge determination at the end of each test. Due to the CC discharge, the accumulated error, caused by the finite sample rate and other influences, can be minimised. This approach is mandatory for long-term tests. [39]

The behaviour of a battery depends on temperature, SOC and current rate. Furthermore, the OCV changes with temperature, depending on chemistry and SOC [82; 83]. Consequently,

due to possible temperature variations during operation, the validation has to be performed at different and varying temperatures, otherwise a reliable and accurate function cannot be guaranteed. [39]

The algorithms presented in the literature are rarely validated during the charging process. In common applications, the discharge current is highly dynamic, while in the charge direction, the current is comparatively constant. As an example for neural networks, this also leads to the need for separate training data for the charge period. Other algorithms such as the dual KF [3–5] or the sliding mode observer [84] also behave differently without any dynamics [39; 42]. These behaviours are often neglected.

Due to the wide measurement range of current sensors, the measurement accuracy of small currents can be disturbed by noise or by an offset of the sensor. These errors can affect the SOC estimation. In order to address these issues, pauses and long-term tests [62] are necessary. During these tests, the SOC based on the Coulomb counter increases due to the current sensor offset, while the SOC estimation of the algorithm follows the reference SOC [39].

Further investigations showed the estimation accuracy and stability concerning variable ambient temperatures as well as ageing effects. Additionally, the influences of initialisation and parameter errors are mandatory for a proper validation [45].

1.2.4 Comparative studies of different Kalman filters

Despite the importance of the filter tuning parameters, most publications about KFs as well as comparative studies of different filters rarely provide information about the filter tuning. So, the comparability is to be considered as critical, due to the high influence of the filter tuning on the estimation behaviour and accuracy.

In [27; 45; 55] an EKF is compared with a SPKF. Here, the results in [45; 55] indicate a similarly accurate estimation of both filters, while in [27] the EKF displayed inaccurate behaviour. However, information about the filter tuning is not presented in these publications. In [20; 26; 35] an EKF is compared with an UKF. In [20] fairly similar results of the EKF and UKF are presented by using the same filter tuning. However, in [26; 35] the UKF demonstrated a better performance. The filter tuning is the same for both algorithms.
Sun et al. compared an EKF with an adaptive extended Kalman filter (AEKF) [20]. In contrast to [19], both filters showed the same results. As shown in [20; 26; 35; 45; 55], the EKF can result in accurate estimation and stable behaviour. Nevertheless, in [40; 57] an EKF with an adaptive ECM approach is compared with an EKF without any ECM adaptation, whereby the latter shows inaccurate results. The tuning parameters are not mentioned.

As one can see, comparable types of KFs can result in completely different results. This shows the importance of the filter tuning and a comparative validation method.

1.2.5 Influence of change in open circuit voltage on the state of charge estimation

As already mentioned in Section 1.2.2, the KF considers the relation between the SOC and the OCV to estimate the states. Whereby, the OCV can be represented by a model or look-up table (LUT) in the filter. This may lead to large deviations compared to the measured OCV resulting in high estimation errors or unstable estimation behaviour. Nevertheless, the influence of the OCV on the SOC estimation is rarely investigated in literature.

In [71] the influence of the temperature-dependent OCV of a lithium-iron-phosphate (LFP) cell on the SOC estimation with a KF is investigated. Here, high errors resulting from an incorrect OCV–SOC correlation are shown. To resolve this problem, different OCVs at different temperatures are implemented in the battery model.

Zheng et al. showed, that this temperature dependency is also influenced by the OCV determination method [85]. Here, the OCV, determined by a constant charge/discharge with a current of C/20 (constant-current (CC)-OCV), and the OCV, determined by 10 % charge/discharge steps followed by a 2 h relaxation time (incremental (IC)-OCV), are compared and the influence on the SOC estimation with a KF is investigated. In their work, the OCV shows a high deviation from the reference at lower temperatures, and therefore, the estimation of the KF is more accurate when the IC-OCV is used. However, at 0 °C both the CC-OCV and the IC-OCV method lead to high estimation errors, whereas the regions lower than 10 % and higher than 90 % are not considered.

The influence of an aged OCV on the SOC estimation with KFs is often not considered in literature.

1.2.6 Ageing of lithium-ion cells and modules

Until today, LICs are mainly used in mobile devices such as cell phones and laptops [86]. However, with the necessity of high-energy and high-power battery packs for different applications, such as stationary energy storage systems (SESSs) or EVs, cells must be connected in series and parallel. As a consequence of the increasing amount of cells connected in series, the computational effort for state estimators increases, as the state for each cell is required. Therefore, in [38; 52; 87; 88] the KF is applied on module and pack level by scaling the ECM parameters. Similar to the state estimation on cell level, the ageing influence is not considered. To take this into account, the ageing behaviour on module and pack level as well as the ageing scalability has to be investigated. Consequently, a profound understanding of the ageing behaviour of LICs, modules and packs is mandatory.

Numerous studies on the ageing behaviour of lithium-ion batterys (LIBs) at the cell level have been presented in past and recent publications [89–101], in contrast to investigations at the battery pack or at the module level. The consequences of ageing generally result in a loss of

capacity and an increase in impedance, with the latter resulting in a loss of power capability [102].

The main reasons for ageing can generally be subdivided into three main categories, which include: the loss of active lithium, the degradation of electrode materials, and deteriorated ionic kinetics [89]. Among the numerous ageing mechanisms of LICs, the formation and evolution of the solid electrolyte interphase (SEI) layer at the interface of the anode and the electrolyte take on a key role. This layer ideally inhibits any decomposition of the electrolyte after formation [103–105] and grows in thickness over their lifetime, especially at a high SOC and high temperatures [106–108]. The increase of this layer results in a decreasing capacity because of the consumption of active lithium accompanied by an increase in impedance. Therefore, long operation periods at high SOC and temperatures should generally be avoided for LICs [107; 109–112]. For a more comprehensive description of the various ageing mechanisms of LICs, such as lithium plating or the effects of volumetric changes of active materials, the reader is referred to [106; 109; 113–115].

In addition to the loss of capacity and increase in impedance the OCV also changes over lifetime, which can influence the state estimation by a KF because of the OCV–SOC relation. A change in shape of the OCV due to degradation effects is observed in more recent publications [116–119]. However, the relation between SOC and OCV is often assumed to be constant over the lifetime of a LIC [33]. Similarly to the capacity degradation, these variations can be explained by a change in the electrode morphology due to the formation of dendritic deposits [120], loss of cycable lithium-ions [119], loss of active materials [119; 121; 122] or a changing electrode balancing [123]. As a consequence, the correlation between OCV and SOC changes during ageing [124] and the relation has to be updated for an accurate state estimation based on the OCV [125]. In [126] the SOC of an aged lithium-cobalt-oxide (LCO) and in [127] that of a nickel-manganese-cobalt (NMC) cell is derived from the OCV–SOC relation of a new cell. In both publications a maximum SOC error of approximately 10 % is observed.

Apart from the works describing the ageing behaviour or mechanisms of LICs, statistical investigations conclude that variations in the initial lithium-ion cell-to-cell parameters (e.g. capacity and impedance parts) will increase with the progression of ageing, even for cells cycled in the laboratory under controlled ambient conditions [128–132]. Cell-to-cell (or lot-to-lot) variations in the new state must be ascribed to the production process, wherein variations in the manufacturing process parameters may occur [133; 134].
In contrast to these intrinsic causes of cell parameter variations, predominantly extrinsic causes are assumed to be responsible for an increase in the parameter spread during the course of ageing in battery units (e.g. parallel blocks, modules and packs). Such extrinsic causes include temperature gradients in the battery pack or deviations in the conductor resistances, cell contact resistances and also their type of interconnection [135; 136]. Cells that are connected in series are loaded with the same current but can be operated within different voltage swings because the weakest cell always determines the performance of the entire string [137]. In contrast, differences in the cell resistances in parallel connected cells cause an

uneven current distribution, which in turn results in SOC drifts [138]. As the SOC influences the OCV, these drifts automatically equalise at pause periods. In summary, during ageing, lithium-ion cell-to-cell parameter variations increase in the field because of the aforementioned extrinsic reasons, whereby a link to initial cell-to-cell variations in the new state because of production tolerances should additionally be assumed [132].
For cells which are interconnected in battery units, it is questionable whether this increasing spread of cell characteristics accelerates the ageing behaviour at module level compared with that of single cells. For example, a 20 % mismatch in the ohmic resistance of two LFP-based cells connected in parallel led to a lifetime reduction by 40 % when compared with an optimally matched compound [138]. However, the ageing behaviour of these parallel compounds was not compared with that of single cells. In addition, most of the ageing experiments in the laboratory are only performed with single LICs because battery unit investigations result in a higher complexity as well as higher measurement equipment requirements and resources.

To show the feasibility of the KF, the different objectives of this work are derived from the presented literature research in the next section. Furthermore, the structure of this work is described.

1.3 Objectives and structure of this work

From the motivation and literature research above, four objectives are derived to fulfil the investigation of the practical feasibility of KFs in real applications on cell and module level:

Objective 1: LIC modelling and experimental investigation of the cell behaviour

The Implementation of a KF in the field of batteries requires an accurate cell model. This model and the quality of the corresponding parameters are the basis for a precise state estimation. The literature research about ECMs showed (Section 1.2.1), that the ECM consisting of the OCV, an ohmic resistance and one or two RC terms are commonly used with KFs due to the compromise between accuracy and complexity. To use this ECM in a real application with varying conditions, e.g. temperature, the investigation of the ECM parameter dependencies is necessary to guarantee an accurate functionality of the state estimation with KFs. Hence, the parameter dependencies of this ECM with one and two RC terms are presented and related to physicochemical effects (Chapter 2). Furthermore, the determined ECM parameters in this work are compared with the cell behaviour described in literature to confirm these results (Chapter 6). Therefore, cells in different ageing states are considered.

Objective 2: Influence of ECM parameters on different KFs

Section 1.2.2 summarised the different KF types implemented in literature. Among others,

SKF and DKF are mentioned and methods to determine the filter tuning parameters are presented. Chapter 3 presents the general implementation of the KF and shows differences to the other KF forms. To show the resulting variation of estimation performance, all introduced KFs are compared. Therefore, a generalised validation and benchmark method (Chapter 5) is developed based on the literature research into validation of state estimation algorithms (Section 1.2.3), ECM parameter dependencies (Chapter 2) and the already mentioned shortcomings of comparative studies (Section 1.2.4). The validation contains an analysis of standardised driving cycles and a generation of an application-independent test profile. The resulting profiles are performed in a wide temperature range during low-dynamic, high-dynamic and long-term validation scenarios. Furthermore, due to the observed dependencies of ECM parameters on SOC, temperature, current and age (Chapter 6), the influence of ECM models and parameters on the estimation accuracy of the different KFs is investigated (Chapter 7).

Objective 3: Influence of the OCV on the state estimation

The literature research regarding the influence of the OCV on the SOC estimation (Section 1.2.5) showed a non negligible dependency on temperature and ageing state of the cell. Therefore, Chapter 8 investigates the influence on the state estimation by considering three cells in different ageing states over a wide temperature range.

Objective 4: Changes in OCV during lifetime at cell and module level

Due to the importance of the OCV as the reference for the KF, the ageing behaviour of the OCV is investigated in more detail. An ageing study is performed at cell (Section 9.1) and module (Section 9.2) level to show the ageing impact on the OCV. Additionally, Section 9.2 aims to compare the ageing behaviour of modules regarding capacity, resistance and OCV changes with that of single cells and evaluates present challenges in a module ageing study. Therefore, temperature influences, influences of contact resistances and the resulting impact on cell balancing are examined. For this purpose, two modules, consisting of 112 LICs each, were constructed. With the ageing experiments at module level, the scalability of ageing, and consequently the scalability of state of charge estimation algorithms, are investigated.

The present thesis is structured as shown in Fig. 1.3. Firstly, in this part, the literature research of this chapter and the fundamentals regarding cell modelling (Chapter 2) and Kalman filtering (Chapter 3) are presented to understand the further work. Afterwards, the experimental part of Chapter 4 and the validation and benchmark method of Chapter 5 introduce the solution approaches (Part II). The results and discussion Part III contains four chapters (Chapter 6 to Chapter 9), whereby each chapter corresponds to one objective presented above. Finally, the work is summarised and a final conclusion about the feasibility of KFs in real applications at cell and module level is given in Part IV.

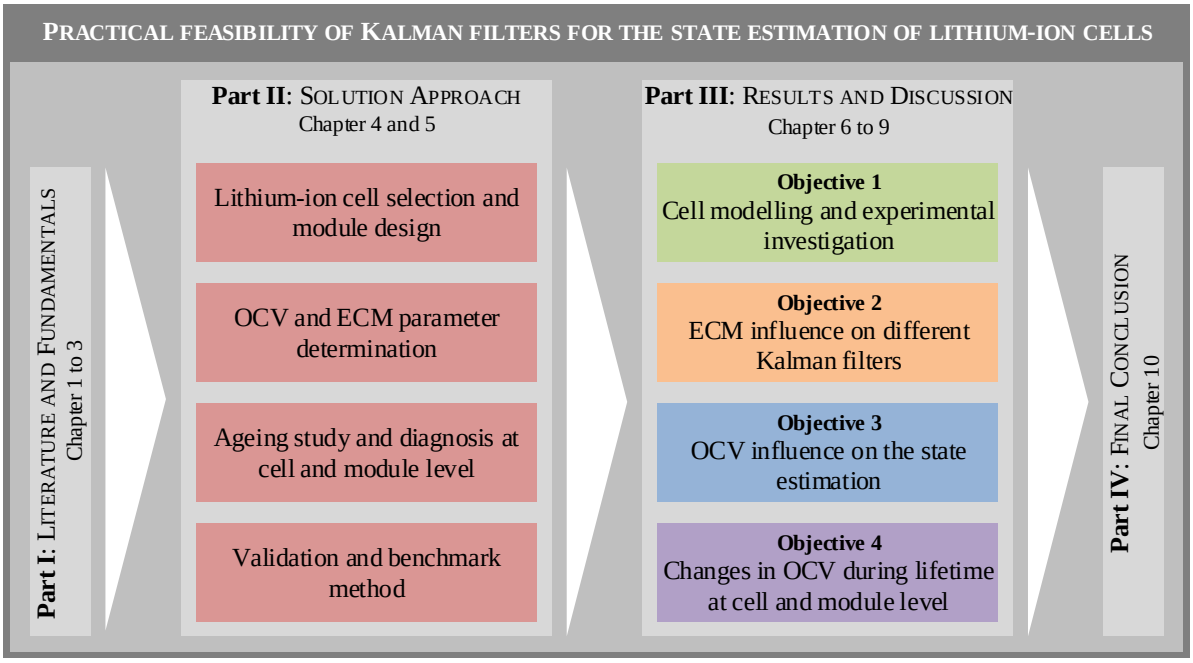

Figure 1.3: Structure of the work

It is noted, that the development of a new approach with a KF is beyond the scope of this work, although, design suggestions and recommendations for further works are presented.

2 Fundamentals of lithium-ion cell modelling

As Section 1.2.1 concluded that the ECM cell model with one and two RC term models are two of the most commonly used ECMs in state estimation by a KF, both models are used in this work.
In this chapter the structure of the one and two RC term ECM are presented and the dependencies of the ECM elements are discussed (Section 2.1). Furthermore, the discrete state-space notation of the ECM is derived in Section 2.2.

2.1 Equivalent circuit based cell modelling

In Fig. 2.1 the ECM with two RC terms is depicted. Furthermore, the dependencies of each element is shown. The ohmic resistance R_i contains the resistance of the current collectors, the electrolyte, SEI and additional contact resistances of the cell [139; 140]. The first RC term (R_1, C_1) represents the charge transfer processes that consist of the double-layer capacitance and the charge transfer resistance. The second RC term (R_2, C_2) describes diffusion effects that consist of the diffusion capacitance and the diffusion resistance [76]. The OCV U_0 is dependent on the SOC and calculated from an analytical equation or a LUT. [141]

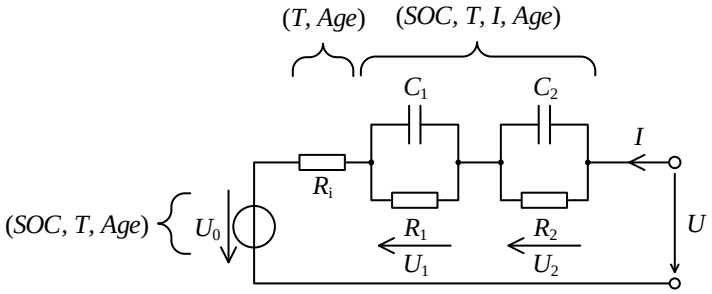

Figure 2.1: ECM consisting of one ohmic resistance (R_i), two RC terms (R_1, C_1 and R_2, C_2) and the SOC-dependent OCV U_0 with the corresponding dependencies. U and I correspond to the terminal voltage and current, respectively.

The ohmic resistance R_i is measured directly (approximately 1 ms) after a current change, or with an electrochemical impedance spectroscopy (EIS) at a frequency of approximately 1 kHz, where the imaginary part of the spectrum is zero [142], depending on the cell. This resistance does not participate in any reactions within the electrodes, resulting in a mostly independence from the SOC [143]. However, a temperature dependency related to the electrolyte can be observed. Therefore, a decreasing temperature leads to an increasing viscosity and poor

lithium-ion transport, resulting in an increased resistance [7; 140]. As already mentioned in Section 1.2.6, R_i increases with ageing as a result of the growing SEI as well as other ageing mechanisms.

Fig. 2.2 presents the normalised charge transfer resistances of different commercial 18650 cells (nickel-cobalt-aluminium (NCA), NMC and LFP) at 25 °C, whereby all cells show a similar behaviour (normalised to their maximum value) at low SOC level. The values for the RC terms are determined by current pulses [7; 65; 142] or EIS measurements [7; 142; 144]. In both cases, the voltage response of the applied current in time and frequency domain for pulses and EIS is fitted by least square methods to optimise the parameters of the ECM.

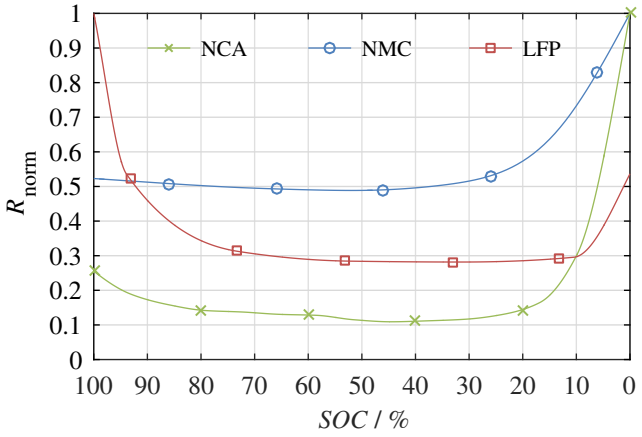

Figure 2.2: Normalised and interpolated charge transfer resistance R_1 of different commercial 18650 cells (nickel-cobalt-aluminium, nickel-manganese-cobalt and lithium-iron-phosphate) cell at 25 °C (normalised to their maximum value).

For the depicted cell chemistries, at low or high SOC levels, the charge transfer resistance increases or decreases with a strong non-linear behaviour, while in the midrange, a reasonably constant charge transfer resistance is observed. The behaviour in the midrange arises from a concentration equilibrium between reactants and products, resulting in an improved kinetic of the reversible processes [7; 143; 145].

A decreasing temperature results in a decreasing conductivity in the electrolyte and intercalation kinetics [7; 140; 145; 146]. As a consequence, the charge transfer resistance increases and the strong non-linear shape at low and high SOC is intensified [145]. In literature, these effects are mostly modelled by the Arrhenius law, which describes the temperature dependency of chemical processes [7; 140; 143; 146].

In [7] a current rate dependency on the charge transfer resistance R_1 is also shown. With increasing current the contributions of the charge transfer polarisation decreases, resulting in a decreasing R_1. In literature, the charge transfer is described by the Butler-Volmer equation [142; 147]. The current rate dependency increases at low temperatures and low SOC levels [7; 145]. Compared to R_1, C_1 shows little dependency on temperature or SOC. However, a change over lifetime is observed [7].

Due to slower chemical processes at lower temperatures, diffusion processes, described by the second RC term, are inhibited [142; 148], which causes the diffusion resistance R_2 to increase [146]. Similar to R_1, R_2 increases with decreasing SOC. Instead of the second RC term, the diffusion is often described by the Warbung impedance (frequency domain) [142].

The OCV is defined as the difference between the half-cell potentials of the cathode and the anode when the applied cell current is cut off and all polarisation effects are completely decayed. Here, the half-cell potential is related to the amount of lithium intercalated in each electrode. Consequently, the cell SOC changes with the SOC of both electrodes [83]. Fig. 2.3 shows the OCV of different commercial 18650 cells at 25 °C with common cathode materials such as NCA, NMC or LFP, all with graphite as the anode material. Therefore, the material composition of the active materials defines the characteristic potential curves of the OCV for the chemistry [119; 149].

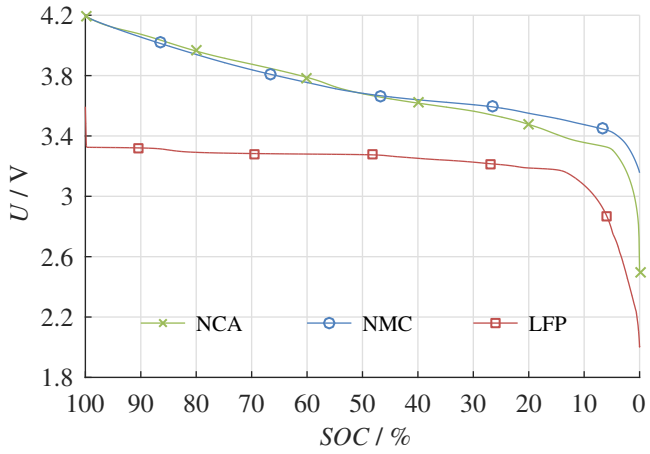

Figure 2.3: OCVs of commercial 18650 lithium-ion cells with graphite vs. different conventional cathode materials at 25 °C, measured by averaging the cell voltage of a constant current charge and discharge.

The high voltage drop at SOCs lower than approximately 10 % can be explained by the increasing potential of the delithiated anode [124]. In applications this region is often avoided due to practical reasons [121], for example, the fast voltage drop which results in a high current demand to fulfil the power requirement.

To determine the OCV, two common methods are established in practise [150]. The first method is the measurement of the cell voltage at a CC charge and discharge (CC-OCV). The OCV–SOC relation is then calculated by averaging the charge and discharge curve. Due to averaging, hysteresis effects and impedance influences are minimised [116]. The charge throughput is normalised to the actual cell capacity [83]. Hysteresis effects arise from mechanical stress and different thermodynamic states at the same SOC [83]. This effect is predominantly observed in LFP cells. In literature, the applied current to measure the OCV varies from C/20 [121] to C/40 [83; 119]. In general, a lower applied current leads to a lower cell polarisation [150; 151], thus, the OCV can be measured more accurately. However, as the

cell impedance can increase significantly at very low and very high SOCs, a low cell polarisation may not be ensured during measurement [119; 150; 151]. Therefore, the CC methods can lead to high voltage errors and imprecise OCV values in these high and low regions. This effect increases at lower temperatures [126] as well.
To minimise the voltage error, the OCV can be determined by the so-called incremental-OCV (IC-OCV). Here, the cell is charged and discharged stepwise to defined SOCs. After each step, the applied current is cut off and the OCV is measured when a defined relaxation time is reached. The relaxation time is dependent on SOC, temperature, cell chemistry and cell age [152]. In literature, the relaxation time varies from 1 h [118; 151; 153] to 24 h [126] and the step size from 4 % [126] to 10 % [85]. If the same SOC for each cut-off phase in charge and discharge direction can be guaranteed [151], the charge and discharge OCVs can be averaged to minimise hysteresis effects [153]. Excluding impedance effects, the temperature dependency of the OCV can be explained by SOC dependent entropy effects [154].

All elements of the presented ECM suffer from ageing. The main ageing effects are summarised in Section 1.2.6. Given that detailed investigations regarding ageing effects are not within the scope of this work, the reader is referred to the cited literature.

In Table 2.1 the dependencies of the ECM elements are summarised, including the corresponding publications.

Table 2.1: SOC, temperature T, current I and ageing dependencies of the ECM elements in literature.

	R_i	RC terms	U_0
SOC	[143]	[7; 140; 143; 145; 146; 155]	[83]
T	[7; 140; 146; 156]	[7; 122; 140; 143; 145; 146]	[71; 83; 85; 116; 156]
I	-	[7; 122; 142; 145–147; 157]	-
Age	[101; 108; 158]	[101; 158]	[116–119]

2.2 Discretisation of the equivalent circuit model

The use of the KF on discrete systems, for example a BMS, requires all equations in their discrete form. Therefore, in this section, the equations of the ECM presented above (Fig. 2.1) are derived and discretised for n RC terms. The resulting discrete state-space notation is then used in the KF implementation in the next section.

The equation for the terminal voltage U of the ECM with n RC terms, similar to Fig. 2.1, results to:

$$U = U_0(SOC) + U_1 + \cdots + U_n + R_\mathrm{i} I \tag{2.1}$$

To calculate the overpotential U_n, Kirchhoff's first law is applied to the RC term:

$$I(t) = i_{\mathrm{C}}(t) + i_{\mathrm{R}}(t) \tag{2.2}$$

From the equations of the RC term elements R_n and C_n the currents i_{C} and i_{R} result to:

$$i_{\mathrm{C}}(t) = C_n \dot{U}_n(t) \tag{2.3}$$

$$i_{\mathrm{R}}(t) = \frac{U_n(t)}{R_n} \tag{2.4}$$

Substituting the currents i_{C} and i_{R} in Eq. 2.2 with Eq. 2.3 and Eq. 2.4, respectively, the time-dependent voltage $\dot{U}_n(t)$ results to:

$$\dot{U}_n(t) = -\frac{1}{R_n C_n} U_n(t) + \frac{1}{C_n} I(t) \tag{2.5}$$

This derivation can be used for any RC-term.

The required SOC value for the SOC dependent OCV is obtained from the coulomb counter defined by Eq. 1.4. The corresponding deviation $\dot{SOC}(t)$ results to:

$$\dot{SOC}(t) = \frac{1}{C_{\mathrm{act}}} I(t) \tag{2.6}$$

Now, the derived equations can be used in the general state-space notation:

$$\dot{x}(t) = \mathbf{A}_t x(t) + \mathbf{B}_t u(t) \tag{2.7}$$

$$y(t) = \mathbf{H}_t x(t) + \mathbf{D}_t u(t) \tag{2.8}$$

Therefore, $x \in \mathbb{R}^n$ is the state of the considered system, $\mathbf{A} \in \mathbb{R}^{n \times n}$ the transition matrix, $\mathbf{B} \in \mathbb{R}^{n \times l}$ the influence of the input $u \in \mathbb{R}^l$ and $y \in \mathbb{R}^m$ the summation of the measured quantities. The measurement matrix $\mathbf{H} \in \mathbb{R}^{m \times n}$ connects the state x with the measurement and the straight-way matrix $\mathbf{D} \in \mathbb{R}^{m \times l}$ gives the influence of the input to the measurement. The system output y corresponds to the terminal voltage U and the system input u to the terminal current I. The index t symbolises continuous quantities.

With Eq. 2.5 and Eq. 2.6 the continuous state-space notation results to:

$$\begin{bmatrix} \dot{U}_1(t) \\ \vdots \\ \dot{U}_n(t) \\ \dot{SOC}(t) \end{bmatrix} = \begin{bmatrix} -\frac{1}{R_1 C_1} & 0 & \cdots & 0 \\ 0 & \ddots & \ddots & \vdots \\ \vdots & \ddots & -\frac{1}{R_n C_n} & 0 \\ 0 & \cdots & 0 & 0 \end{bmatrix} \begin{bmatrix} U_1(t) \\ \vdots \\ U_n(t) \\ SOC(t) \end{bmatrix} + \begin{bmatrix} \frac{1}{C_1} \\ \vdots \\ \frac{1}{C_n} \\ \frac{1}{C_{\mathrm{act}}} \end{bmatrix} I(t) \tag{2.9}$$

The equation for the model output in matrix form corresponds to the sum of the overpotentials

and the OCV of the presented ECM:

$$U(t) = \begin{bmatrix} 1 & \cdots & 1 & \frac{U_0(SOC(t))}{SOC(t)} \end{bmatrix} \begin{bmatrix} U_1(t) \\ \vdots \\ U_n(t) \\ SOC(t) \end{bmatrix} + R_\mathrm{i} I(t) \tag{2.10}$$

Eq. 2.9 and Eq. 2.10 are now discretised and transformed into the general discrete state-space notation:

$$x_{k+1} = \mathbf{A}_k x_k + \mathbf{B}_k u_k \tag{2.11}$$

$$y_k = \mathbf{H}_k x_k + \mathbf{D}_k u_k \tag{2.12}$$

The index k symbolises discrete quantities. According to [6], for every time invariant system matrix $\mathbf{A}_t$, the fundamental matrix $\mathbf{\Phi}$ exists. With this matrix the contiguous state can be propagated exactly from t_0 to any time t:

$$x(t) = \mathbf{\Phi}(t - t_0) x(t_0) \tag{2.13}$$

The fundamental matrix can be calculated using the Laplace transformation $\mathcal{L}$ with the Laplace operator $\mathbf{s}$ and the identity matrix $\mathbf{I}$ [6] according to:

$$\mathbf{\Phi}(t) = \mathcal{L}^{-1}[(\mathbf{sI} - \mathbf{A}_t)^{-1}] \tag{2.14}$$

$$\mathbf{\Phi}(t) = \begin{bmatrix} e^{-\frac{t}{R_1 C_1}} & 0 & \cdots & 0 \\ 0 & \ddots & \ddots & \vdots \\ \vdots & \ddots & e^{-\frac{t}{R_n C_n}} & 0 \\ 0 & \cdots & 0 & 1 \end{bmatrix} \tag{2.15}$$

Due to $\mathbf{\Phi}_k = \mathbf{\Phi}(\tau_\mathrm{s})$ [6], whereby τ_s is the sample time,

$$\mathbf{\Phi}(\tau_\mathrm{s}) = \mathbf{A}_k = \begin{bmatrix} e^{-\frac{\tau_\mathrm{s}}{R_1 C_1}} & 0 & \cdots & 0 \\ 0 & \ddots & \ddots & \vdots \\ \vdots & \ddots & e^{-\frac{\tau_\mathrm{s}}{R_n C_n}} & 0 \\ 0 & \cdots & 0 & 1 \end{bmatrix} \tag{2.16}$$

holds true. To discretise the transition matrix $\mathbf{B}_t$ (in this case a vector) the integral of the

continuous quantity $\mathbf{B}_t$ multiplied with $\mathbf{\Phi}$(t) is calculated and results to:

$$\mathbf{B}_k = \int_0^{\tau_\mathrm{s}} \mathbf{\Phi}(t)\mathbf{B}_t dt \tag{2.17}$$

$$\mathbf{B}_k = \begin{bmatrix} R_1\left(1 - e^{-\frac{\tau_\mathrm{s}}{R_1 C_1}}\right) \\ \vdots \\ R_n\left(1 - e^{-\frac{\tau_\mathrm{s}}{R_n C_n}}\right) \\ \frac{\tau_\mathrm{s}}{C_\mathrm{act}} \end{bmatrix} \tag{2.18}$$

With Eq. 2.16 and Eq. 2.18 the discretised state-space notation of the ECM with n RC terms results to:

$$x_{k+1} = \begin{bmatrix} e^{-\frac{\tau_\mathrm{s}}{R_1 C_1}} & 0 & \cdots & 0 \\ 0 & \ddots & \ddots & \vdots \\ \vdots & \ddots & e^{-\frac{\tau_\mathrm{s}}{R_n C_n}} & 0 \\ 0 & \cdots & 0 & 1 \end{bmatrix} x_k + \begin{bmatrix} R_1\left(1 - e^{-\frac{\tau_\mathrm{s}}{R_1 C_1}}\right) \\ \vdots \\ R_n\left(1 - e^{-\frac{\tau_\mathrm{s}}{R_n C_n}}\right) \\ \frac{\tau_\mathrm{s}}{C_\mathrm{act}} \end{bmatrix} u_k \tag{2.19}$$

$$y_k = \begin{bmatrix} 1 & \cdots & 1 & \frac{U_0(x_{n+1,k})}{x_{n+1,k}} \end{bmatrix} x_k + R_\mathrm{i} u_k \tag{2.20}$$

where τ_s and k are the sample time and the time step, respectively. The product of R_n and C_n corresponds to the time constant τ_n of the n RC term. The state vector contains n overpotentials of the RC terms and the SOC:

$$x_k = \begin{bmatrix} U_{1,k} & \cdots & U_{n,k} & SOC_k \end{bmatrix}^t \tag{2.21}$$

Now, the complete discrete state-space notation of the battery model is known and can be used with a KF. In the next chapter, the KF and variations of it are introduced.

3 Fundamentals of Kalman filtering

The literature research of Section 1.2.2 showed several variations of KFs. In this chapter the KF is introduced (Section 3.1) and the differences between the various KF implementations are identified (Section 3.2).

3.1 General Kalman filter implementation

To include model and measurement uncertainty to the discrete ECM (Section 2.2), noise is added to the state-space notation (Eq. 2.19 and Eq. 2.20). Two random variables $w_k \in \mathbb{R}^n$ and $v_k \in \mathbb{R}^m$ represent the process and the measurement noise, respectively. Considering this notation, the state-space representation and the measurement equation are extended to:

$$x_{k+1} = \mathbf{A}_k x_k + \mathbf{B}_k u_k + w_k \tag{3.1}$$

$$y_k = \mathbf{H}_k x_k + \mathbf{D}_k u_k + v_k \tag{3.2}$$

It is further assumed that the variables w_k and v_k consist of Gaussian distributed white noise. In addition, regarding the measured quantities, it is expected that the measuring devices are not offset afflicted. Furthermore, all measurements occur independently from each other. Moreover, it is assumed that the perturbation due to the process noise appears in the same manner. If the process noise and the measurement noise are uncorrelated and the mean values are zero, it can be assumed that:

$$\mathbb{E}\left[ww^t\right] = \mathbf{Q} \tag{3.3}$$

$$\mathbb{E}\left[vv^t\right] = r \tag{3.4}$$

Thereby, $\mathbb{E}$ is the statistical expectation operator, r the covariance of the measurement noise and $\mathbf{Q}$ the covariance of the process noise matrix. [3]

The KF belongs to the prediction-correction method. It first predicts a state $\hat{x}_k^-$ in its state-space notation and the corresponding covariance matrix $\mathbf{P}_k^-$. In the next step, the Kalman gain $\mathbf{K}$ is computed. Then, the KF corrects the prediction ($\hat{x}_k^+$ and $\mathbf{P}_k^+$) by weighting the difference between the real measurement U_k and the predicted measurement result y_k with the $\mathbf{K}_k$. The working principle of the KF is shown in Fig. 3.1.

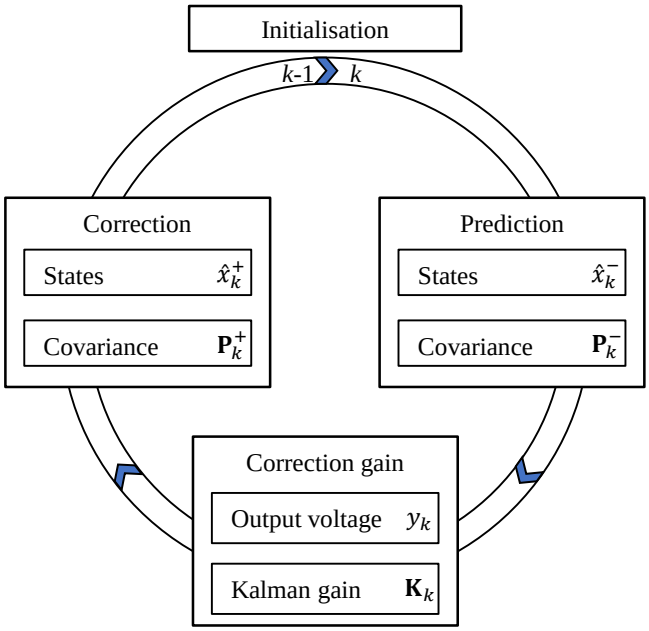

Figure 3.1: Calculation sequence of a Kalman filter

Due to the assumptions made in Eq. 3.4 and Eq. 3.3, the algorithm simplifies to the following calculation sequence [3; 159]:

Initialisation:

$$\hat{x}_0^+ = \mathbb{E}\left[x_0\right] \tag{3.5}$$

$$\mathbf{P}_0^+ = \mathbb{E}\left[\left(x_0 - \hat{x}_0^+\right)\left(x_0 - \hat{x}_0^+\right)^t\right] \tag{3.6}$$

Prediction:

$$\hat{x}_k^- = \mathbf{A}_{k-1}\hat{x}_{k-1}^+ + \mathbf{B}_{k-1}u_{k-1} \tag{3.7}$$

$$\mathbf{P}_k^- = \mathbf{A}_{k-1}\mathbf{P}_{k-1}^+\mathbf{A}_{k-1}^t + \mathbf{Q} \tag{3.8}$$

Correction gain:

$$y_k = \mathbf{H}_k\hat{x}_k^- + \mathbf{D}_k u_k \tag{3.9}$$

$$\mathbf{K}_k = \mathbf{P}_k^-\,\mathbf{H}_k^t\,\left(\mathbf{H}_k\,\mathbf{P}_k^-\,\mathbf{H}_k^t + r\right)^{-1} \tag{3.10}$$

Correction:

$$\hat{x}_k^+ = \hat{x}_k^- + \mathbf{K}_k\left(U_k - y_k\right) \tag{3.11}$$

$$\mathbf{P}_k^+ = \left(\mathbf{I} - \mathbf{K}_k\mathbf{H}_k\right)\mathbf{P}_k^- \tag{3.12}$$

In the subsequent work, this type of KF is referred to as a LKF. The described calculation sequence is used in all different types of KFs.

The differences between the algorithms are introduced in the next section.

3.2 Variations of Kalman filter algorithms

In this section the differences between various KFs are shown. All described algorithms are state of the art and well published. The reader is referred to cited literature for the complete algorithm implementations.

3.2.1 Extended Kalman filter

The model explained in Section 3.1 is not able to describe non-linear physical systems such as the charge transfer reaction of electrochemical cells. To include non-linear behaviour, it is assumed that the state-space equation and measurement equation have the form:

$$x_{k+1} = f\left(x_k, u_k\right) + w_k \tag{3.13}$$

$$y_k = e\left(x_k, u_k\right) + v_k \tag{3.14}$$

with the differentiable functions f and e. If the time deviation of these two functions is small, they can be approximated by the first order Taylor expansion. Furthermore, the functions are evaluated at the latest state approximation: either $\hat{x}_k^+$ or $\hat{x}_k^-$. This procedure distinguishes the difference between the LKF and the EKF.
Considering these assumptions, the matrices $\mathbf{A}$ and $\mathbf{H}$ from Eq. 3.1 and 3.2 can be redefined:

$$\mathbf{A}_k \coloneqq \left.\frac{\partial f\left(x_k, u_k\right)}{\partial x_k}\right|_{x_k} \tag{3.15}$$

$$\mathbf{H}_k \coloneqq \left.\frac{\partial e\left(x_k, u_k\right)}{\partial x_k}\right|_{x_k} \tag{3.16}$$

Eq. 3.15 and Eq. 3.16 are usually called Jacobian matrices. Taking these variations into account, the algorithm of the EKF works analogously to the LKF in Section 3.1. The complete algorithm derivation can be found in [3; 36; 77; 160].

3.2.2 Adaptive extended Kalman filter

Due to the EKF, it is possible to apply the KF to non-linear systems. However, there are systems whose dynamical processes and parameters cannot be identified accurately. This leads to inaccurate estimations by the KF.
To solve this problem the system's remaining degrees of freedom can be used by the process noise and the measurement noise. The right choice of these values induces a fast transient response and an accurate estimation of the state [19; 32; 38]. Furthermore, due to changing external influences (e. g. temperature) which manipulate the approximation, the process noise and the measurement noise can be adapted in every time-step [53].
The idea is to use the average value of the deviation of the measured and the predicted mea-

surement value at the latest time-step instead of the measurement noise value, which averages over all possible states of the random variables. Although this contradicts the minimising property of the Kalman gain, the replacement includes the real behaviour of the system into the KF. This can be implemented by calculating the moving average V^{ϕ} of the deviation from the measurement:

$$V_k^{\phi} = \frac{1}{\phi} \sum_{m=k-\phi+1}^{k} (U_k - y_k)(U_k - y_k)^t \tag{3.17}$$

with window size $\phi \leq k$ and $\phi \in \mathbb{N}$. Based on the averaged error, the measurement noise and the process noise matrix is updated as follows [19; 32; 38]:

$$r_k = V_k^{\phi} + \mathbf{H}_k \mathbf{P}_k^{-} \mathbf{H}_k^t \tag{3.18}$$

$$\mathbf{Q}_k = \mathbf{K}_k V_k^{\phi} \mathbf{K}_k^t \tag{3.19}$$

The rest of the algorithm is identical to the EKF explained in Section 3.2.1.

3.2.3 Unscented Kalman filter

Section 3.1 describes the KF in its original form assuming a linear model and/or Gaussian distributed random variables. In Section 3.2.1 a solution for models, which can be approximated by linearisation, is shown. However, the system can be neither linear nor the state Gaussian distributed. Furthermore, the influence of the noise can also be non-linear. Consequently, the state-space equation and measurement equation are

$$x_{k+1} = f\left(x_k, u_k, w_k\right) \tag{3.20}$$

$$y_k = e\left(x_k, u_k, v_k\right) \tag{3.21}$$

with the differentiable functions f and e. In Section 3.1 it is shown, that the formalism of the KF works if the random variable is Gaussian distributed. So, the solution of the problem is to claim that the state, which is considered, has this characteristic. Therefore, the random variable is approximated by other vectors, which is constructed in such a way, that the mean value and the covariance matrix are equal to the parameters of the state. Since the choice of the weights of every sigma point as well as its number is arbitrary, there is no restriction to the selection of these vectors. However, the constructed probability distribution is only an approximation of the Gaussian distribution. Thereby, the mean value and covariance matrix are only equal in the first two moments of a Taylor approximation. If the sigma points are chosen symmetric to the mean value and weight the vectors and their reflection equal to the mean value, then all odd moments are zero, which is equivalent to the Gaussian distribution. Moreover, an additional parameter in the weighting to derive the fourth moments of the Gaussian distribution is introduced.
The algorithm of the UKF is equal to all other KFs with the exception of the approximation

of the Gaussian distribution. Considering the process noise, the determination of $2n+1$ sigma points λ_n is required, with n representing the length of the state vector. Afterwards, the state-space Eq. 3.20 can be used to receive the estimation of the next state. Then the covariance matrices and the measurement equation are calculated. The derivation and the complete algorithm can be found in [67–69].

3.2.4 Central difference Kalman filter

Another KF that is able to estimate non-linear systems without the need of derivatives is the CDKF. Similarly to the EKF, it approximates the state-space equations and the measurement equations to the second order. The approximations of the derivatives by a Taylor series are replaced by Stirling's polynomial interpolation formula [27; 68]. Except the weighting of the evaluation points, the CDKF and the UKF are similar to each other, resulting in a nearly equal estimation accuracy [67]. Here, the UKF uses three parameters (λ_1, λ_2, λ_3) whereas the CDKF uses only one (h). The algorithm is explained in detail in [28; 67].

3.2.5 Square root forms of the unscented and the central difference Kalman filter

A general disadvantage of the UKF and the CDKF is the required computation of the square root of different matrices, due to big computational effort and rounding errors in the Cholesky factorisation. To handle this problem, a QR-decomposition, Cholesky factor updating or efficient pivot-based least squares can be used instead. In this way, the order of magnitude or computation of the state, depending on the dimensions of the covariance matrices, can be reduced by one power. Nevertheless, the estimation accuracy is rarely influenced. [34; 67; 70]

3.2.6 Dual Kalman filter

The DKF introduced in [3–5; 30; 67; 73; 77] consists of two KFs working in parallel. Therefore, the first KF estimates the states x_k (Eq. 2.21) and the second the parameters θ of the ECM and the cell capacity:

$$\theta_k = [R_\mathrm{i}, C_\mathrm{act}, R_1, C_1, \ldots, R_n, C_n] \tag{3.22}$$

The filter estimation sequence contains a prediction step of the state vector and a correction step of the parameters. In this process, the expected states are predicted based on the state-space notation in Eq. 3.1. Due to the fact that the state-space notation does not exist for the parameters of the ECM, a prediction is not possible and the adaptation of the parameters has to be done in the correction step [5; 39]. Accordingly, the parameter prediction θ_k^- results to:

$$\theta_k^- = \theta_{k-1}^+ \tag{3.23}$$

For a dynamic adaptation of the ECM parameters it is essential to consider the parameter process noise $\mathbf{Q}_\theta$ and the measurement noise r_θ of the parameter estimator. This is required due to the missing model description of the ECM parameters. So, only the filter tuning determines the estimation performance.
Since the parameters θ_{k-1}^+ are the input for the state and parameter estimator, a first coupling of the two filters is implemented at the beginning of each cycle k. A second coupling is performed in the correction step, as the predicted state $\hat{x}_k^-$ is considered for the parameter correction [36].

3.3 Filter tuning

The overall performance of the filters is set by the covariance matrix $\mathbf{P}$, the process noise matrix $\mathbf{Q}$ and the measurement noise r. To the authors knowledge, it is not possible to calculate the correct set of tuning parameters for KFs in the field of batteries. The determination of the parameters results from experience and empirical experiments, but in general:

- The process noise matrix determines the model uncertainty [6; 161]: if the diagonal elements of $\mathbf{Q}$ are zero, the filter assumes a perfect model. As a consequence, no correction of the states occurs. High values for $\mathbf{Q}$ increase the estimation error, because the filter assumes continually contributing uncertainty to the states. Therefore, a compromise between the ability to correct inaccurate values and estimation error has to be found.
- The covariance matrix determines the convergence behaviour [6; 161]: if the diagonal elements of $\mathbf{P}$ are zero, the filter assumes accurate initial values. As a consequence, the adaptation of incorrect initial values is performed slowly in contrast to an adaptation with diagonal elements higher than zero (depending on the values for the process noise matrix $\mathbf{Q}$). If the initial state is unknown, high values for $\mathbf{P}$ are recommended. This allows a fast correction of the initial parameters, but can also result in unstable behaviour. Therefore, a compromise between convergence velocity and stability has to be found.
- The measurement noise determines the measurement uncertainty [6; 161]: small values for r assume a high accuracy of the measurement sensors. Consequently, the filter calculates the states based on the measurement[1] and ignores the model[2]. High values for r result in a lower Kalman gain (Eq. 3.10) due to the distrust of the measurement. As a consequence, the correction based on the measurement is reduced and the estimation follows the model without correction. Therefore, a compromise between the ability to correct inaccurate values and estimation error has to be found.

[1] voltage based on the measurement equation
[2] Coulomb counter

Part II

Solution Approach

4 Experimental

For all experiments in this work, the cell introduced in Section 4.1 was used. For the measurements at module level, two battery modules consisting of the same cells were constructed (Section 4.2), whereby the experiments at single cell and module level were performed with the measurement setup shown in Section 4.3. The methods to characterise the cells and to track the progress during the ageing studies (Section 4.6) are explained in Section 4.4 and Section 4.5, respectively. An overview of the experiments with the corresponding cell group (CG) is given in Section 4.7.

4.1 Introduction of examined cells

To obtain representative results for state estimation and cell ageing in battery electric vehicles (BEVs), LICs with typical characteristics for electromobility were required. As the range of BEVs is substantially determined by the energy content of the traction battery, these batteries usually comprise high-energy LICs. Moreover, the traction battery has to provide sufficient peak power for accelerating the vehicle. To meet these requirements, Panasonic NCR18650PD NCA cells with a nominal capacity (C_{nom}) of 2.85 A h were used in this work. They feature a high specific energy of 214 W h kg^{-1}, a high energy density of 577 W h l^{-1} and a low ohmic resistance of approximately 21 mΩ. The operating voltage range of these cells ranges from 2.5 V (U_{min}) to 4.2 V (U_{max}). The data-sheet of the cell can be found in Appendix A.

4.2 Design of the battery modules

To investigate the ageing scalability and the OCV change at module level an ageing study at the module level is performed. Therefore, two identical battery modules were constructed. The requirements included: a realistic size and capacity for an electrical vehicle, an exact temperature measurement, and the possibility to disassemble the series connection to obtain a deeper insight in the local ageing behaviour.

4.2.1 Topology

The modules were designed in an 8s14p cell interconnection topology, which is illustrated in Fig. 4.1a. This topology consisted of eight blocks connected in series, with each block consisting of 14 cells in parallel. This resulted in an operating voltage range from 20 V to

33.6 V and a nominal capacity of approximately 40 A h. A total number of 224 cells was used to construct the two battery modules. These cells were selected out of 250 cells from the same production lot. The matching process is described in Section 4.2.3.

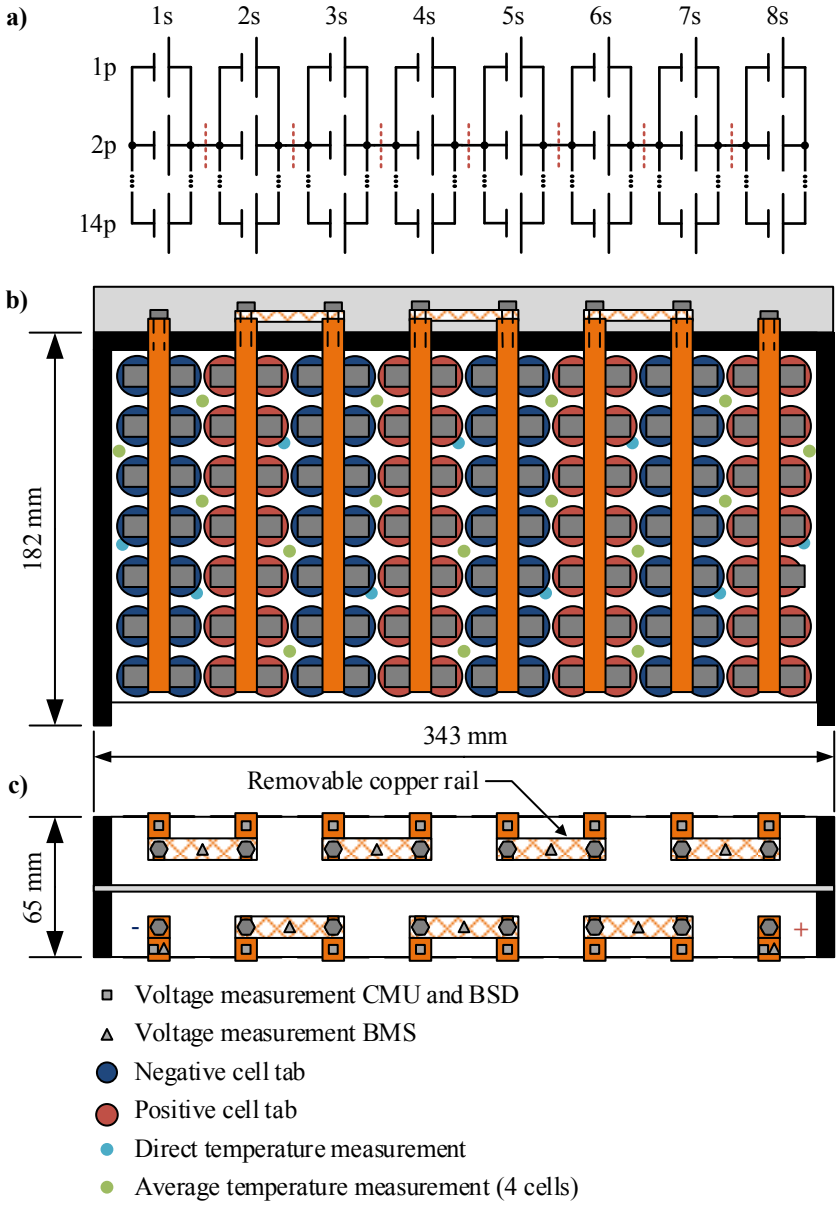

Figure 4.1: Design of the modules in 8s14p topology: (a) schematic representation which illustrates the disassembly points (dashed red lines); technical drawings in top (b) and front view (c), illustrating the positions of the temperature and voltage measurements.

To gain a deeper insight into the ageing behaviour of the module, the series connections of the eight blocks are demountable. This is illustrated in Fig. 4.1a by the dashed red lines. This allowed for separate capacity and resistance measurements for all eight cell blocks to determine interdependencies between the ageing behaviour and the position of the cells within the module. However, the interconnections between the 14 cells of each block were realised as non-removable joints, as removable connectors generally increase the contact resistances

[135]. This would affect the equalisation processes between parallel cells and may distort the ageing behaviour.

4.2.2 Construction

Fig. 4.1b and Fig. 4.1c show the design of the modules. The 112 cells were placed in a frame that was 343 mm long and 182 mm wide, with a spacing between the cells of 1.6 mm and 4.6 mm, respectively. The blue circles symbolise the negative poles and the red circles the positive poles of the cells.
The cell connectors, depicted in grey, were made of 0.2 mm thin nickel-plated steel (Hilumin), which is a steel alloy that can be spot-welded onto the cell poles. The cell connectors were welded to 1.5 mm thick and 10 mm wide copper rails, depicted in orange. During the construction process, the cell connectors were first attached to the copper rails by ultrasonic welding. Afterwards, the produced "ribs" were spot welded onto the cell poles.
Due to the module design, with its removable series connectors, the entire current of the 14 parallel cells of each block had to flow through the current collector rails, depicted in orange. To prevent high power losses and heat generation in the cell connectors, these rails were not made of Hilumin because of its high specific resistance, of approximately $0.1\,\Omega\,\mathrm{mm}^2\,\mathrm{m}^{-1}$. Instead, the current collector rails were made of copper, which provided a substantially lower specific resistance of $0.017\,\Omega\,\mathrm{mm}^2\,\mathrm{m}^{-1}$. In this manner, the power loss of the connectors and hence the cell heating was minimised. Moreover, the module could be disassembled in blocks by untightening the copper rails on the front of the module (Fig. 4.1c).

To investigate the temperature behaviour, 25 temperature sensors were installed in each module. The locations of the sensors are also shown in Fig. 4.1b (cyan and green circles). The cyan circles symbolise PT100 sensors attached directly onto the cell surface by a thermal adhesive, and the green circles symbolise thermocouple sensors placed in the centre of a heat conductive silicone spacer, which retained an equal distance from the four adjacent cells. The two groups of sensors thus enabled measurements of the cell temperatures as well as the average temperatures at different locations inside the module.

4.2.3 Capacity-based cell matching

To perform capacity-based cell matching, the capacity distribution of the used cells had to be measured to exclude outliers. For all 250 cells used in this investigation, the measured and normal distribution is given in Fig. 4.2a for capacities and Fig. 4.2b for ohmic resistances (measured at 1 kHz).
The relative coefficients of variation $\kappa{=}\sigma/\mu$ for the capacity and the resistance are 0.16 % and 0.72 %, respectively. The parameter σ is the standard deviation from the normal distribution [132]. The arithmetic mean value μ of the capacity is 2.88 Ah, and that of the resistance is 21.67 mΩ. Higher κ for resistances were also observed for LICs with other cathode materials

[128; 132], which in turn could lead to a pronounced ageing behaviour for cells connected in parallel (Section 1.2.6 and [138]).

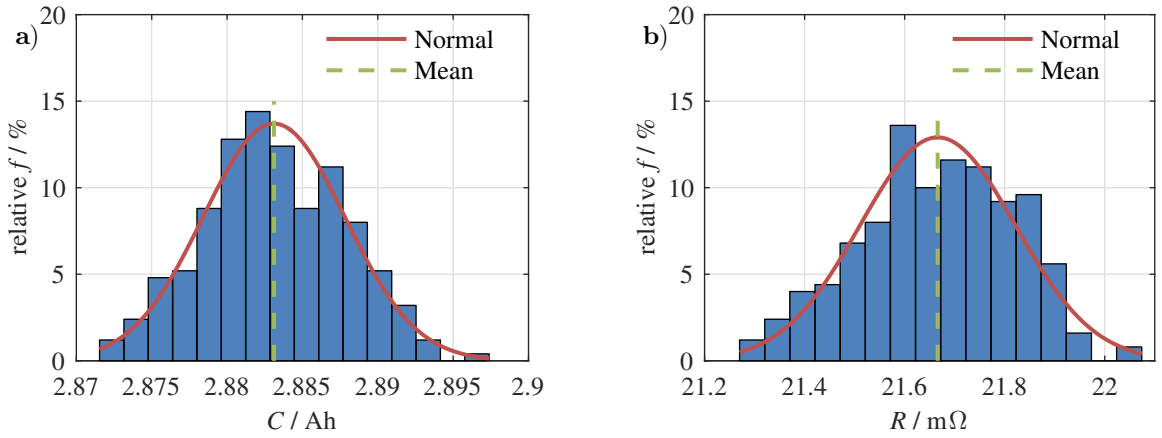

Figure 4.2: Cell matching: (a) normal distribution of capacities at the cell level; (b) normal distribution of ohmic resistances (measured at 1 kHz) at the cell level.

Despite the low tolerances, capacity-based cell matching was performed to guarantee a low balancing effort for the BMS. The objectives of cell matching were to select and connect cells to blocks such that the serial connections would result in a homogeneous capacity distribution in the module. In other words, the module capacities would not be reduced by a weak block, and the BMS would not require continuous balancing. Two (approximately) identical modules were created after the cell matching procedure.

The calculated and measured capacities of the eight blocks of both modules after matching are shown in Fig. 4.3a and Fig. 4.3b, respectively. Thereby, the capacity and resistance values for each block were calculated by:

$$C_{\text{block}} = \sum_{i=1}^{14} C_{\text{cell},i} \tag{4.1}$$

$$R_{\text{block}} = \frac{1}{\sum_{i=1}^{14} \frac{1}{R_{\text{cell},i}}} \tag{4.2}$$

On the basis of these results, the capacities at the module level were observed to be lower. This was attributed to the length of storage time (approximately 4 months) between the single cell measurements and the measurements at the block level. The mean capacity losses caused by calendar ageing were 0.91 % and 0.88 % for module 1 (M1) and module 2 (M2), respectively.

The calculated and measured block resistances are shown in Fig. 4.3c and 4.3d. Here, an increase of the measured resistances compared to the calculated values was observed. The effect of a resistance change due to calendar ageing was considered to be negligible because the contact resistances were the dominant factor for increased resistances in the modules. In [135], the resistance of a spot welded contact (Hilumin to Hilumin) was given as 0.16 mΩ.

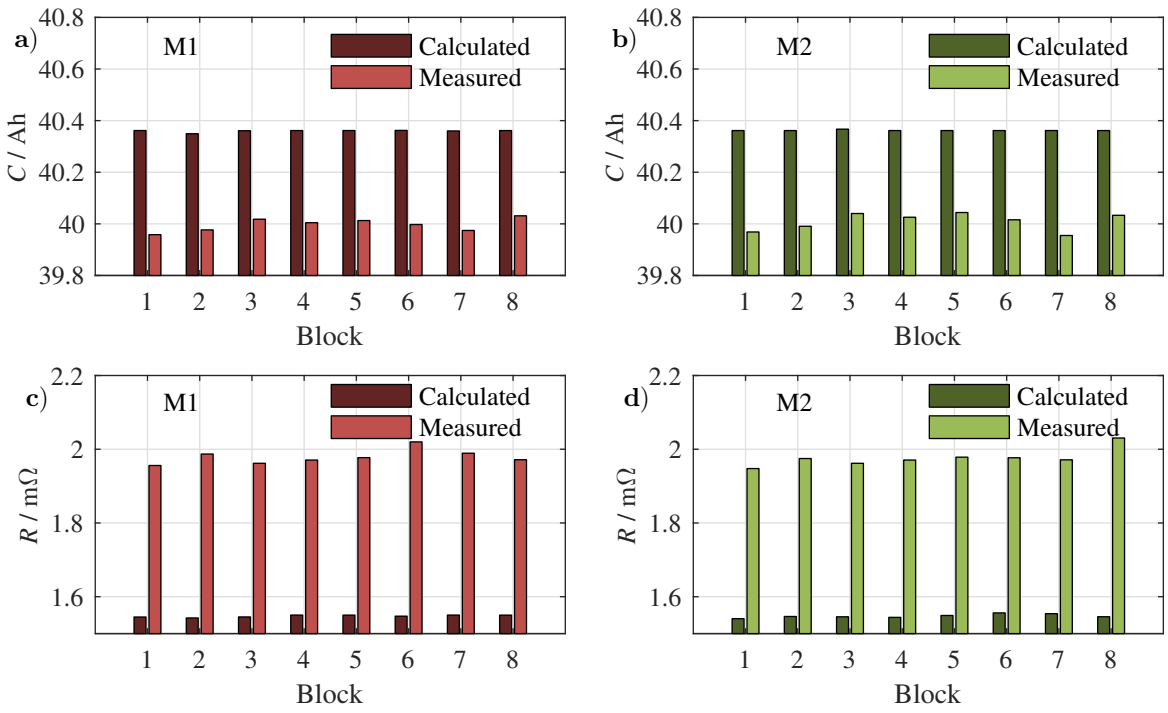

Figure 4.3: Cell matching at 25 °C: measured and calculated capacities of (a) module 1 and (b) module 2; measured and calculated ohmic resistances (measured at 1 kHz) of (c) module 1 and (d) module 2.

For the two poles and 14 parallel cells of one block, this resulted in a contact resistance of R_{contact}=0.16 mΩ·2/14=0.023 mΩ. The mean increase of the block resistances was from 1.55 mΩ to 1.98 mΩ (21.7 %) for both modules, whereas about 5.3 percentage points were related to the contact resistances. The rest was related to the contact resistances between Hilumin and the copper rail and the material itself.

4.3 Measurement setup at single cell and module level

4.3.1 Single cell level

In this work all measurements on single cell level were performed with a BaSyTec cell test system (CTS). For the validation of the state estimation algorithms, measurement data was provided additionally by a less-accurate BMS. To guarantee the functionality of the used algorithm in real applications, cell voltages, temperatures and current were measured by this self-developed prototype BMS [36]. Thereby, the device which provides the reference value must have a higher accuracy and resolution than the device which provides the measurement data for the algorithm.
To realise the experiments at the defined temperatures, the cell was placed in a temperature chamber. In Fig. 4.4, the experimental set-up for the validation is shown. The accuracies and resolutions of the used devices are summarised in Appendix B Table B.1.

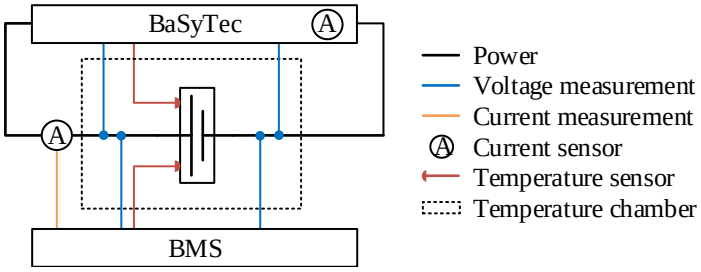

Figure 4.4: Measurement setup on cell level

4.3.2 Module level

For the measurements at module level a module test bench was developed. A BaSyTec high power system (HPS) with two channels was used to cycle the modules with a maximum current of 80 A at a maximum module voltage of approximately 33 V. Each channel had a battery safety device (BSD) for monitoring the single-cell voltages of every block as well as the module temperature. As the BSD only measures with low accuracy in terms of safety, an additional BaSyTec cell measurement unit (CMU) was used to measure the single voltages with high accuracy. The connection terminals for the BSD and CMU are symbolised by a grey square in Fig. 4.1c.

The series connection of several cell blocks could lead to slightly different voltages and SOC levels for the cell blocks due to the manufacturing tolerances of the cells and inhomogeneous ageing or temperature distribution in the module [25]. This imbalance is the reason for cell balancing in battery modules. To process balancing, the modules were supervised by the BMS from Section 4.3.1, which measured every block voltage and the module current. When the voltage difference between the highest and lowest block exceeded the threshold of 5 mV during charging periods, the BMS started the balancing process. The balancing was performed dissipatively by switched 33 Ω resistors. This allowed a balancing current between 75 mA and 127 mA, depending on the block voltage. The connections of the BMS are symbolised in Fig. 4.1c by a grey triangle.

The PT100 temperature sensors, attached directly onto the cell surfaces, were measured with a National Instruments PXI system, and the thermocouples for average temperatures at different locations inside the module with the CMU.

The BMS sent the measured values to the PXI system (Fig. 4.5) via the controller area network (CAN)-bus. In Fig. 4.5a, the setup for the test configuration during cycling is shown. The connectors between the blocks were closed and the HPS loaded the battery module with the driving cycle.
Fig. 4.5b shows the test configuration during check-up for each block. The modules were disassembled and a check-up for each block was performed with an extended cell test system (XCTS). The HPS, BSD and BMS are deactivated, and the CMU only measures temperatures. The ohmic resistance R_i of each block and module was measured with an impedance

measurement device (HIOKI BT3562). The accuracies of the measurement equipment are summarised in Appendix B Table B.2.

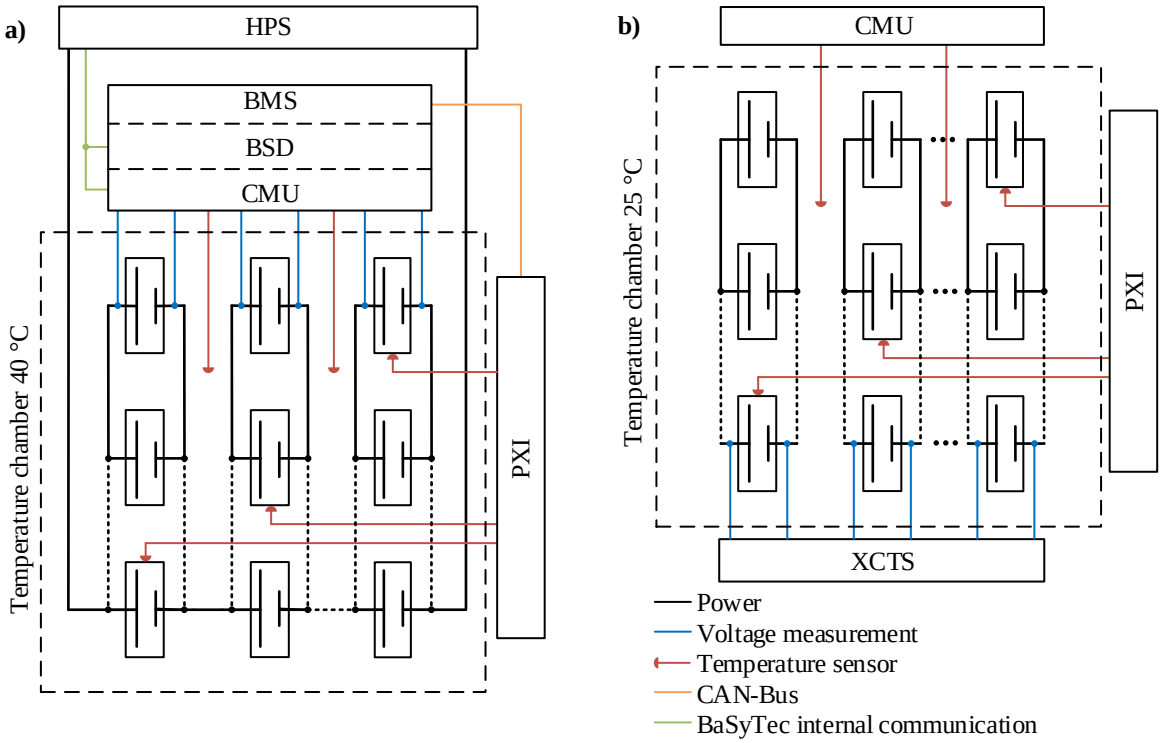

Figure 4.5: Scheme of the module ageing test bench: (a) cycling configuration; (b) check-up configuration.

4.4 Methods used for determining equivalent circuit model parameters

4.4.1 Parameter identification

To determine the cell parameters, current pulses with different amplitudes were applied to the cell over the entire SOC range in steps of approximately 7 % of the nominal capacity. The voltage response of every current pulse was fitted by a least square method to optimise the parameters for the ECM, consisting of one ohmic resistance and one or two RC terms (Fig. 2.1). Therefore, the ohmic resistance R_i was measured by an EIS at 1 kHz at the same SOC levels. The parameter fitting was calculated separately for the one and two RC term model. This procedure was repeated at −10 °C, 0 °C, 10 °C, 25 °C and 40 °C and for different current rates (−1 C, −0.75 C, −0.5 C, −0.25 C in discharge direction and 0.5 C in charge direction).

4.4.2 Open circuit voltage determination

In this work both OCV determination methods introduced in Section 2.1 were used. For the CC-OCV the NCA cell was charged to the maximum allowed voltage $U_{\max}$ and discharged to the minimum allowed voltage $U_{\min}$ with a constant current of 0.01 C.
To induce the same polarisation effects during loading compared to the CC method, the same current of 0.01 C was used for the IC method. Here, the cell was charged and discharged in 10 % steps with a relaxation time of 3 h in between. The OCV at a SOC of 100 % or 0 % was determined by a constant-current constant-voltage (CCCV) charge or discharge, respectively. Therefore, the cut-off current was set to 0.005 C.
To ensure the same SOC levels of the steps for both directions the precise Coulomb counting of the CTS was used. The charge and discharge direction was averaged for both methods to minimise hysteresis effects and, in the case of the CC method, to compensate the influence of the impedance. Both measurement procedures were repeated for all considered temperatures.

4.5 Methods used for cell diagnosis

A check-up routine was used to determine the condition and to track the degradation of the lithium-ion cells and modules. This routine consisted of capacity and resistance measurements. At the module level, the spread among cell blocks (group of 14 cells in parallel) was also evaluated by a newly introduced parameter, which is the state of inhomogeneity (SOI).

4.5.1 Capacity measurement

To determine the capacity, the cell was fully charged with a CC of 0.5 C and a constant-voltage (CV) of the maximum allowed voltage $U_{\max}$ (for the tested cell 4.2 V), until the current dropped below 0.02 C. This corresponds to a SOC of 100 %. After that, the cell was discharged with a CC of 1 C to the minimum allowed voltage $U_{\min}$ (for the tested cell 2.5 V), followed by a CV period with a cut-off current of 0.02 C, corresponding to a SOC of 0 %. The additional CV charge and discharge period was required to reduce the impacts of the cell impedance, and the cell temperature, on the measurement of the actual capacity [162]. The C-rate in this work is related to the nominal capacity.

For the measurements obtained at the module level, the voltage limits were multiplied by the amount of cells connected in series. The charge and discharge currents were multiplied by the amount of cells connected in parallel. At the module level, a CCCV discharge was not possible because the discharge process had to be stopped when the first block reached the lower voltage limit. The described check-up routine was performed at 25 °C.

4.5.2 Resistance measurement

After the capacity measurement, the check-up routine charged the cells and modules to 50 % of their measured capacity. At this SOC, the internal resistance R_i was determined to monitor the changes in cell impedance. This value represents the real part of the cell impedance at 1 kHz, and is determined by an excitation of the cells or modules with a sinusoidal current. Therefore, the resistance was measured with the HIOKI BT3562, which directly measured the resistance at 1 kHz.

4.5.3 State of inhomogeneity

To identify the increasing inhomogeneity between the blocks within each module during the progress of ageing, a new state, referred to as SOI, was defined. The SOI reveals the spread between the maximum and minimum value of a battery parameter in percent:

$$SOI_X = \frac{X_\mathrm{max} - X_\mathrm{min}}{X_\mathrm{max}} \tag{4.3}$$

where X can refer to the capacity, ohmic resistance or temperature. The concept of the SOI can also be transferred to other parameters and used both for single cells and modules.

4.5.4 Differential voltage analysis

The differential voltage analysis (DVA) is an enhanced method to characterise a LIC. Therefore, the derivative of the OCV is related to the derivative of the corresponding charge throughput. The DVA allows a separate consideration of different ageing mechanisms. [123]
In this work, the resulting DVA spectra are related to the actual capacity.

4.6 Ageing study at single cell and module level

To investigate the ageing behaviour at single cell and module level an ageing study is performed. The aim of these studies is to show the scalability of ageing and the change in OCV. This is essential for state estimation at single cell and module level during lifetime.
For the comparison of cell and module ageing, results from [163] are used. In the ageing study at the cell level, the impact of regenerative braking on battery ageing was examined for a representative driving load profile, derived from the US06 highway driving cycle (see Fig. 4.6a) [163]. This driving cycle was selected because it features frequent load changes and a high charge throughput per time, which was beneficial for accelerated cycle life testing. A vehicle model was used to compute the load currents at the cell level for a BEV with a highway driving range of approximately 100 km. Fig. 4.6b illustrates the load profiles resulting from unrestricted regenerative braking compared with no regenerative braking. [163]

The cells were charged and discharged repeatedly with the following test sequence: At first, the cells were charged with a constant current of 0.25 C (≈700 mA) to their assigned charging voltage. After a pause of 5 min, the cells were discharged, with two subsequent runs of a driving load profile, with a pause of 1 min after each run. Before the cycle life testing and after 400 repetitions of the charging and discharging sequence, a check-up was performed to track the ageing of the cells.

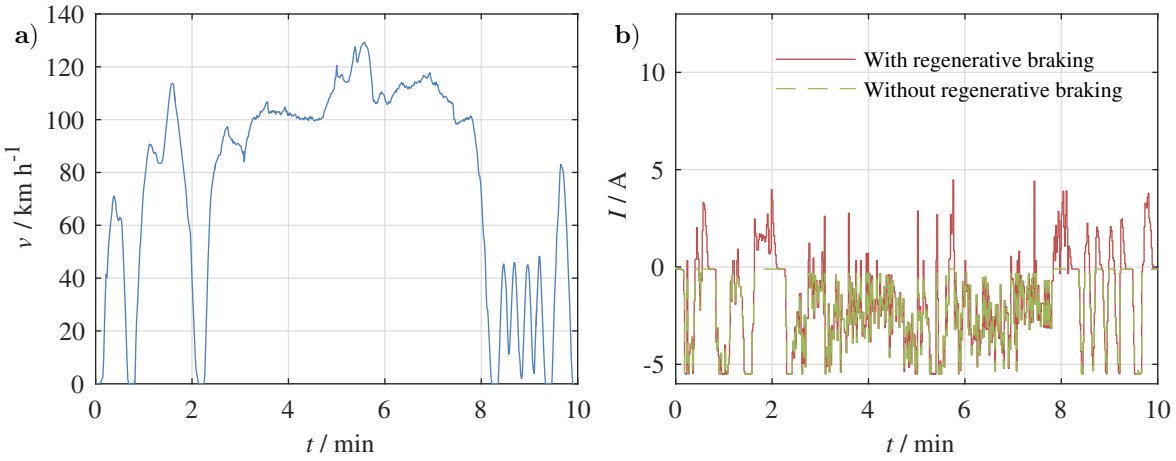

Figure 4.6: US06 highway driving cycle: (a) velocity profile; (b) load current at the cell level with unrestricted regenerative braking and without regenerative braking. [163]

Since the depth of discharge (DOD) was about 25 %, the check-ups were always performed after a charge throughput of approximately 100 equivalent full cycles (EFC). For the vehicle configuration, this corresponded to a driven distance of approximately 10 000 km.

The different test conditions in the ageing study at the cell level comprised three temperatures (10 °C, 25 °C and 40 °C), four levels of regenerative braking (from unrestricted regenerative braking to no regenerative braking at all) and three SOC operating windows (high, medium and low SOC), resulting from three different charging voltages (3.7 V, 3.9 V and 4.1 V). In addition to the cells, which were cycled repeatedly, other groups of cells from the same production lot were stored at eight different SOC levels and temperatures, from 10 °C to 55 °C, to examine the calendar ageing at the different SOC regions. For each test condition, one new cell was used. [163]
The results from five months of testing [163], covering a driven distance of 50 000 km, showed that for all three temperatures, the fastest ageing occurred in the high SOC operation with no regenerative braking at all. The increased battery ageing resulting from the load profile without regenerative braking was assumed to be attributed to a higher depth of discharge at the end of the driving sequence, as no charge was recovered during braking periods. Moreover, a high SOC is also known to increase calendar ageing. [163]

In order to compare the ageing behaviour of the module level with that of the single cell level, comparable test procedures were used. From the test conditions at the cell level, the most stressful load profile was selected. Hence, the tests at the module level were performed at the

high SOC operating window at 40 °C with no regenerative braking.
The current of this load profile was multiplied by the number of cells in parallel. So, the same average load per cell as in [163] was yielded. To compare battery ageing at the single cell and module level, single LIC and modules consisting of 112 cells were investigated. For each study, all examined cells belonged to an identical production lot. All cells were examined with the check-up routine presented in Section 4.5 before the module construction, as well as before the start of ageing experiments.
The modules were cycled in a temperature chamber which kept the ambient temperature at about 40 °C. After 100 EFC, the check-up of the modules was performed with a CC discharge at approximately 25 °C.

To investigate the OCV during ageing, a separate ageing study was performed in this work, with the same conditions as described above. The cyclic ageing behaviour was investigated at 25 °C and 40 °C at the low (L) and high (H) SOC level (3.7 V and 4.1 V). The calendar ageing was additionally performed at 10 °C at both SOC levels. To track the OCV changes, the check-up routine was extended with the OCV determination by a constant current described in Section 4.4.2.
Due to the comparably long check-up routine, this ageing study is not comparable with the ageing study at module level. In Table 4.1 the ageing experiments at single cell and module level are summarised.

Table 4.1: Matrix of the cyclic and calendar ageing experiments at single cell and module level. L corresponds to the low SOC level (3.7 V), H corresponds to the high SOC level (4.1 V). The green tick symbolises the amount of cells or modules per ageing condition, the red cross symbolises conditions not considered.

		L/10 °C	H/10 °C	L/25 °C	H/25 °C	L/40 °C	H/40 °C
Cell	cyclic	✗	✗	✓✓	✓✓	✓✓	✓✓
	calendar	✓	✓	✓✓	✓✓	✓✓	✓✓
Module	cyclic	✗	✗	✗	✗	✗	✓✓
	calendar	✗	✗	✗	✗	✗	✗

4.7 Overview of experiments

During this work, several experiments were performed with different cells of the aforementioned Panasonic NCR18650PD NCA cell (Section 4.1). Therefore, in Fig. 4.7 the experiments are categorised in CGs. The vertical position of the single blocks symbolises the time progress. With CG1, OCV and pulse measurements are performed to calculate the parameters of the used one and two RC term ECM (Section 4.4) of a new cell. Due to the low cell-to-cell variation (Section 4.2.3) two different cells, one for the OCV and one for the pulse measurement are used to reduce measurement time. With this experiment the dependencies of the ECM elements of new cells are investigated in Chapter 6.

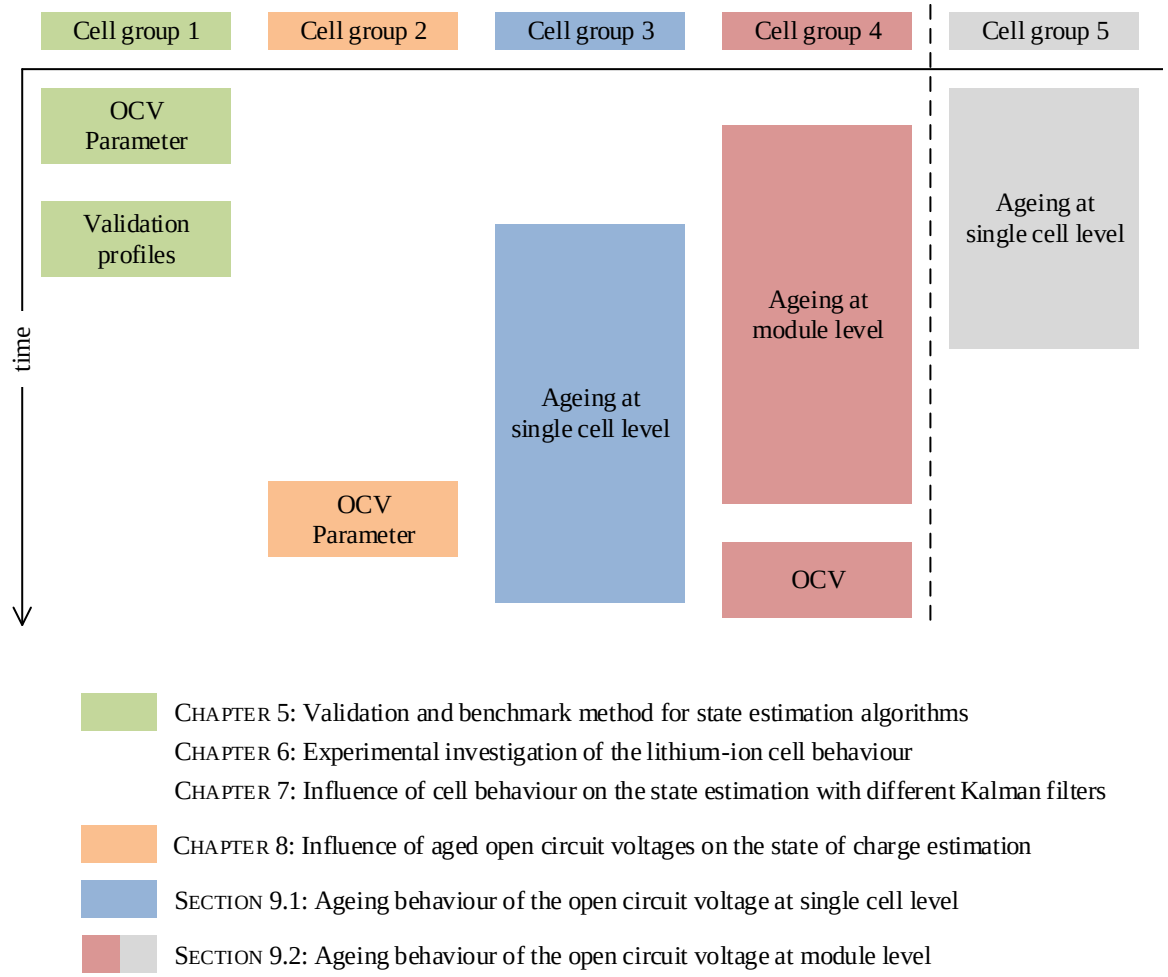

Figure 4.7: Overview of the performed experiments on cell and module level. Cell group 5 correspond to results of [163].

In parallel, the validation method for state estimation algorithms was developed (Chapter 5). The required measurements were performed with the same cell as used for the OCV measurements (CG1). These results and the cell parameters of CG1 were used for the KF comparison study in Chapter 7.

To investigate the influence of change in OCV on the SOC estimation with KFs (Chapter 8), the experiments to determine the ECM elements and the OCV were repeated with three cells in different ageing states (CG2). In Table 4.2 the history of these cells, given in EFC at different conditions, is summarised with the resulting state of health (SOH). Therefore, the SOH is the ratio between the actual capacity C_{act} and the nominal capacity C_{nom}. The ageing study of these cells is not a topic of this work.

The cells of CG3 and CG4 were used for the two ageing studies in this work (Chapter 9). The ageing study at single cell level (CG3) gives a deeper insight into the OCV changes (Section 9.1) during lifetime, whereas the ageing study at module level (CG4) aims to investigate the ageing scalability. Therefore, the study of ageing at module level was started first. To

Table 4.2: Cell history and SOH of the investigated cells (Z1, Z2 and Z3) in CG2.

Cell	Cell history	SOH
Z1	0 EFC	98.3 %
Z2	385 EFC (2.5 V to 4.1 V) at 10 °C	90.4 %
Z3	400 EFC (2.5 V to 4.2 V) at 10 °C	82.5 %

compare the results at module level with the ageing behaviour at single cell level (Section 9.2), previously available results from the ageing study of Keil et al. were used (CG5) [163]. At the end of the ageing study at module level, OCV measurements at module, block and single cell level allow the investigation of the OCV change during lifetime.

5 Validation and benchmark method for state estimation algorithms

Section 1.2.3 showed the shortcomings of actual validation methods. Furthermore, Chapter 2 presented the non-linear behaviour of LIC at different temperatures, SOC levels and ageing states. Consequently, an enhanced validation method is required, to survey the functionality of state estimation algorithms.
To consider different operational conditions, three validation scenarios are created based on standardised driving cycles. For this purpose, existing driving cycles are analysed to identify dominant time constants (Section 5.1). With this information, a synthetic load cycle (SLC) is generated (Section 5.2), which is used for the three validation profiles (Section 5.3). To allow a comparison of different algorithms, a benchmark method for performance evaluations is presented in Section 5.4.

Parts of this chapter were previously published in [141].

5.1 Analysis of driving profiles

It is already stated that the dynamic response of LICs strongly depends on temperature, SOC, load current and ageing. The quality of the state estimator is determined by its ability to provide accurate results under different operating conditions. The comparability can be achieved by applying an identical test profile. The driving cycle analysis, which gives the foundation for the derivation of such a test profile, is described in the following.

Any signal in the time domain can be represented by a power distribution in the frequency domain. If the signal is periodic, then the power distribution will be dominated by the corresponding frequency components. In the case of vehicle driving cycles, these periodic processes could be linked to repeated acceleration or braking while driving. Waiting at traffic lights, as well as other frequent interruptions of vehicle movement, belong to periodic processes as well. In total, 149 reference velocity profiles from [164] are transformed using the common vehicle model presented in [165, p. 77] to extract power profiles. The power requirements are derived from the velocity profile based on this vehicle model, with the parameters summarised in Appendix C. Due to the diverse origins and purposes of these driving cycles, all profiles are normalised according to their maximum power. Since not all power profiles are neutral in terms of acceleration and recuperation power, the direct component is eliminated by subtracting the profile average value from itself. Such adjustments are assumed to be valid since

only the dynamic information is of particular interest.
Adapted profiles are subsequently transformed to the frequency domain using a fast Fourier transformation (FFT) algorithm. The first four dominating frequencies are determined for each profile. A sample result, based on the *Artemis HighMot urbdense total* driving cycle (distance: 3086 m; duration: 787 s; average speed: 14.1 km h^{-1}) [164], is shown in Fig. 5.1.

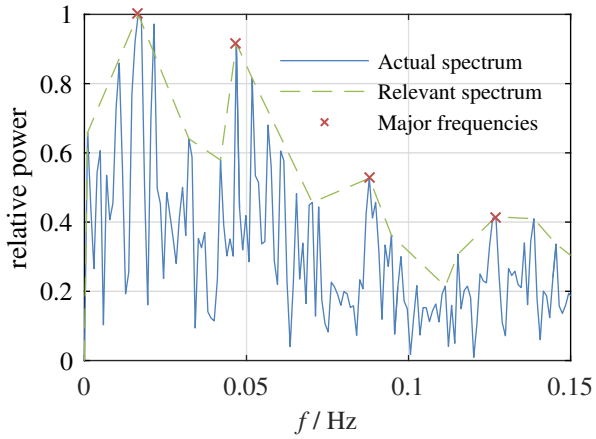

Figure 5.1: Creating an application-independent test profile: dominant frequencies after a local peak search of the *Artemis HighMot urbdense total* driving cycle

It has to be mentioned that the major frequencies-finding algorithm does not simply take the first highest values in the power spectrum. Such an algorithm would result in closely lying major frequencies, which owe their existence to the leakage effect of discrete Fourier transformation (DFT). The actual algorithm replaces the initial spectrum by linear interpolation of local maxima, which is shown in Fig. 5.1. The process is iterated until the interpolated spectrum has only the desired amount of peaks. For driving cycle frequency analysis, this number is set to four.

5.2 Generation of an application-independent test profile

Table 5.1 holds the averaged major time constants τ_{dc} of all adjusted power profiles sorted in descending order of corresponding power magnitudes. The major time constants, which could be extracted by analysing the driving cycles, as described in Section 5.1, provide the basis for the dynamic validation profiles. Additionally, the most commonly used sample time τ_{s}=1.0 s within the analysed driving cycles is appended [164]. So, the Nyquist theorem is guaranteed, according to which, the sample rate f_{s} has to be twice the highest frequency f_{max} to reconstruct the signal (f_{s}=2 · f_{max}). Using the four time constants and the appended sample time τ_{s}, a dynamic load profile A is generated by the sum of sine waves with ascending sample and hold times τ_{sh} and its corresponding power distribution a:

$$A(t) = \sum_{i=1}^{5} \left(a_i \cdot \sin\left(\frac{2\pi}{\tau_{\mathrm{sh},i}} \cdot t \right) \right) \tag{5.1}$$

with

$$[A(t)] = \frac{\mathrm{kW}}{\mathrm{kW_{peak}}}$$

Depending on the application, and hence, different measurement possibilities, the sampling rate of the system varies between seconds and minutes. To validate the algorithm or model for different sampling rates, the sample and hold time τ_{sh} is modulated. Therefore, the number of periods N with a constant sample and hold time τ_{sh} is rounded to its next integer value (Table 5.1).

Table 5.1: Major time constants and sample rates for discretisation.

Time constant τ_{dc}	Number of Periods N	Sample and hold time τ_{sh}
55.82 s	1	55.82 s
9.023 s	6	9.014 s
5.144 s	10	5.140 s
3.860 s	14	3.859 s
τ_{s}=1.0 s	55	1.015 s

To generate the quantised signal with different step sizes, the dynamic load profile is repeated five times. Both half cycles for each sample and hold time define one time step $\Delta t_j = t_{j+1} - t_j$ wherein the average load is calculated. Combining all time steps generates a quantised signal S with a decreasing step size, which is equal to the sample and hold time:

$$S(t_j) = \sum_{i=1}^{5} \left(\sum_{j=0}^{2N_i-1} \frac{\int_{t_j}^{t_{j+1}} A(t)\,dt}{\frac{\tau_{\mathrm{sh},i}}{2}} \right) \tag{5.2}$$

where

$$t_j = j \cdot \frac{\tau_{\mathrm{sh},i}}{2}$$

$$[S(t_j)] = \frac{\mathrm{kW}}{\mathrm{kW_{peak}}}$$

To equalise the different load quantities in charge and discharge directions, without interfering with the frequency spectrum, the profile is extended by the vertically and horizontally mirrored profile. Another advantage is the additional behaviour of the prehistory, whether the cell is stressed intensively or fairly steadily. In conclusion, the generated profile is repeated 10 times to validate the full bandwidth of the load scenarios with all five sample and hold times in ascending and descending orders (Section 5.2). This Coulomb neutral SLC is used as a subset for the different validation scenarios. To achieve a cell-independent profile, the relative power profile is divided by the nominal voltage of the used cell and scaled to the maximum current of the cell.

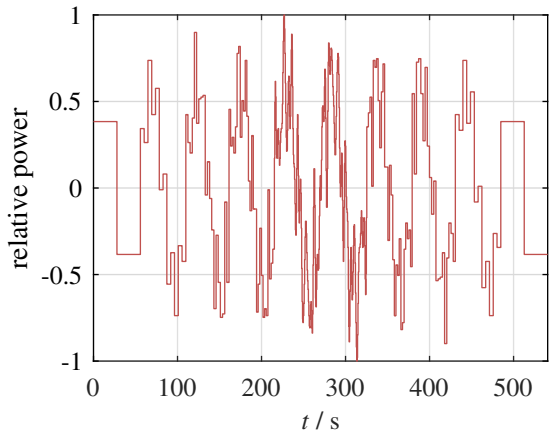

Figure 5.2: Creating an application-independent test profile: the discrete profile with the corresponding sample rates (Eq. 5.2).

5.3 Validation scenarios

With the SLC and the information about cell behaviour, the validation profiles can be developed. To validate the stability of the state estimators during low-dynamic (profile A), high-dynamic (profile B) and long-term tests (profile C), three independent validation profiles are created. To guarantee a reproducible validation, at the beginning of every profile, a complete CCCV charge and discharge is performed to determine the actual capacity, as described in Section 4.5.1. The process is shown in Fig. 5.3 phase 1.

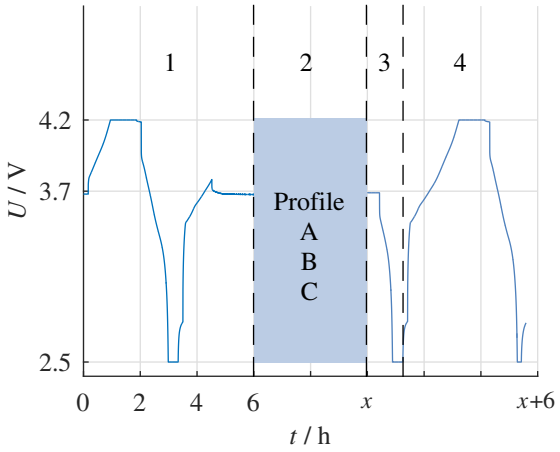

Figure 5.3: Validation profiles for a NCA cell: sequence of the validation process for each profile (1: capacity measurement and initial SOC conditioning; 2: profile A, B or C; 3: residual charge measurement; 4: capacity measurement). The variable x depends on the duration of the profiles.

At the end of each validation profile A, B, or C (Fig. 5.3 phase 2), a residual charge determination is performed by a CCCV discharge (Fig. 5.3 phase 3) with the same constraints as that of the capacity determination. In order to calculate the final SOC based on the residual charge and to consider a capacity fade during long-term tests (profile C), the capacity is measured again (Fig. 5.3 phase 4).

5.3.1 Profile A

Profile A (Fig. 5.4) aims to validate the low-dynamic behaviour of a state estimator. Several CC charges and discharges are performed. Relaxation times and the Coulomb neutral SLC are placed between single CC periods. To investigate the behaviour of the state estimator with strongly changing parameters over the SOC range, this profile is performed at SOC levels where the parameters differ the most (compare Section 2.1). The distinctive parameter values of most of the LICs can be found at about 10 %, 50 % and 90 % SOC. Initially, the cell is charged from 50 % to 90 %. After a relaxation period of 30 min, SLC is performed. Subsequent to a second rest period of 30 min, the cell is discharged to the next SOC level of 50 % or 10 %. This procedure is repeated at −10 °C, 0 °C, 10 °C, 25 °C and 40 °C to investigate the temperature behaviour of the state estimator for low-dynamic profiles.

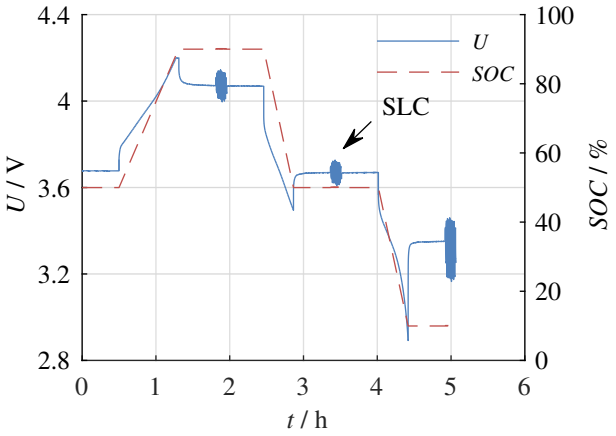

Figure 5.4: Validation profiles for a NCA cell: profile A for low-dynamic.

5.3.2 Profile B

While validation profile A needs a Coulomb neutral profile to ensure a steady SOC at the considered SOC levels, validation profile B (Fig. 5.5) comes with an additional direct current (DC) offset. The amount of continuous discharge depends on the recuperation rate of the driving cycles analysed in Section 5.1. Therefore, all driving profiles are normalised in power and time. Afterwards, all load levels are rearranged in descending order of their magnitudes, resulting in a common load duration curve. Cumulatively, for the recuperation levels of the average load duration curve, around 11.35 % of the discharged energy is recuperated. The discrete SLC is shifted towards its discharge direction until the recuperation satisfies this requirement. Dividing the power profile by the nominal voltage results in the current profile. While profile A validates the behaviour of estimation algorithms during rest and CC periods, profile B investigates the dynamic behaviour within the SOC range of 10 % to 90 %. The charging period from 50 % to 90 % between phase 1 and phase 2 (Fig. 5.3) is not considered. Analogous to profile A, the same ambient temperatures of −10 °C, 0 °C, 10 °C, 25 °C and 40 °C are performed for profile B to investigate the temperature behaviour of the state estimator

for high-dynamic profiles.

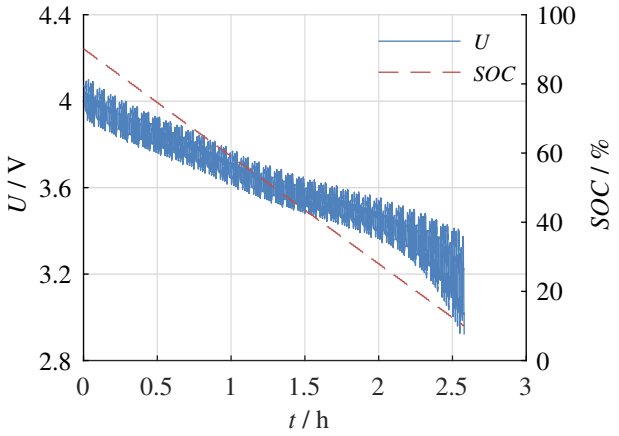

Figure 5.5: Validation profiles for a NCA cell: profile B for high-dynamic.

5.3.3 Profile C

The purpose of validation profile C is to investigate the long-term stability and accuracy during varying temperatures in the range from −10 °C to 40 °C. Validation profile C uses the Coulomb neutral SLC as in profile A. SOC is maintained constant at 50 % and SLC continually repeats itself for seven days.

Fig. 5.6 shows the first 32 h of profile C. The temperature cycling starts (t_S) and ends (t_E) at 25 °C. In between, the five ambient temperature levels (−10 °C, 0 °C, 10 °C, 25 °C and 40 °C) are kept constant for two hours, while the incline or decline to the next temperature level takes one hour. Except the boundary temperatures of −10 °C and 40 °C, every temperature level is set twice. In total, the complete temperature range is cycled in 24 h and repeated for seven days.

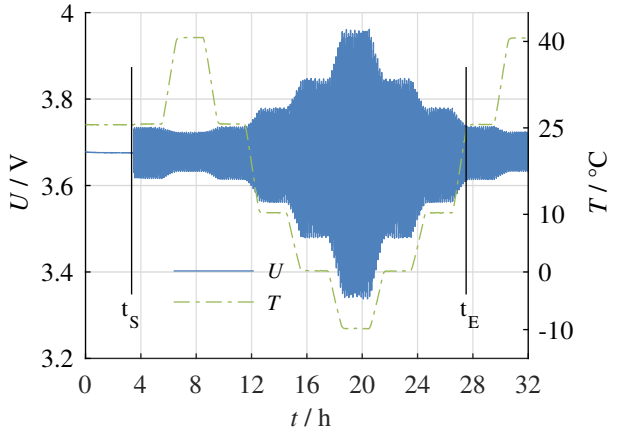

Figure 5.6: Validation profiles for a NCA cell: one of the seven cycles of profile C for the long-term test (temperature cycle start: t_S; temperature cycle end: t_E).

5.4 Benchmark of state of charge estimation algorithms

To guarantee the comparability between state estimators, a standardised evaluation system needs to be defined. In this section, such a system is proposed. Similar to [45], a scoring system from 0 (worst) to 5 (best) points is applied.

In this section, the six categories of the evaluation system are explained: estimation accuracy K_{est}, drift behaviour K_{drift}, residual charge determination K_{res}, transient behaviour K_{trans} and failure stability K_{fail}.
For the evaluation, several error boundaries ε are defined. Each of them corresponds to an evaluation score $P(\varepsilon)$. Eq. 5.3 shows the score depending on the defined error boundaries. In every category the same values are used.

$$P(\varepsilon) = \begin{cases} 5 & \text{for} \quad 0\,\% \leq |\varepsilon| \leq 0.5\,\% \\ 4 & \text{for} \quad 0.5\,\% < |\varepsilon| \leq 1\,\% \\ 3 & \text{for} \quad 1\,\% < |\varepsilon| \leq 2\,\% \\ 2 & \text{for} \quad 2\,\% < |\varepsilon| \leq 4\,\% \\ 1 & \text{for} \quad 4\,\% < |\varepsilon| \leq 8\,\% \\ 0 & \text{for} \quad |\varepsilon| > 8\,\% \end{cases} \tag{5.3}$$

5.4.1 Estimation accuracy K_{est}

Here, the overall accuracy during cycling is evaluated for all profiles. The estimation accuracy depends on the total time within a certain error boundary ($\sum \Delta t_{\delta \in \varepsilon}$) in relation to the total measured time t_{end} (see Fig. 5.7). Thereby, δ describes the absolute difference between the reference SOC_{ref} provided by the CTS, and the estimated SOC_{est}:

$$\delta = |SOC_{\text{ref}} - SOC_{\text{est}}| \tag{5.4}$$

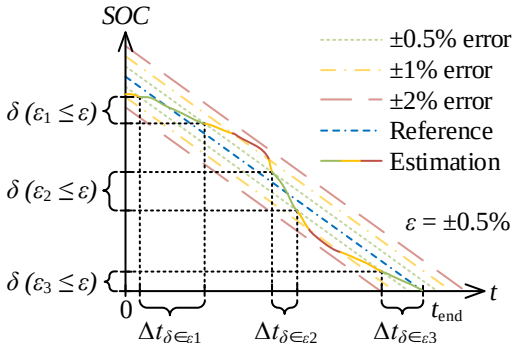

Figure 5.7: Validation principle: evaluation of the estimation accuracy (example with profile B and error boundary ε=±0.5 %, not all boundaries shown).

The resulting percentage part of the total time is then multiplied with the corresponding point

$P(\varepsilon_i)$. This is calculated for all six error boundaries and summed for K_{est}:

$$K_{\text{est}} = \sum_{i=1}^{6} \left(P(\varepsilon_i) \cdot \frac{\sum \Delta t_{\delta \in \varepsilon_i}}{t_{\text{end}}} \right) \tag{5.5}$$

The sum of all t_δ corresponds to t_{end}.

5.4.2 Drift behaviour K_{drift}

A repeating discharge profile results in an overall linear SOC trend with a certain gradient. In short validation profiles, a difference between the reference and estimation gradient, caused by wrong parameters or measurement errors, generates a negligible error. However, in long validation tests or in real applications, this differing gradient can provoke an accumulating error and the estimation drifts. When the estimation has the same gradient as the reference, despite the mentioned reasons, the state estimator can correct any current offset or other shortcomings. To examine this behaviour, an investigation of the estimation drift is essential (Fig. 5.8).
Due to possible small transients at the beginning, or a non-linear estimation, the regression line of the estimation error is calculated.

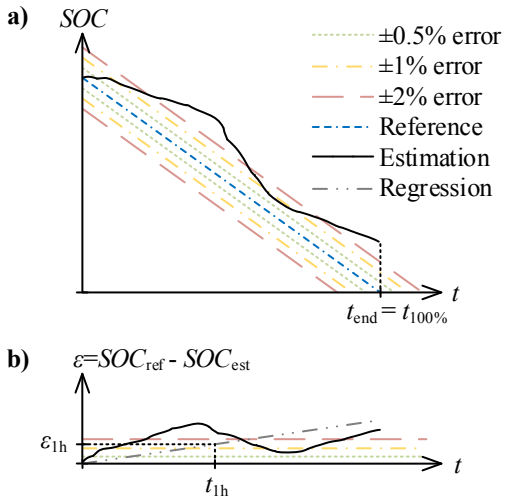

Figure 5.8: Validation principle: (a) estimation with drift (example with profile B, not all boundaries shown); (b) linear regression of the estimation error gives the average drift error $P(\varepsilon_{1\,\text{h}})$

To calculate the average drift score K_{drift}, the gradient G of the regression line z is multiplied with the time $t_{1\,\text{h}}$:

$$\begin{aligned} z &= G \cdot t + b \\ \varepsilon_{1\,\text{h}} &= G \cdot t_{1\,\text{h}} \\ K_{\text{drift}} &= P(|\varepsilon_{1\,\text{h}}|) \end{aligned} \tag{5.6}$$

with

$$[\varepsilon_{1\,\mathrm{h}}] = \frac{\%}{\mathrm{h}}$$

For profile A, the drift corresponds to the mean of the drift scores during the CC charge and discharge periods. Due to the long duration of profile C, the error per hour results in a negligible error, even when the error increases to several percent per week. To consider such a drift in the evaluation, the error for long-term tests (tests with a duration of at lest 7 d) is related to one week:

$$[\varepsilon_{7\,\mathrm{d}}] = \frac{\%}{7\,\mathrm{d}}$$

The drift score correlates with the estimation score. A low drift score results in a low estimation score, because the estimation is drifting apart. This has a high influence during long-term investigations (profile C). However, if the drift score is high and the estimation score is low, the estimation is not drifting but has a parallel offset. For Coulomb counter based algorithms, for example KF, this can be provoked by incorrect parameters or voltage measurement errors. When the estimation is oscillating, the linear regression could result in a falsified drift value. So, a long transient oscillation around the correct SOC value can result in a high estimation score but a low drift score. This context is summarised in Table 5.2. This correlation can determine the reason for low estimation performance.

Table 5.2: Possible relationship between K_{est} and K_{drift}

	low K_{drift}	high K_{drift}
low K_{est}	drifting (e.g. current offset)	parallel offset (e.g. wrong parameters)
high K_{est}	transient oscillation	all Ok

5.4.3 Residual charge determination K_{res}

During cycling, the reference is influenced by accumulated errors, due to the limited sample time and measurement errors. Furthermore, the reference SOC is related to the cell capacity, which may change due to a varying temperature during testing. Hence, the available capacity differs and the reference is falsified as a consequence. The residual charge at the end of a cycle related to the actual capacity represents the true SOC_{res}. The resulting error bound yields the evaluation points for this category:

$$K_{\mathrm{res}} = P(|\varepsilon|) \tag{5.7}$$

with

$$\varepsilon = SOC_{\text{est,end}} - \frac{C_{\text{res}}}{C_{\text{act}}} = SOC_{\text{est,end}} - SOC_{\text{res}} \tag{5.8}$$

where C_{res} is the remaining capacity determined by a CCCV discharge at the end of the validation profile (Fig. 5.3, phase 3) and C_{act} is the cell capacity measured after the validation profiles (Fig. 5.3, phase 4).

5.4.4 Transient behaviour K_{trans}

Common state estimation algorithms can compensate for incorrect initial values, measurement errors and changes in parameters, temperature, etc. The investigation of the transient behaviour is performed by initialising the system with incorrect values.
In Fig. 5.9, the evaluation of the transient behaviour is depicted. Here, it is examined which error bound the estimator is in after 10 % of the total time ($t_{10\,\%}$) after an incorrect initial SOC. The percent specification allows for higher algorithm requirements for shorter profiles and lower requirements for long-term tests.

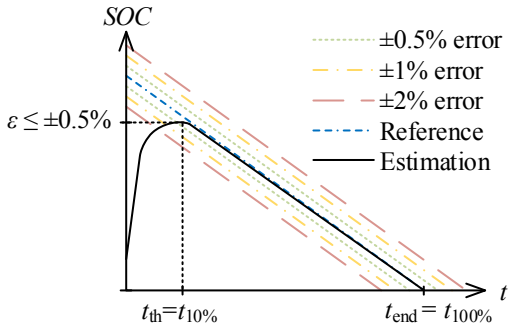

Figure 5.9: Validation principle: evaluation of the transient behaviour (example with profile B, not all boundaries shown).

The resulting point is scaled with the initial error mismatch (Eq. 5.9). So, the maximum points are only reachable when the reference SOC is 100 %, while the initial estimation SOC is 0 % at the beginning. The minimal mismatch must be higher than 8 %, which corresponds to the highest error boundary.

$$K_{\text{trans}} = P(|\varepsilon|) \cdot \frac{|SOC_{\text{ref},t_0} - SOC_{\text{est},t_0}|}{SOC_{\text{ref},t_0}} \tag{5.9}$$

with

$$\varepsilon = SOC_{\text{ref},t_{10\,\%}} - SOC_{\text{est},t_{10\,\%}} \tag{5.10}$$

State estimation algorithms can behave differently during low-dynamic loads, high-dynamic loads or rest periods. To validate the transient behaviour correctly, the test is performed with

a low-dynamic load (profile A), a high dynamic load (profile B) and a rest period (profile A) at the beginning. For the low-dynamic load and the rest period in the beginning, the starting point of profile A is shifted to the first CC discharge period and after the CC charge period, respectively. The mean of these test results is the final evaluation value.

5.4.5 Failure stability K_{fail}

Several errors, such as an offset in the current and voltage measurement as well as incorrect or varying (ageing) parameters, can provoke unstable and inaccurate behaviour in the state estimation algorithm. For reliable functionality, these error cases should be tested and validated. To do so, a current, voltage or parameter offset is set and scores are compared to the normal operation. From the intensity of the score change, the failure stability score $K_{\text{fail},q}$ is calculated. Thereby, q represents the benchmark category. This test uses the results of the estimation, residual charge and drift category.
For evaluating the state estimator in an error case, a current offset ρ_{I} of 0.1 % of the 1 C current and a voltage offset ρ_{U} of 2 % of the voltage range of the cell are used. For the parameter error ρ_{R}, the algorithm is initialised with 10 % of the correct parameter. For a detailed investigation, each error can be considered separately for each category. In the experimental part, for clarity, $K_{\text{fail},q}$ is the mean of all error influences:

$$K_{\text{fail},q} = \frac{1}{3} \sum_{\rho} \left(P(\varepsilon = 0) - |K_q - K_{q,\rho}| \right) \tag{5.11}$$

with

$$\rho \in \{\rho_{\text{I}},\, \rho_{\text{U}},\, \rho_{\text{R}}\}$$

The mean value of $K_{\text{fail},q}$ is the final value for failure stability:

$$\bar{K}_{\text{fail}} = \frac{1}{3} \sum_{q} K_{\text{fail},q} \tag{5.12}$$

with

$$q \in \{\text{est, drift, res}\}$$

5.4.6 Temperature stability K_{temp}

Most algorithms are based on cell models which use temperature-sensitive parameters. In real applications, the cell temperature varies depending on the ambient temperature or due to high loads. Hence, a state estimator has to demonstrate proper functionality at different temperatures. Here, the performance change due to a different temperature in each test is observed.

To achieve an independent score for the overall estimation performance, the standard deviation is used to rate the temperature stability $K_{\text{temp},q}$ (Eq. 5.13). Thereby, q represents the benchmark category. This test uses the results of the estimation, residual charge, drift and transient category.

$$K_{\text{temp},q} = P(\varepsilon = 0) - 2 \cdot \sigma \tag{5.13}$$

with

$$\sigma = \sqrt{\frac{1}{n} \sum_{i=1}^{n} (K_{q,i} - \bar{K}_q)^2} \tag{5.14}$$

where $\bar{K}_q$ is the mean of the scores of profile A or B over the temperature range in each category and n is the number of tested temperatures.

The mean value of $K_{\text{temp},q}$, is the final value for temperature stability:

$$\bar{K}_{\text{temp}} = \frac{1}{4} \sum_{q} K_{\text{temp},q} \tag{5.15}$$

with

$$q \in \{\text{est, drift, res, trans}\}$$

5.4.7 Overview

In Table 5.3 the categories and their test requirements are summarised.

Table 5.3: Benchmark categories and their requirements.

Category	Reference value	Requirements
K_{est}	SOC_{ref}	Profile A, B, and C
K_{drift}	SOC_{ref}	Profile A, B, and C
K_{res}	SOC_{res}	Profile A, B, and C
K_{trans}	SOC_{ref}	Profile A and B with wrong SOC initialisation
K_{fail}	SOC_{ref}	K_{est}, K_{res} and K_{drift} with offsets of profile A, B, and C
K_{temp}	SOC_{ref}	K_{est}, K_{drift}, K_{res}, K_{trans} of profile A and B

5.5 Conclusion

This chapter introduces a generalised validation and benchmark method for SOC estimation algorithms. The method can be used to not only compare different algorithms, but also to optimise a state estimator for specific needs.

The validation consists of three profiles, where low-dynamic, high-dynamic and long-term scenarios are tested. This is repeated for different temperatures in the range from −10 °C to 40 °C. The independence of standardised driving cycles is obtained by developing a synthetic load cycle. To do so, a frequency analysis is performed for 149 different driving cycles and the major time constants are identified.
In the end, a benchmark provides information about the weaknesses and strengths of the studied algorithms and enables a comparison between different algorithms. The benchmark has six categories for the short-term validation and four categories for the long-term test. The categories are: estimation accuracy, transient behaviour, drift behaviour, failure stability, temperature stability, and the estimation accuracy related to the residual charge at the end of each test. These categories and the relationship of some benchmark scores allow the detection of shortcomings of the investigated algorithms.

Part III

Results and Discussion

6 Experimental investigation of lithium-ion cell behaviour

As with many electrochemical systems, batteries exhibit highly non-linear behaviour [166]. The dynamic behaviour depends on the impedance of the cell, which is influenced by many parameters, such as temperature, SOC, current rate, ageing and history [7; 147] (Section 2.1). In a real application, all these dependencies can occur; hence, it is not sufficient to evaluate a state estimator under only one specific condition in the laboratory.
In this chapter, some of the dependencies mentioned in Section 2.1 are presented to emphasise the importance of a detailed evaluation and to guarantee an exact and reliable state estimation with KFs. Firstly in this chapter, the dependencies of a new cell (CG1) and aged cells (CG2) are presented in Section 6.1 and Section 6.2, respectively. Afterwards, the dependencies of the OCV are discussed in Section 6.3. Section 6.4 summarises this chapter by comparing the experimental investigation with the literature research in Section 2.1.

Parts of this chapter were previously published in [167].

6.1 Dependencies of equivalent circuit elements of a new cell

As mentioned in Section 2.1, the ohmic resistance R_i exhibits a low dependency on SOC in comparison to the temperature. Fig. 6.1a shows the resistance R_i at the investigated temperatures $-10\,°\mathrm{C}$, $0\,°\mathrm{C}$, $10\,°\mathrm{C}$, $25\,°\mathrm{C}$ and $40\,°\mathrm{C}$ in the range from $0\,\%$ to $100\,\%$ SOC. The relative difference between the minimum and maximum resistance over the complete SOC range is $6.1\,\%$ or $4\,\%$ at $-10\,°\mathrm{C}$ or $40\,°\mathrm{C}$, respectively. The relative difference between the average resistance at $-10\,°\mathrm{C}$ and $40\,°\mathrm{C}$ is $24\,\%$. Consequently, the temperature has an influence approximately five times higher than that of the SOC.

In addition to R_i, the dependency of the one second resistance $R_{\mathrm{dc1\,s}}$ is shown (Fig. 6.1b). For state and parameter estimation in this work, the resistance one second after a current pulse ($R_{\mathrm{dc1\,s}}$) is used instead of the ohmic resistance R_i, due to the algorithm sample time of one second (τ_s=1 s). Therefore, $R_{\mathrm{dc1\,s}}$ is the resistance calculated one second after a 0.25 C current pulse by relating the voltage drop to the induced current. As a consequence, the $R_{\mathrm{dc1\,s}}$ contains the fast processes of the charge transfer already. Therefore, the $R_{\mathrm{dc1\,s}}$ behaves similarly to the charge transfer resistance. If the $R_{\mathrm{dc1\,s}}$ is used instead of the R_i for parameter fitting, the additional RC terms represent the diffusion effects, which can be modelled more accurately with a higher amount of RC terms.

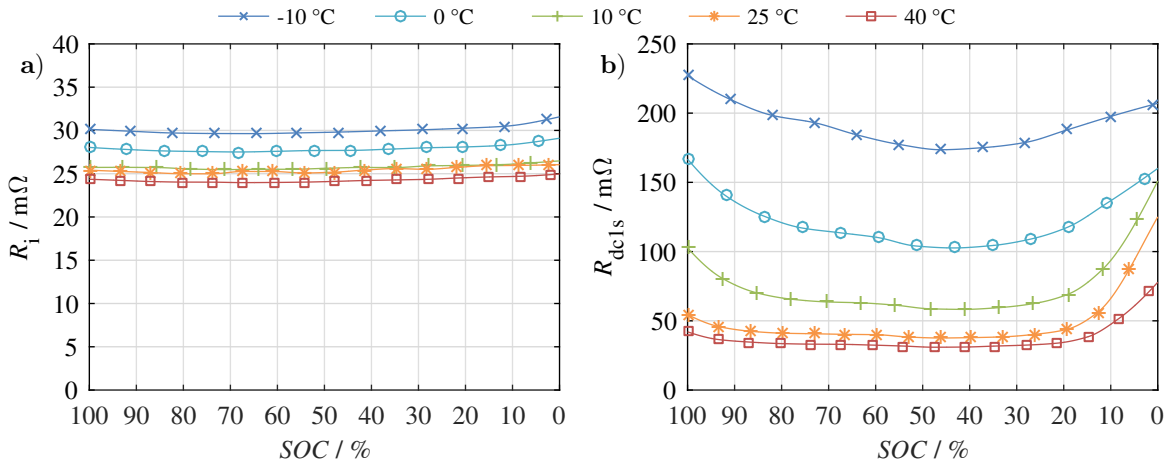

Figure 6.1: Parameters of NCR18650PD: (a) ohmic resistance R_i and (b) $R_{dc1\,s}$ (measured after a $-0.5\,C$ current pulse) at different temperatures. Markers symbolise measurement points.

In this chapter the $R_{dc1\,s}$ is investigated separately. In Fig. 6.1b the temperature and SOC dependency of the $R_{dc1\,s}$, resulting from a $-0.5\,C$ current pulse, is shown. Compared to R_i, a much higher temperature ($\approx$420 %) and SOC ($\approx$70 % at 25 °C) dependency is observable. Similar behaviour can be observed regarding the charge transfer resistance R_1 (two RC term model), which increases with decreasing temperature (not shown).

Fig. 6.2a and Fig. 6.2b show the charge and discharge current rate dependency of the charge transfer resistance R_1 at 0 °C and 40 °C, respectively. It is observed, that the current rate dependency decreases with increasing temperature. Here, the relative difference between the average resistance, measured with a current rate of $-0.25\,C$ and $-1\,C$ results to 26 % and 3 % at a temperature of 0 °C and 40 °C, respectively. This observations agree with the literature research in Section 2.1. A similar behaviour is also observed for R_2.

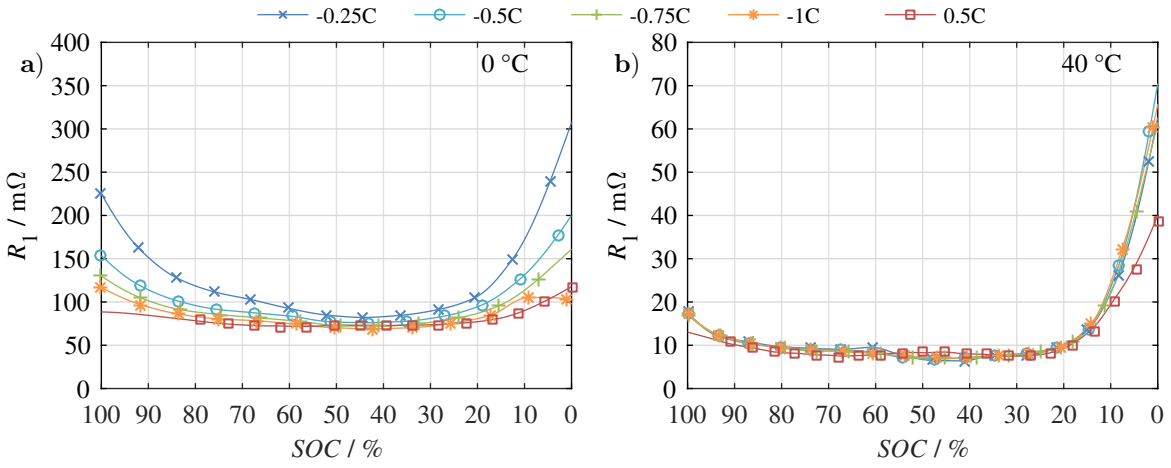

Figure 6.2: Parameters of NCR18650PD: charge transfer resistance R_1 at different current rates at (a) 0 °C and (b) 40 °C. Markers symbolise measurement points.

Due to the relationship $\tau_1 = R_1 \cdot C_1$ and the low temperature and SOC dependency of C_1 [7], τ_1 shows a similar behaviour to R_1 in the investigated temperature range (Fig. 6.3a).

Fig. 6.3b shows the temperature dependency of τ_1 at 10 %, 50 % and 90 %. Interestingly, despite the fact that the relationship between τ_1 and the temperature is linear at a SOC of 10 %, at higher SOCs the behaviour changes to an exponential shape. For τ_2 no clear dependency on SOC and temperature is observable.

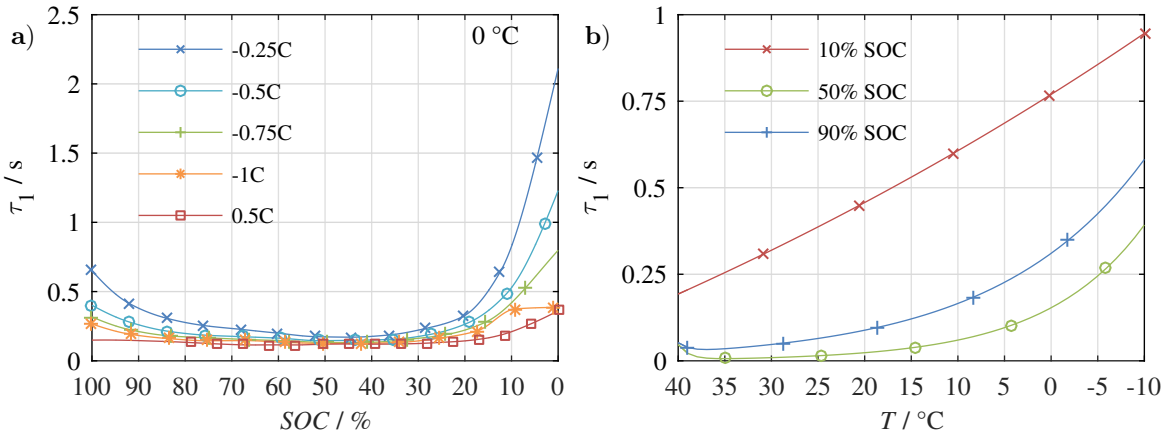

Figure 6.3: Parameters of NCR18650PD: (a) time constant τ_1 at different current rates at 0 °C. Markers symbolise measurement points; (b) interpolated temperature dependency at 10 %, 50 % and 90 % with a current rate of −0.25 C.

Fig. 6.4 shows a qualitative validation of the two RC term ECM including R_i with the presented parameters at 25 °C and 0 °C. Therefore, profile B of the validation method (Chapter 5) is used. In contrast to the simulation results at 0 °C (Fig. 6.4b), the simulated voltage at 25 °C (Fig. 6.4a) almost overlaps the measured voltage. The result at 0 °C shows higher deviations during charging current and relaxation times. This could arise from a low resolution of the current dependency in charge direction, or from differing parameters during relaxation. The latter is not considered in this model.

Below, the difference of the simulated and measured voltage, in the range from 90 % to 10 % SOC, is depicted at 25 °C (Fig. 6.4c) and 0 °C (Fig. 6.4d). The root mean square (RMS) error corresponds to 14.7 mV and 32.9 mV at 25 °C and 0 °C, respectively. Here, an error increase at a SOC lower than approximately 20 % can be observed. This may arise from the increasing non-linearity of the OCV and cell parameters, which is not representable by the RC term ECM. However, for the KF validation in Chapter 7 the ECM uses fixed parameter values at 50 % (initial SOC of profile A and C) or 90 % (initial SOC of profile B), so the accuracy at this SOC level is not relevant. For higher SOCs the model shows an adequate accuracy, hence the model and the parameter fitting are proven to be valid.

6.2 Dependencies of equivalent circuit elements of an aged cell

Now, the dependencies of $R_{\mathrm{dc1\,s}}$ at different ageing states are presented. The investigated cells Z1 (SOH=98.3 %), Z2 (SOH=90.4 %) and Z3 (SOH=82.5 %) are from CG2 (Section 4.7).

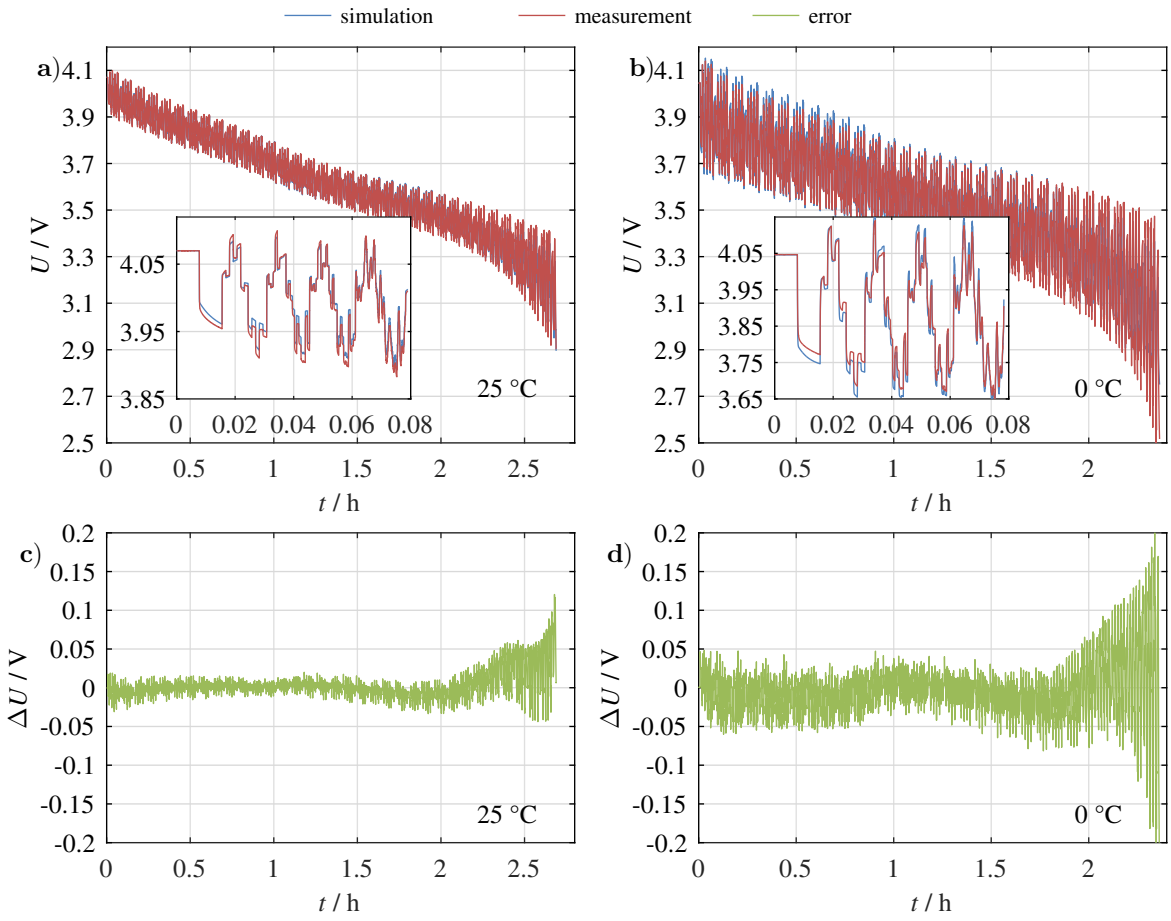

Figure 6.4: Validation of the two RC term ECM and parameters: (a) extract of the total simulation at 25 °C; (b) extract of the total simulation at 0 °C; (c) deviation at 25 °C; (d) deviation at 0 °C

In Fig. 6.5a the $R_{\mathrm{dc1\,s}}$ of the ageing states Z1, Z2 and Z3 depending on the SOC at −10 °C and 40 °C is shown. At −10 °C the resistance of Z1 is depicted over the full SOC range. The resistances of Z2 and Z3 are measurable only in the range from 96 % to 28 % and from 91 % to 35 % SOC, respectively. This can be explained by high impedances caused by ageing and low temperatures, resulting in high overpotentials. The increasing resistance with a decreasing temperature arises from dominant influences of the temperature-dependent conductivity of the electrolyte and charge transfer resistance. As a consequence, the limiting voltage of 4.2 V (U_{max}) and 2.5 V (U_{min}) for the cell is reached before the cell is charged or discharged completely. This problem is reduced at elevated temperatures. Therefore, the SOC range of Z2 and Z3 is increased at a temperature of 40 °C.
Compared to the SOC dependency of $R_{\mathrm{dc1\,s}}$, Fig. 6.5b shows the temperature dependency of the three cells at a SOC of 50 %. The aged cells Z2 and Z3 show a higher variation of the resistance over the investigated temperature range. Similar results are presented in [7; 168].

In Fig. 6.6, the temperature dependency of the actual cell capacity C_{act}, determined by the CCCV discharge (Section 4.5.1), is shown for the three cells. Especially at low temperatures, the usable capacity drops and follows a non-linear characteristic. Due to the previously

mentioned impedance effects, the temperature dependency of the actual cell capacity increases with ageing, despite the low cut-off current. Similar results are presented in [69; 158; 168; 169].

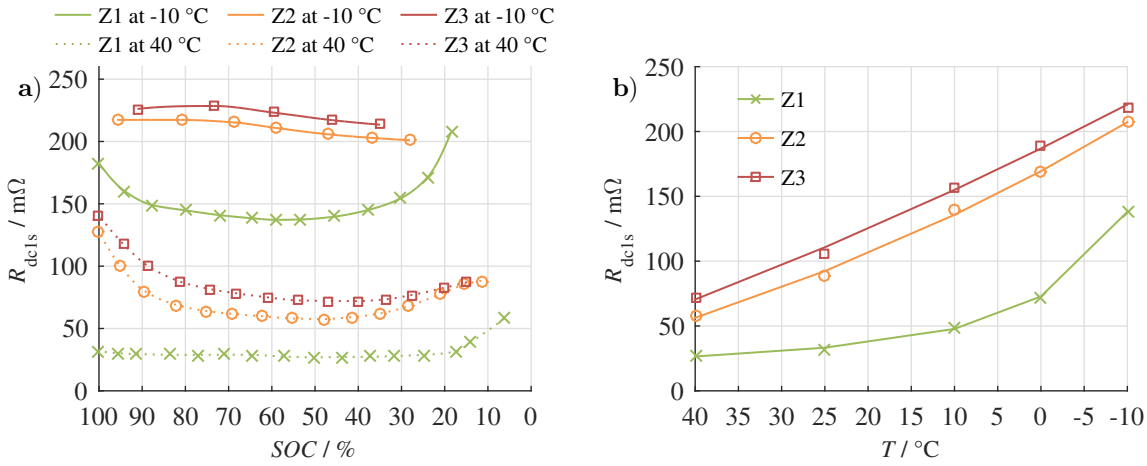

Figure 6.5: Parameters of the investigated cell in three different ageing states: (a) SOC dependency of the $R_{\mathrm{dc1\,s}}$ resistance measured after one second at −10 °C and 40 °C; (b) temperature dependency of $R_{\mathrm{dc1\,s}}$ at a SOC of 50 %. Markers symbolise measurement points.

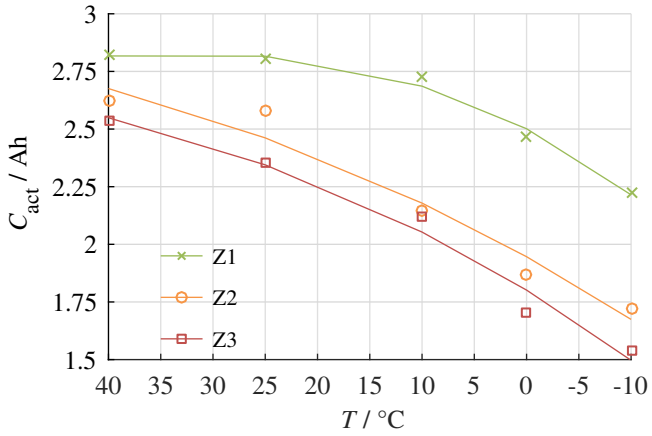

Figure 6.6: Parameters of the investigated cell in three different ageing states: temperature dependency of the actual capacity C_{act} determined by the CCCV discharge (Section 4.5.1). Markers symbolise measurement points.

6.3 Dependencies of the open circuit voltage at different ageing states

The KF and other common OCV-based algorithms use the OCV–SOC relation to estimate the SOC of LICs [4; 80; 121; 170–172]. In these studies, the SOC is derived from the OCV, based on the OCV–SOC correlation [173]. In this work, the OCV is measured by the CC and IC methods according to Section 4.4.2. However, as shown in Fig. 6.7a and Fig. 6.7b as well as in [71; 83; 121], the OCV of a new cell determined by both methods has a non-negligible

temperature dependency. Thereby, ΔSOC is defined as the difference between the OCV-based SOC at 25 °C and the OCV-based SOC at the same voltage at different temperatures. SOC calculations based on the OCV at 25 °C can result, with both methods, in estimation errors up to ΔSOC=4 % at low temperatures ($T \leq 0$ °C). For clarity reasons only the OCV at 25 °C is shown, the deviation is represented by ΔSOC. As one can see, for a new cell the temperature dependency is similar for the OCV determined by the CC method and the IC method. At a SOC higher than 80 %, the IC method shows a lower SOC deviation compared to the CC method.

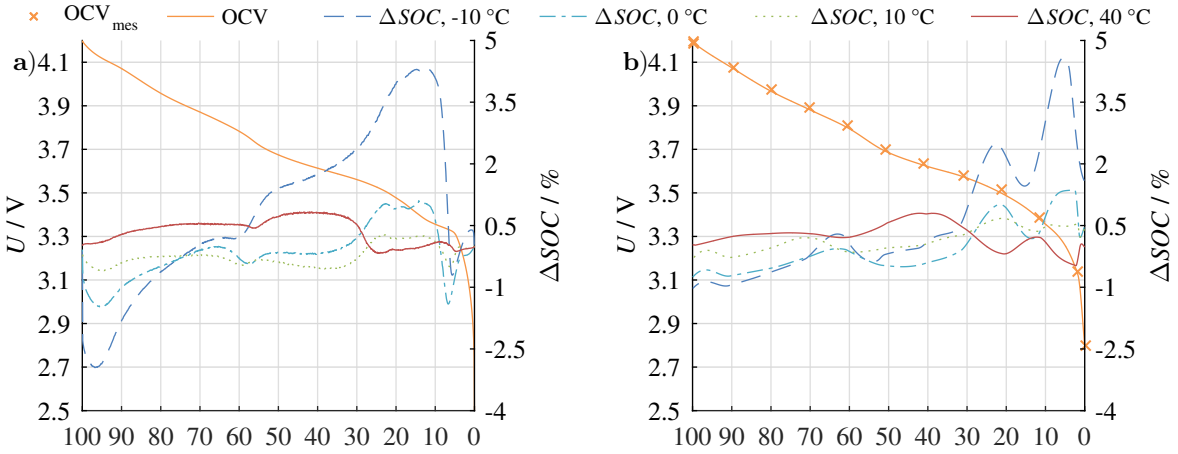

Figure 6.7: Temperature and SOC dependency of a new cell: (a) CC-OCV and (b) IC-OCV (left axis) and temperature influence at the corresponding SOC (right axis).

This behaviour changes with aged cells. In Fig. 6.8a the results of both OCV determination methods are shown in charge and discharge direction for the new (Z1) and old cell (Z3) at 40 °C and −10 °C. The markers of the IC curves correspond to the measurement points. At −10 °C the increasing impedance provokes higher overpotentials. As a consequence, the voltage measured by the CC discharge shows lower values over the entire SOC range compared to higher temperature, whereas the voltage determined by the IC method shows lower values at SOCs higher than 25 %. Below 25 % the voltage level is similar to that at 40 °C.
In charge direction the voltage at −10 °C is higher than at 40 °C for SOC levels lower than 60 %. Above 60 % the voltage measured by the CC method follows the voltage measured at 40 °C, whereas the voltage measured by the IC method shows lower values. At 40 °C both methods show the same values.

Fig. 6.8b shows the interpolated and averaged voltage curves and Fig. 6.9a shows the deviation of the IC method compared to the CC method for Z1 and Z3 at 40 °C and −10 °C, respectively. Despite averaging, it can be observed that especially at low temperatures (−10 °C) and low SOCs (< 40 %) the increasing impedance causes a high voltage drop with the CC method, which results to a $\Delta SOC_{\mathrm{CC-IC}}$ up to 13.5 % (Fig. 6.9a). With the use of the IC method, this voltage drop not exists. As a result, the OCV at −10 °C is at the same voltage level as the OCV of the new cell at 40 °C. At higher SOC levels (> 40 %) both methods show nearly the same values because of the decreasing influence of the impedance.

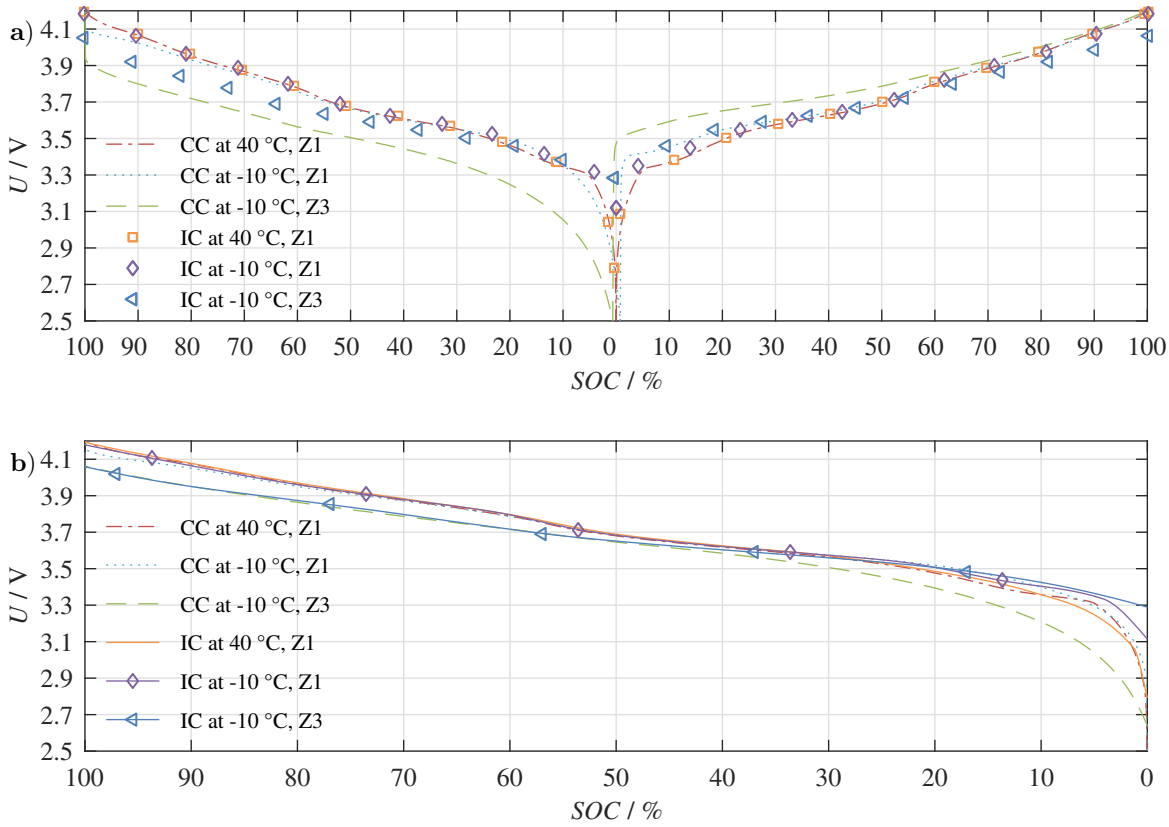

Figure 6.8: OCV determination methods: (a) OCV in charge and discharge direction of the new and old cell at −10 °C and 40 °C measured by the incremental and constant-current method; (b) interpolated and averaged OCVs.

In Fig. 6.8b a lower gradient of the OCV at a temperature of −10 °C can be observed. This can be explained by a decreased maximum and an increased minimum voltage at a SOC of 100 % and 0 %, respectively: after the CCCV charge to 4.2 V with a current of 0.01 C and a cut-off current of 0.005 C the voltage decreases after 3 h relaxation to 4.06 V. This corresponds to a voltage drop of 140 mV compared to U_{max}. At 40 °C this voltage drop is 20 mV. However, due to the low current during the CCCV charge and the low cut-off constraint, the cell is assumed to be at a SOC of 100 %. This voltage relaxation is higher at a SOC of 0 %. Here, the voltage relaxes from U_{min} to approximately 2.77 V ($\Delta U = 270$ mV) for all cells at 40 °C. At −10 °C this voltage drop increases to 614 mV and 789 mV for Z1 and Z3, respectively. As a consequence, the gradient of the OCV is decreased. Fig. 6.9b shows this dependency in the investigated temperature range for the three cells at a SOC of 0 % and 100 %. As one can see, the temperature dependency of the maximum/minimum voltage increases with the age of the cell.

These results show that the CC method is only suitable for new cells at elevated temperatures because of the high overpotentials, due to increased impedances at low temperatures and aged cells. The advantage of this method, compared to the IC method, is the higher resolution of the OCV. In contrast, the IC method allows a precise OCV determination of cells with increased impedance due to ageing or low temperatures.

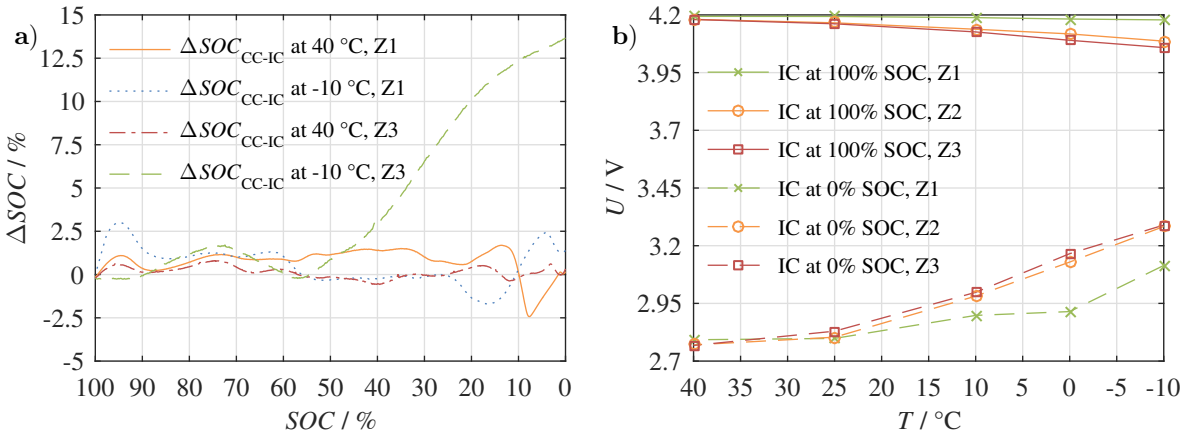

Figure 6.9: OCV determination methods: (a) OCV deviation between the IC method and the CC method of the new and old cell at −10 °C and 40 °C, (b) voltage at 100 % SOC and 0 % SOC at different temperatures and ageing states.

6.4 Conclusion

In this chapter the ECM and OCV dependencies of the investigated cell in the new and aged state is presented. Therefore, the parameters of a two RC term ECM are determined according to Section 4.4 and observed for the new cell at different temperatures (−10 °C, 0 °C, 10 °C, 25 °C and 40 °C) and current rates (−1 C, −0.75 C, −0.5 C, −0.25 C in discharge direction and 0.5 C in charge direction) over the SOC range from 0 % to 100 %. Furthermore, the $R_{\mathrm{dc1\,s}}$, C_{act} and the OCV is investigated at three different ageing states.
Table 6.1 summarises the found dependencies and symbolises the accordance to the literature research in Section 2.1 with a green check tick.

Table 6.1: Comparison of the investigated *SOC*, temperature T, current I and ageing dependencies of the ECM elements with the literature in Section 2.1. The green tick symbolises the accordance to the literature research.

	R_{i}	RC terms	U_0
SOC	[143] ✓	[7; 140; 143; 145; 146; 155] ✓	[83]✓
T	[7; 140; 146; 156] ✓	[7; 122; 140; 143; 145; 146] ✓	[71; 83; 85; 116; 156]✓
I	-	[7; 122; 142; 145–147; 157] ✓	-
Age	[101; 108; 158] ✓	[101; 158]✓	[116–119]✓

The shown dependency of a LIC on SOC, temperature, current and age confirm that a validation of state estimation algorithms is not adequate at only one condition in the laboratory. The next chapter investigates the influence of incorrect ECM parameters on the estimation performance of different KFs.

7 Influence of cell behaviour on the state estimation with different Kalman filters

Using the presented validation method in Chapter 5, the influence of ECM parameters (Chapter 6) of a one and a two RC term ECM on the estimation performance of 9 different KF implementations are investigated in this chapter:

- single Kalman filter (SKF)
- single extended Kalman filter (SEKF)
- single adaptive extended Kalman filter (SAEKF)
- single unscented Kalman filter (SUKF)
- single central difference Kalman filter (SCDKF)
- single square root unscented Kalman filter (SSRUKF)
- single square root central difference Kalman filter (SSRCDKF)
- dual extended Kalman filter (DEKF)
- dual adaptive extended Kalman filter (DAEKF)

Therefore, the cells of CG1 are used.

First, Section 7.1 describes the initialisation for the comparability study and the experimental conditions. Then in Section 7.2, the different SKF are compared regarding their estimation accuracy and behaviour for the battery model with one and two RC terms. The same investigations are performed with the DKF (Section 7.3) and the change in performance compared to the SKF is discussed. In Section 7.4 the dependency of the ECM parameters on the parameter estimation of the dual algorithm is shown. After summarising the benchmark results (Section 7.5), in Section 7.6 the estimation accuracy and transient behaviour of four filters with correctly initialised ECM parameters and individual filter tuning for each temperature are shown, to underline the importance of the correct values.

Parts of this chapter were previously published in [174].

7.1 Initialisation of the Kalman filter

In Section 3.3 the general guidance for the filter tuning is presented. To ensure comparability, all filters use the same fixed set of tuning parameters. The tuning parameters used are summarised in Appendix D Table D.1.
As well as correct filter tuning, the KF requires correct parameter values of the ECM for ac-

curate estimation. As previously mentioned, these parameters are dependent on temperature, SOC and ageing of the cell (Section 2.1 and Chapter 6). However, the exact occurring states of the parameters could be difficult to predict in common applications. Due to the memory limit of embedded systems, as used in BMS, it may not be possible to store several LUTs containing the correct ECM parameters at different temperatures and ageing states. Furthermore, to determine the cell behaviour in all possible conditions an immense measurement effort regarding time and equipment is required. Therefore, in this work the ECM with $R_{\mathrm{dc1\,s}}$ and one RC term, as well as two RC terms are parametrised at a temperature of 25 °C and kept constant for the experiments at other temperatures in order to investigate the temperature influence on the different filters (Appendix D Table D.1). The ECM is initialised at 50 % for profile A and C and at 90 % for profile B to avoid an additional SOC dependent transient behaviour in the beginning. A parameter adapting algorithm should result in a more accurate estimation. However, the OCV and the actual capacity C_{act} are adapted to each temperature, because it is observed that differing values result in unstable behaviour. The initial values for the actual capacity for each temperature are shown in Appendix D Table D.2. The initial SOC for the reference and the algorithms are derived from the OCV–SOC relation.

7.2 State estimation: single Kalman filter

Fig. 7.1 shows the results for the single unscented Kalman filter (SUKF), the single linear Kalman filter (SLKF), the single extended Kalman filter (SEKF) and the single adaptive extended Kalman filter (SAEKF).

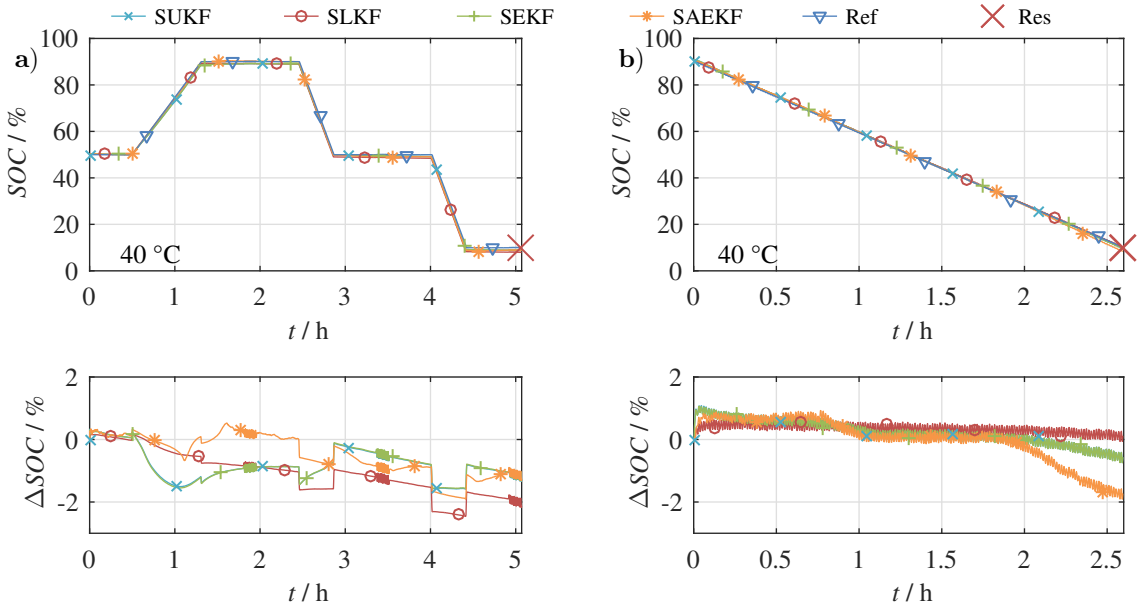

Figure 7.1: SOC estimation results and the deviation from the reference (ΔSOC) of the SKF (one RC term) with correct initialisation: (a) profile A at 40 °C; (b) profile B at 40 °C.

All results are compared to the reference (Ref) and to the SOC based on the residual charge (Res). In Fig. 7.1a and Fig. 7.1b the estimation result and the deviation from the reference (ΔSOC) of profile A and profile B are shown at 40 °C, respectively. Here, the algorithms show nearly identical behaviour and are in agreement with the reference. The differences between the filters are lower than 1 %, except at a lower SOC level in profile B. The RMS error between the reference and the estimation is smaller than 1.3 % and 0.7 % for profile A and profile B, respectively. The SOC based on the residual charge is predicted with an error smaller than 2 % for profile A and profile B. The differences of the ECM parameters between 25 °C and temperatures below 10 °C are higher than between 25 °C and 40 °C. As a result the estimation accuracy is reduced at lower temperatures.

For profile A, at 0 °C, a gradient different for each filter is visible during the first CC charge period (Fig. 7.2a). This provokes a SOC overestimation of up to 5.52 percentage points. While the SLKF stays constant after the charging period, the SUKF and SEKF correct the over estimated SOC during the pause and SLC. However, the SAEKF follows the reference in each time step. After the first CC discharge period at approximately 50 % SOC, the estimation difference between the filters is lower than 1.5 %. This deviation increases to 3 % at 10 % SOC.

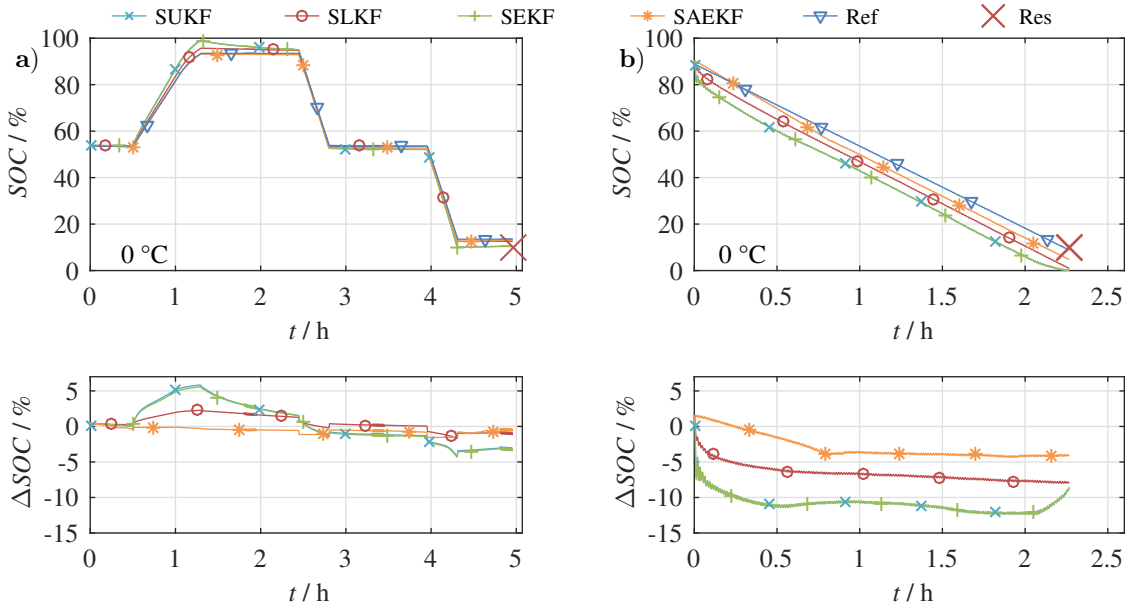

Figure 7.2: SOC estimation results and the deviation from the reference (ΔSOC) of the SKF (one RC term) with correct initialisation: (a) profile A at 0 °C; (b) profile B at 0 °C.

While the SLKF and the SAEKF are closer to the reference ($\Delta SOC = 1\,\%$), the SEKF and SUKF are closer to the residual charge ($\Delta SOC = 0.5\,\%$). The increased estimation errors at higher (≈90 %) and lower (≈10 %) SOC levels correlates to the higher ECM parameter deviation from the parameters at 25 °C at these points (Fig. 6.1 to Fig. 6.2). The deviation between the reference and the SOC based on the residual charge may arise from temperature effects during the CC charge and discharge periods. As the temperature decreases, measurable self-heating of the cell increases, due to the increasing resistances (higher resistances at lower SOC, Section 2.1). Therefore, only the CC periods provoke an observable increase in

temperature on the cell surface. For the used cell, the measured surface temperature increases by 7 K during profile A performed at 0 °C at lower SOC levels. This effect is negligible during profile B, here the temperature increases by 2 K.
For profile B, at 0 °C (Fig. 7.2b), all filters show a parallel offset towards a lower SOC level after 0.5 h, resulting in a difference between the filters smaller than 4.7 % in the end. At this point, the error of all filters is smaller than 9 %. During the estimation the error is lower than 13 %. Due to the high-dynamic current load, deviating parameters caused by the temperature, have a high influence on the estimation. During pauses and CC charge and discharge periods, the RC term is in steady state after a transient behaviour. During a high-dynamic current load, the RC term determines the voltage dynamic and hence the estimation accuracy. The voltage difference caused by the deviating ECM parameters at 0 °C can be seen in Fig. 7.3. This shows the importance of correct ECM parameter at every temperature. A parameter mismatch leads to a higher estimation error.

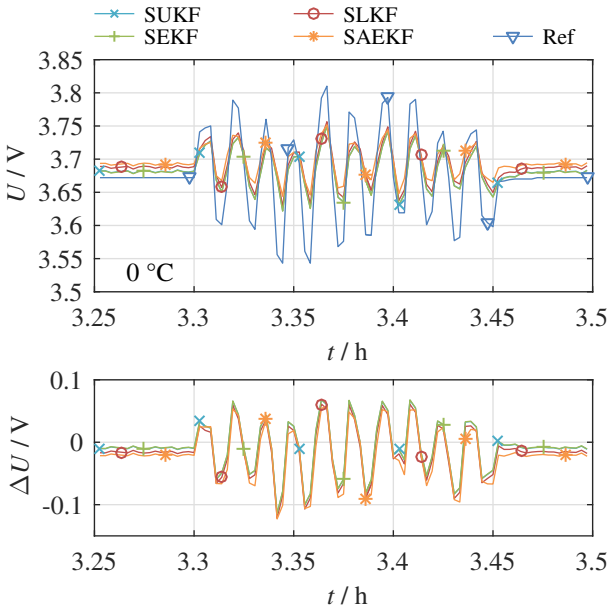

Figure 7.3: Voltage estimation results U and voltage error ΔU of the SKF (one RC term) with correct initialisation: estimated and measured voltage of profile A (during a SLC at approximately 50 % SOC) at 0 °C.

In Fig. 7.4 the long-term behaviour of the algorithms is shown. Here, also the Coulomb counter of the BMS is depicted (SOC BMS). This Coulomb counter receives the same current input as the algorithm. For profile A and B, the Coulomb counter shows almost the same results as the reference, due to the short duration of the test (Fig. 7.1 and Fig. 7.2). During the long-term test, the reference and the BMS show a decreasing behaviour despite the Coulomb neutral SLC. This is due to accumulating measurement errors and the limited sample rate. On the contrary, the estimated SOC values increase. While the SOC based on the residual charge at the end of both short profiles A and B is identical with the last value of the reference, SOC_{res} differs from the reference in profile C ($\Delta SOC = 1.7\,\%$). The reference drifts apart, due to the change in cell capacity caused by temperature variation and accumulated errors in the

current measurement. All algorithms show the same behaviour and the mean error between the KF and the residual charge based SOC is 0.2 %. Here, the reference deviates by 1.3 %.

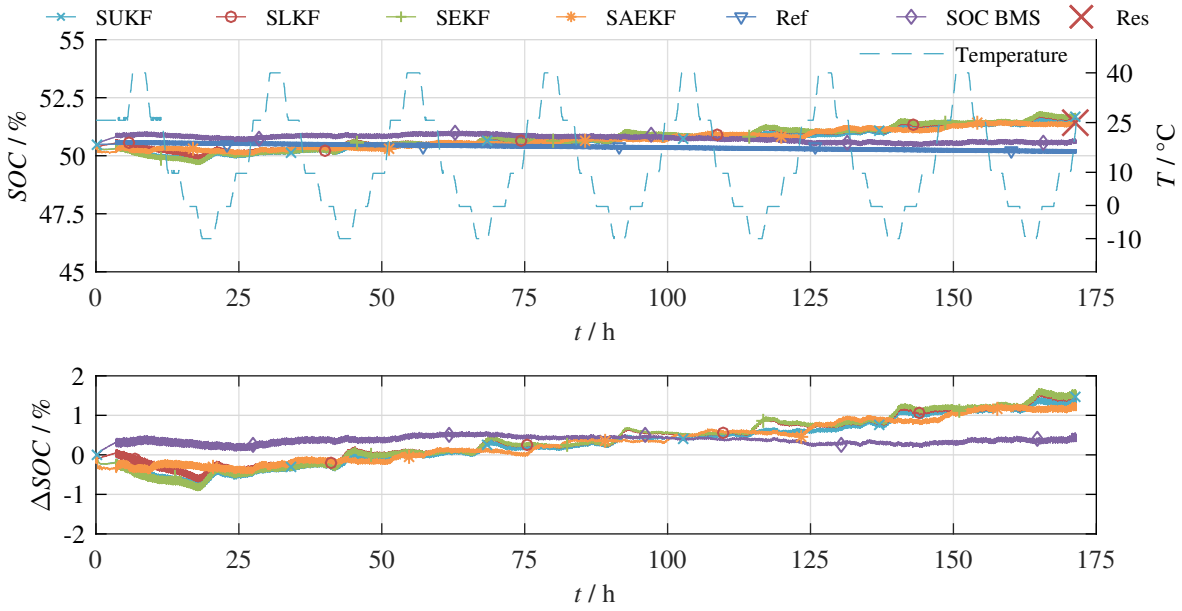

Figure 7.4: SOC estimation results and the deviation from the reference (ΔSOC) of the SKF (one RC term) with correct initialisation: profile C.

The results for the single square root unscented Kalman filter (SSRUKF), the single central difference Kalman filter (SCDKF) and the single square root central difference Kalman filter (SSRCDKF) are not shown, since the difference of the estimation results compared to the SUKF is negligible [67, p. 81]. Table 7.1 summarises the RMS error during profile B at 25 °C of these filters compared with the error of the SUKF. Due to the similar estimation behaviour only the results for the SUKF are shown for clarity reasons.

Table 7.1: RMS error of the sigma point and square root KF for profile B at 25 °C

	SUKF	SSRUKF	SCDKF	SSRCDKF
RMS error	0.8029 %	0.8029 %	0.8049 %	0.8049 %

The numerical advantage of the square root forms is negligible on computing environments like Matlab. However, the advantage could be higher on embedded systems with limited word lengths. Due to the square root of the covariance matrices a larger range is representable with the available word length. As a result, rounding errors are reduced and the numerical stability is increased [67, p. 111].

The validation method from Chapter 5 includes an investigation into the estimation behaviour after wrong initialisation values and current, voltage or parameter offsets.
Fig. 7.5a depicts the results of the SOC estimation within the first 10 % of time for an incorrect initial value of the high-dynamic profile B at 25 °C. In this case, the correct SOC is 90 %, but the filter is initialised with a SOC value of 10 %. With the exception of the SLKF, all algorithms are able to correct the wrong initial value. After an initial correction of the error,

the estimation of the SLKF results in a parallel offset of 10 % SOC. The SEKF and the SUKF correct the error within the first calculation step. Due to the fast transient behaviour, an overshoot of the estimation can be observed in the error plot. Compared to these algorithms, the SOC estimation of the SAEKF increases slowly until the correct value is reached after 0.21 h. Due to the measurement noise adaptation (Eq. 3.18), the Kalman gain increases slower in the beginning compared to the other algorithms. This results in a delayed SOC correction. To avoid this behaviour, the covariance matrix can be adjusted. The remaining offset between the estimation and the reference is caused by inaccurate ECM parameters.

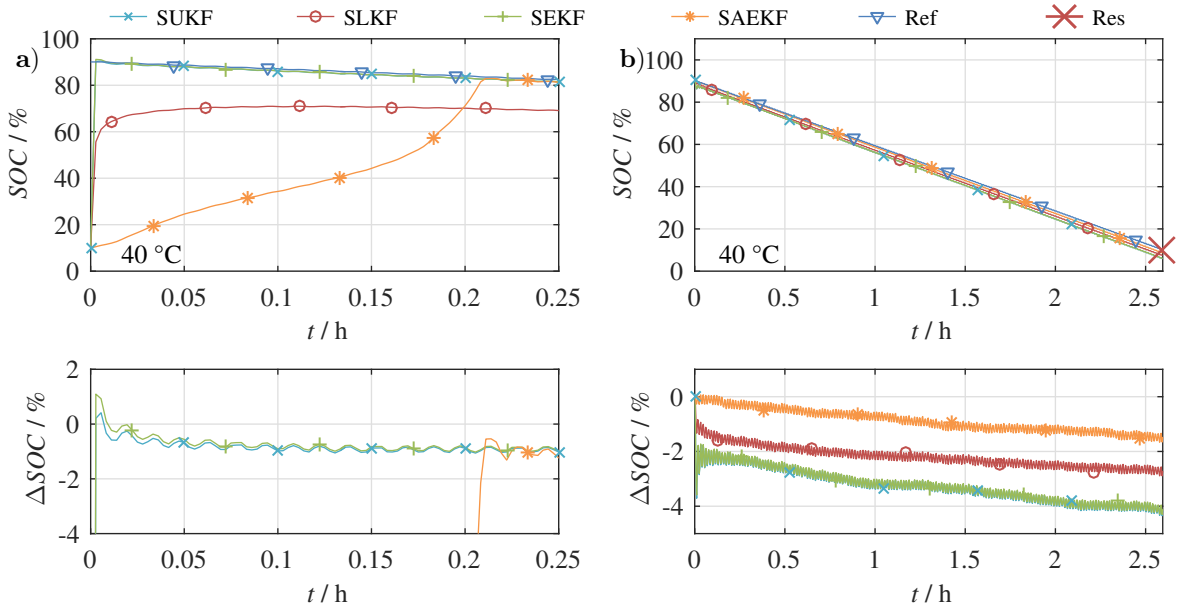

Figure 7.5: SOC estimation results and the deviation from the reference (ΔSOC) of the SKF (one RC term): (a) transient behaviour during high-dynamic discharge (first 10 % of time of profile B at 25 °C); (b) influence of an incorrect parameter ($R_{\mathrm{dc1\,s}}$, profile B at 40 °C).

In Fig. 7.5b the result of the SOC estimation with a parameter offset of $R_{\mathrm{dc1\,s}}$ is shown ($R_{\mathrm{dc1\,s}}$ is initialised with 10 % of the correct parameter value, for the used cell the initial value of $R_{\mathrm{dc1\,s}}$ results to 4.27 mΩ). Therefore, the resistance error generates a smaller voltage drop. As a consequence, the voltage in the ECM is modified and operates as a modification of the OCV. Due to the prediction part of the KF based on the Coulomb counter, the SOC error based on the residual charge is only increased by 3.55 percentage points for the SEKF. Similar errors in the ECM parametrisation can be provoked by a resistance increase due to ageing effects. A dual KF, which can also adapt the parameters of an ECM, would be able to correct the incorrect parameters and thus the influence of this error could be minimised [5; 30].

When the current measurement is afflicted with a current offset, the algorithm has to correct the resulting deviation from the Coulomb counter. In Fig. 7.6 the influence of a 0.001 C current offset (2.85 mA) on profile C is presented and the Coulomb counter based on the measurement data of the BMS is shown (SOC BMS). Since the KF uses not only the BMS Coulomb counter, but also the measured voltage, the algorithms can compensate the drift in parts. Compared to the estimation without current offset (Fig. 7.4), the error regarding the

SOC based on the residual charge is 1.4 percentage points higher. The SOC from the current offset afflicted Coulomb counter of the BMS results in an error of 16 %. Whereas the SLKF, SEKF and SUKF show nearly identical linear behaviour, the SAEKF oscillates with the same gradient as the other algorithms. The oscillation arises from the changing capacity due to the varying temperature. The adaptive tuning of the SAEKF causes a more sensitive behaviour to the temperature dependency, which results in a higher oscillation amplitude. The benchmark method presented in Chapter 5 allows a more detailed analysis of the estimation performance.

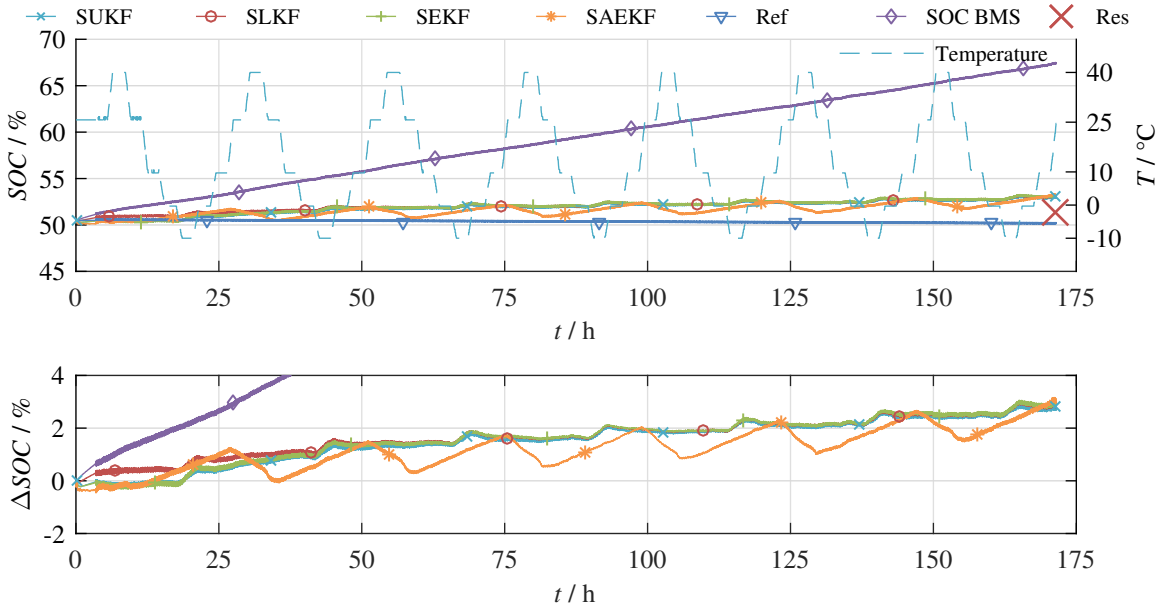

Figure 7.6: SOC estimation results and the deviation from the reference (ΔSOC) of the SKF (one RC term): influence of a current offset on profile C.

In Fig. 7.7 the four KF with one and two RC terms are compared at −10 °C, 0 °C, 10 °C, 25 °C and 40 °C. Thereby, Fig. 7.7a shows the estimation benchmark results K_{est} during profile A. As the ECM is initialised at 25 °C, here, the highest score is achieved compared to the results at other temperatures. With higher and lower temperatures the accuracy decreases, due to deviating ECM parameters. The score differences between the algorithms change with temperature. Compared to the other algorithms, the SAEKF shows a lower score at 25 °C, but at other temperatures the results are better than for the SUKF and SEKF. Therefore, the SUKF and SEKF show nearly identical behaviour. The SLKF behaviour is similar to that of the SEKF and SUKF, except at 0 °C and 10 °C. Here, the SLKF achieves approximately one score more. At 0 °C the SLKF and the SAEKF show nearly identical behaviour. Due to the steady state during CC charge or discharge periods, the number of RC terms do not influence the voltage estimation of the KF. Hence, the differences between the estimations with one or two RC terms are negligible.

Fig. 7.7b shows the accuracy distribution over the investigated temperature range, if the ECM is initialised at 10 °C instead of at 25 °C. As a consequence, the performance peak of the one RC term filters is shifted to 10 °C. At this temperature the accuracy of the two RC term ECM decreases. Changing the initialisation temperature does not affect the results of the SAEKF.

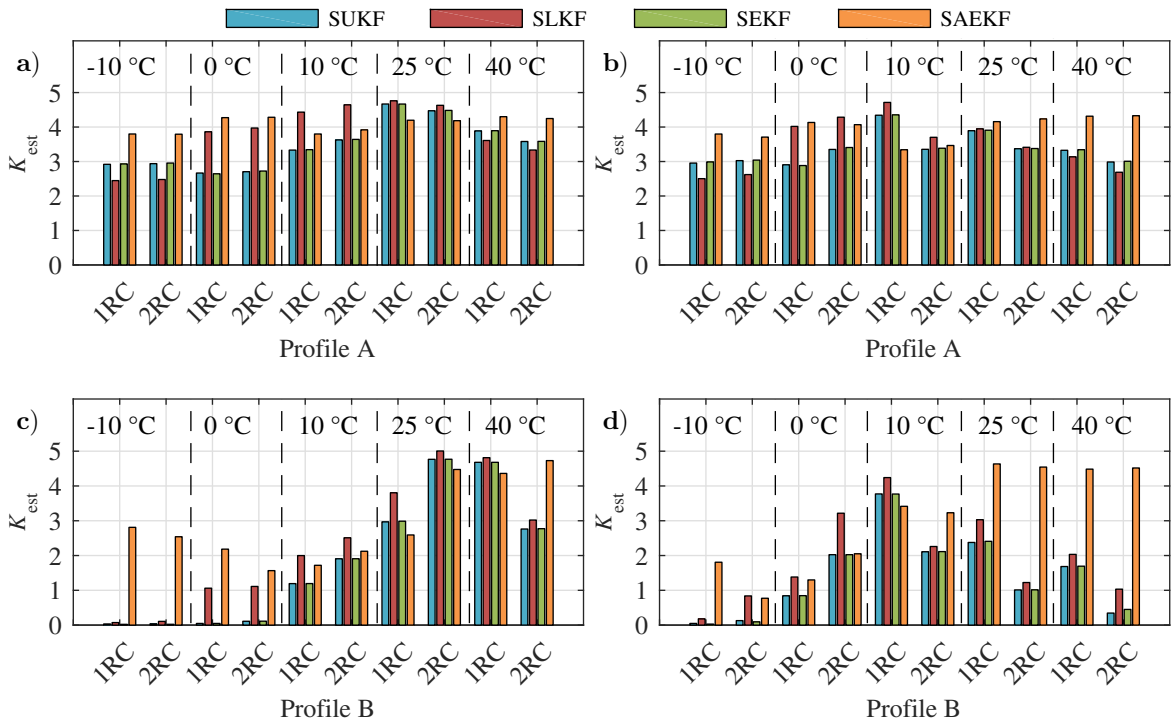

Figure 7.7: Estimation score K_{est} of the SKFs with one and two RC terms at different temperatures: (a) during low-dynamic load (profile A) with the ECM initialised at 25 °C; (b) during low-dynamic load (profile A) with the ECM initialised at 10 °C; (c) during high-dynamic load (profile B) with the ECM initialised at 25 °C; (d) during high-dynamic load (profile B) with the ECM initialised at 10 °C.

The behaviour during the high-dynamic profile B is shown in Fig. 7.7c. Here, a higher impact of low temperatures to the estimation accuracy is observable. Moreover, the differences between one RC and two RC terms are higher. This effect is already described previously. Furthermore, it is observable, that the two RC term model results in a higher estimation accuracy (except at 40 °C) due to the increased voltage estimation accuracy. Similarly to profile A, the score decreases with temperatures different from 25 °C, although the SAEKF shows an advantage against the other algorithms at low temperatures. The noise adaptation of the SAEKF reduces the process noise for the SOC resulting in a higher weighting of the Coulomb counter. The SEKF and SUKF show an identical behaviour.
Parametrising the ECM at 10 °C instead of 25 °C results in a higher estimation accuracy at 10 °C (Fig. 7.7d). However, the estimation accuracy at temperatures differing from 10 °C is lower. This behaviour is comparable to the ECM parametrised at 25 °C (Fig. 7.7c). Here, the SAEKF shows the best performance over the temperature range investigated in this work.

As shown in Fig. 7.7c, the same temperature dependency is observable in Fig. 7.8a, where the results of the transient test with profile B at different temperatures are shown. The SLKF is not able to correct the wrong initial value at any temperature. The other algorithms are not able to correct the error at −10 °C. With the exception at 40 °C, the SAEKF shows a lower score compared to the SEKF and SUKF (compare with Fig. 7.5a).
For the long-term profile C, with varying temperature, four benchmark criteria are considered.

The score for K_{est}, K_{drift}, K_{fail} and K_{res} are shown in Fig. 7.8b. In contrast to the high-dynamic profile B, the RC term dependency is not visible. At a SOC of 50 % the parameter difference between the one and two RC term ECM in the range of −10 °C and 40 °C is small compared with lower and higher SOC levels. Due to the constant SOC of 50 %, the parameters change only in dependency of the temperature.

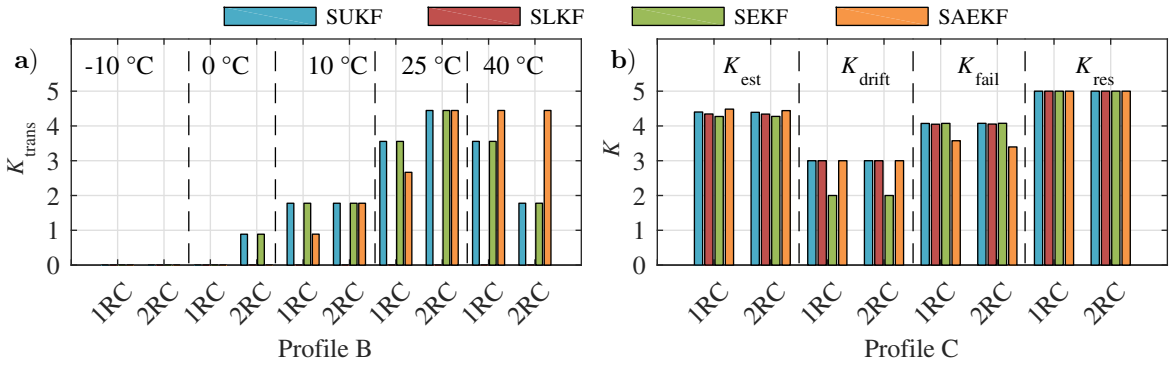

Figure 7.8: Benchmark results of the SKF with one and two RC terms (ECM initialised at 25 °C): (a) transient behaviour K_{trans} during high-dynamic discharge (profile B) at different temperatures; (b) estimation score K_{est}, drift score K_{drift}, failure stability score K_{fail} and residual charge determination score K_{res} during the long-term test (profile C) with varying temperature.

7.3 State estimation: dual Kalman filter

A DKF allows a correction of incorrect or changing ECM parameters resulting in a more accurate estimation. In Fig. 7.9 and Fig. 7.10 the behaviour of the dual extended Kalman filter (DEKF) and the dual adaptive extended Kalman filter (DAEKF) is shown.

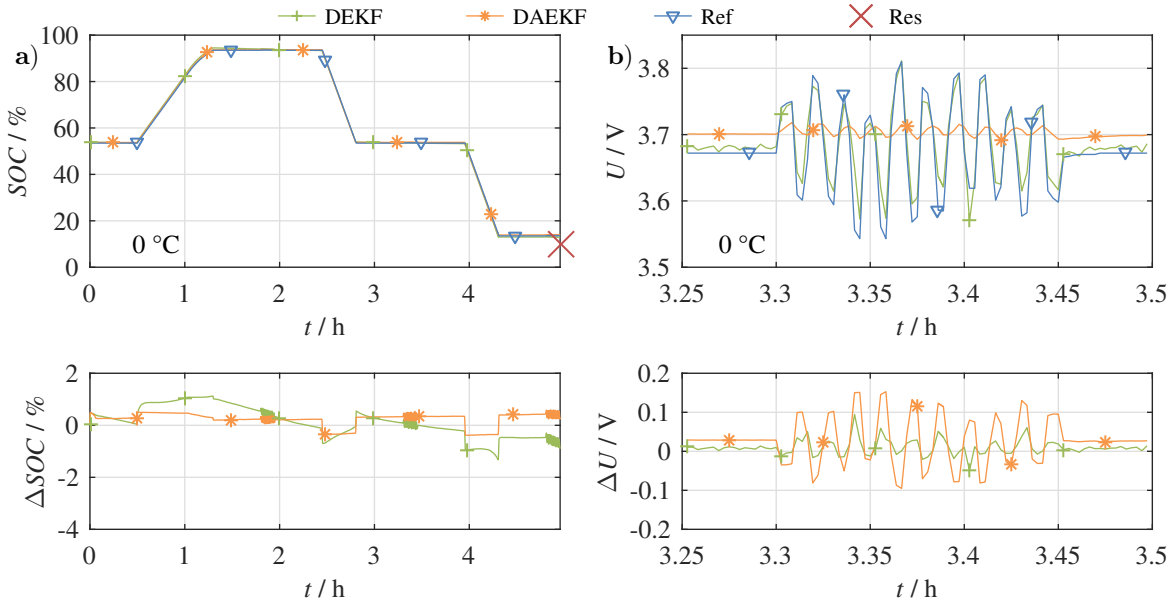

Figure 7.9: Results of the DKF (one RC term) and the deviation from the reference (ΔSOC): (a) profile A at 0 °C; (b) voltage error of profile A (during a SLC at approximately 50 % SOC) at 0 °C.

Therein, Fig. 7.9a shows the estimation during profile A at 0 °C. Compared to the corresponding SKF in Fig. 7.2a, the estimation of both algorithms follows the reference value in the investigated time period. In addition, the SOC overshoot of the SEKF and SUKF is reduced from 5.52 to 1.06 percentage points.
In Fig. 7.9b the voltage estimation of the DKF during the SLC in profile A at 0 °C is shown. Compared to the SEKF (Fig. 7.3), the voltage estimation is improved by the DEKF by 63.5 percentage points, related to the RMS error. Despite the adaptation of the measurement noise and process noise matrix, the DAEKF shows a lower voltage estimation performance than the DEKF.

Fig. 7.10 shows the influence of a dual estimation when an ECM parameter is not correct. Compared to the estimation without parameter offset, the error of the SEKF increased by 3.55 percentage points (Fig. 7.5b), whereas the error of the DEKF increased by 2.28 percentage points. In this case, the DAEKF shows no improvement in the estimation behaviour.

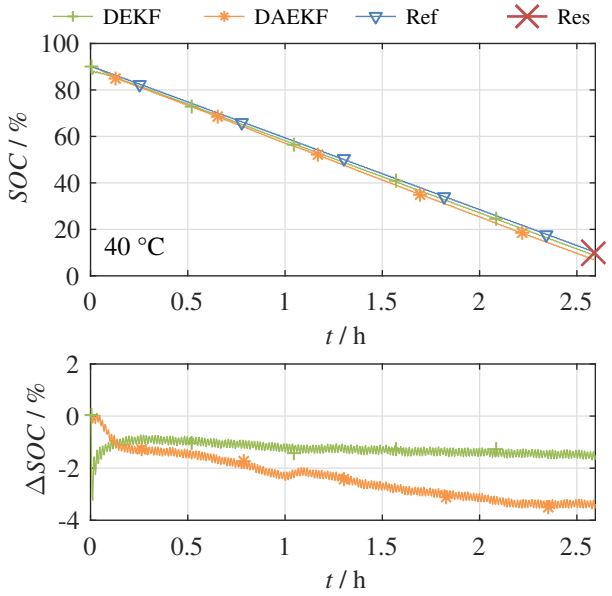

Figure 7.10: Results of the DKF (one RC term) and the deviation from the reference (ΔSOC): influence of an incorrect parameter ($R_{\mathrm{dc1\,s}}$, profile B at 25 °C).

In Fig. 7.11 the performance difference of the dual estimation and the SKF is shown. Here, a positive value indicates an improvement of the DKF against the SKF. During low-dynamic loads (Fig. 7.11a) the estimation of the DEKF is improved at every temperature. The DAEKF decreases the accuracy at 40 °C.
In contrast to the increase in accuracy during low-dynamic loads, a decrease in accuracy is observed during high-dynamic loads (Fig. 7.11b). Therefore, a decrease in the estimation accuracy score is observable for both dual algorithms at 25 °C and 40 °C. During a high-dynamic load, the parameter estimation is enhanced. Depending on the filter tuning, this could lead to a faster adaptation of the parameter compared to the SOC, which could lead to the increased SOC estimation errors. In addition, the transient behaviour shows a score between one or two

points lower at these temperatures for the DEKF or the DAEKF, respectively (Fig. 7.11c). Depending on the temperature or the algorithm, this behaviour can be caused by a too rapid ECM parameter adaptation of the filter. Therefore, the error between the measured and calculated voltage is not reduced by the correction of the SOC, but by a change of an ECM parameter, which results in a decreased voltage error due to the changed voltage drop. This can be influenced by the filter tuning.

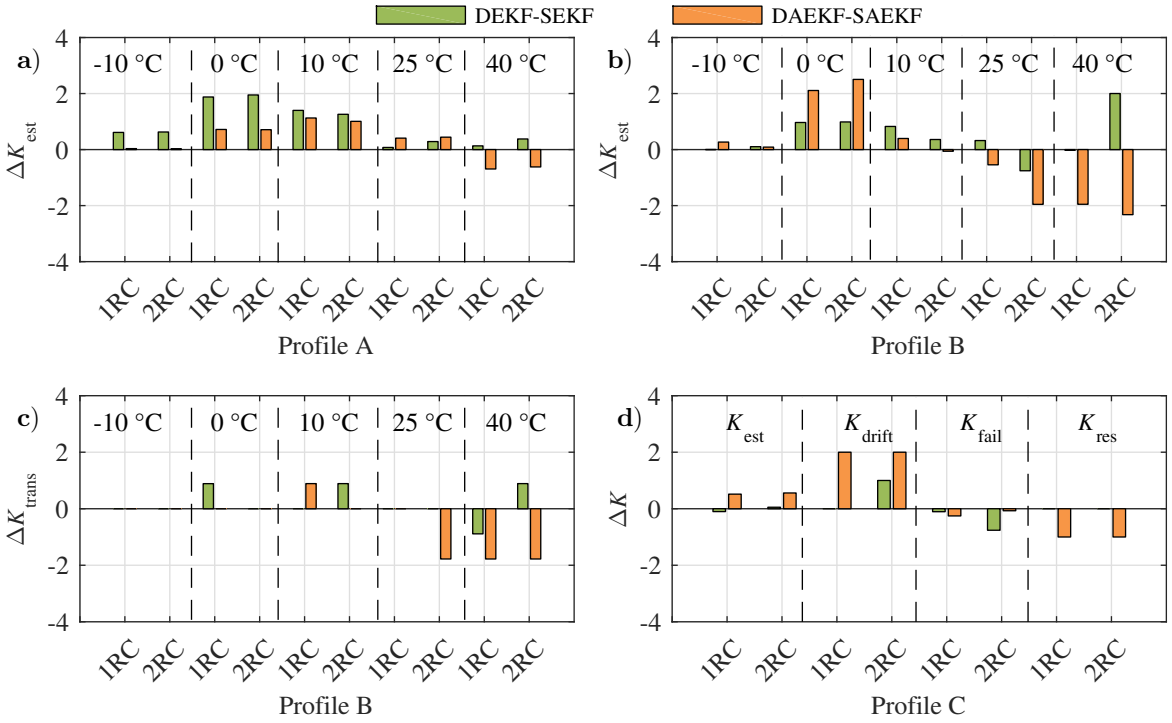

Figure 7.11: Performance change of a DKF compared to the corresponding single KF: (a) estimation score ΔK_{est} at different temperatures during low-dynamic load (profile A); (b) ΔK_{est} at different temperatures during high-dynamic load (profile B); (c) transient behaviour during high-dynamic discharge (profile B) at different temperatures ΔK_{trans}; (d) ΔK_{est}, drift score ΔK_{drift}, failure stability score ΔK_{fail} and residual charge determination score ΔK_{res} during the long-term test (profile C) with varying temperature.

During the long-term test (profile C) the dual estimation improves the estimation score K_{est} and the drift behaviour K_{drift} of the adaptive KF for both ECM models. In addition, the failure stability K_{fail} and the SOC estimation score based on the residual charge K_{res} is reduced. The influence of the DEKF on the estimation behaviour is only observable in the K_{drift} and K_{fail} category with two RC terms. Thereby, the overall drift behaviour is increased and the failure stability is decreased.

7.4 Parameter estimation: dual Kalman filter

Due to the initialisation of the parameters at 25 °C, the estimation accuracy tends to decrease at lower temperatures. This behaviour correlates with the decreasing precision of the ECM parameters. The improved estimation at different temperatures is achieved by a correction of the SOC and temperature dependent ECM parameters. To evaluate this behaviour, the correction of the parameter $R_{\mathrm{dc1\,s}}$ over the SOC range for a KF with one and two RC term ECM is depicted in Fig. 7.12. Thereby, the reference parameter is the result of the parameter determination over the entire SOC range according to Section 4.4.

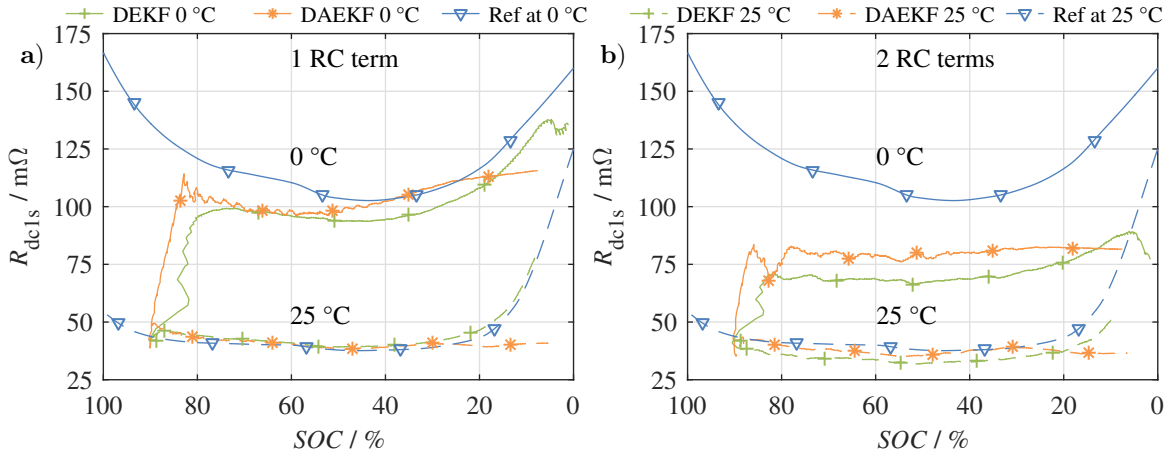

Figure 7.12: Comparison of the $R_{\mathrm{dc1\,s}}$ estimation by the DKF with one (a) and two (b) RC terms at 0 °C and 25 °C (Profile B).

The $R_{\mathrm{dc1\,s}}$ estimated by the DEKF and DAEKF with one RC term during profile B at 0 °C and 25 °C is shown in Fig. 7.12a. Here, the ECM parameters are initialised at 25 °C. Hence, the estimation at 25 °C follows the reference parameter without a transient behaviour in the beginning of the profile (SOC=90 %). At a SOC<20 %, $R_{\mathrm{dc1\,s}}$ starts to increase due to electrochemical effects in the cell (Section 2.1). The DEKF can adapt to this effect by increasing $R_{\mathrm{dc1\,s}}$. Compared to the DEKF, the DAEKF is not able to correct the parameter increase. At 0 °C a correction of the parameter estimation at the beginning of the profile is visible. At a SOC<80 % the estimation follows the reference value. Similar to the estimation at 25 °C, the parameter estimated by the DEKF increases with decreasing SOC while the estimation by the DAEKF stays approximately constant.

Fig. 7.12b shows the $R_{\mathrm{dc1\,s}}$ estimation by the DKF with two RC terms. The result of the two RC term algorithms at 25 °C shows a similar behaviour as with one RC term, but the deviation to the reference is higher. The initial correction of the DKFs with two RC terms at 0 °C is lower compared with the one RC term algorithms. In this case, the correction of the voltage error is performed by adjusting the additional RC term. In consequence, the resistance of the $R_{\mathrm{dc1\,s}}$ is shifted to the second RC term. It can be concluded, that the parameter estimation with the less complex ECM results in an increased estimation accuracy. This arises from the lower amount of ECM parameters and results in simpler filter tuning.

7.5 Benchmark: summary and comparison

The results of the investigated algorithms are summarised for the three profiles in Fig. 7.13. It is notable that it is not possible to identify the best algorithm for all operation conditions, thus, the selection should be based on the specific application. However, it can be seen, that the dual estimation (DEKF or DAEKF) shows an advantage in all categories, except K_{res} during profile A.

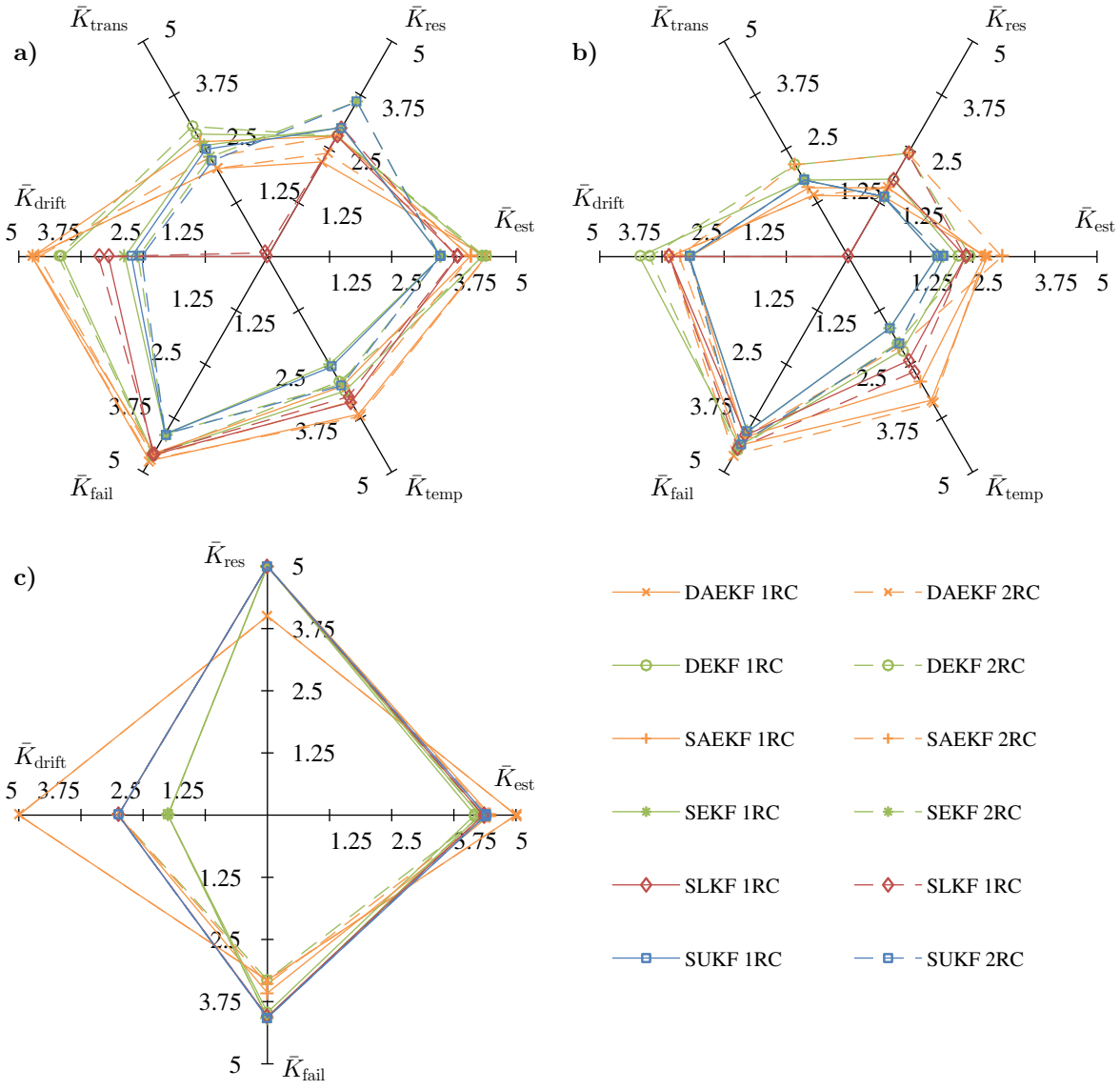

Figure 7.13: Net diagram with the final scores of all investigated KFs: (a) low-dynamic load (profile A); (b) high-dynamic load (profile B); (c) long-term test (profile C).

7.6 Individual filter tuning and correct equivalent circuit model parameters

In Fig. 7.7, Fig. 7.8 and Fig. 7.11 the strong dependency of the temperature on the estimation behaviour is shown. This is based on the fact that the dynamic of the cell changes due to the temperature dependency of the electrochemical effects, resulting in a change of the ECM parameters (Section 2.1) and consequently in a change of model uncertainties. Hence, the constant filter tuning is not optimal.
In this section the validation of the SEKF, SAEKF and DEKF with one RC term and the SLKF with two RC terms is repeated for profile B at 0 °C and 25 °C. Thereby, the ECM parameters are initialised with the correct parameters for both temperatures. The parameters at 0 °C are summarised in Appendix D Table D.3. Furthermore, the KFs are tuned individually for both temperatures. The tuning parameters are again determined experimentally (Section 3.3). In Appendix D Table D.4 the changed parameters for 0 °C and 25 °C are shown.
The results of the estimation score K_{est} and the transient behaviour K_{trans} are shown in Fig. 7.14. Compared with the non-individually tuned filters, the estimation accuracy is increased (Fig. 7.14a). The SEKF and the SAEKF show a higher estimation accuracy score at 0 °C compared with at 25 °C. The DEKF achieved approximately the same score for both temperatures.
The transient behaviour is shown in Fig. 7.14b. The SOC correction failed for the SLKF and the SAEKF at 0 °C with the non-individual filter tuning (Fig. 7.8a). With the individually tuned filters, the selected KFs achieve approximately the same score for both temperatures. The tuning of the algorithms with two RC terms is more challenging due to the additional tuning parameters. Here, a higher K_{est} for the SLKF with two RC terms resulted in a lower K_{trans}.

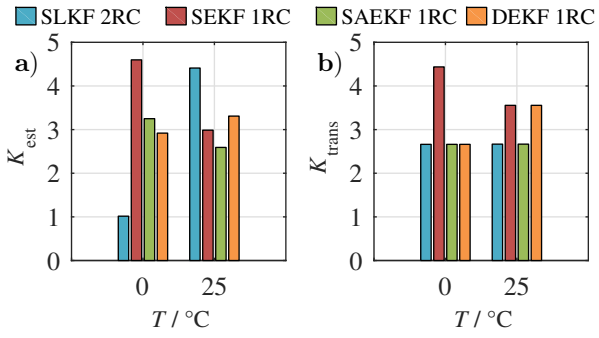

Figure 7.14: Benchmark results with correct parameters and individual filter tuning at 0 °C and 25 °C during profile B: (a) estimation score K_{est}; (b) transient behaviour K_{trans}.

As one can see, all filters can achieve an adequate accuracy with correct ECM parameters and optimised filter tuning.

7.7 Conclusion

The KF is a common algorithm for SOC estimation of LIC. In literature a great variety of different validation methods exist, wherein the test conditions are restricted. In consequence, the estimation error of the filter is often evaluated for one specific temperature and current profile, neglecting the influence of dynamic temperature and high or low-dynamic current loads on the filter performance. Furthermore, a comparison of different filter algorithms is limited due to the large scope of different validation methods. To quantify the performance of 18 different Kalman filters the validation method presented in Chapter 5 is used. The method consists of three profiles, where low-dynamic, high-dynamic and long-term scenarios are applied at $-10\,°C$, $0\,°C$, $10\,°C$, $25\,°C$ and $40\,°C$. In this process, the algorithms are validated with a one and a two RC term ECM.

As the filter tuning determines the estimation behaviour and accuracy, all KFs use the same filter tuning parameters to allow a comparison of the different algorithm types. Moreover, the ECM is initialised at $25\,°C$ at every temperature to investigate the influence on the KFs behaviour. The estimation accuracy results at temperatures greater than $25\,°C$ show similar behaviour for all algorithms. At temperatures below $25\,°C$ the differences in the SOC estimation increases between the filters. This effect is increased during high-dynamical profiles in the SOC range from $90\,\%$ to $10\,\%$. Repeating the experiments with the ECM initialised at $10\,°C$ shifts the optimum towards the initialised temperature. In contrast to high-dynamic loads, during low-dynamic loads the amount of RC terms has no effect on the estimation behaviour.

Depending on the precision of the fitted ECM parameters, a two RC term model can increase the accuracy during high-dynamic loads. However, the estimation accuracy decreases with an increasing deviation of the ECM parameters caused by the temperature. Inaccurate initialised parameters can be corrected by a dual estimation algorithm, which increases the SOC estimation accuracy. The improvement in SOC estimation accuracy depends on the temperature and the amount of RC terms. The DEKF with one RC term shows a more accurate parameter estimation than the DAEKF.

To show the importance of the filter tuning and the correctness of the ECM parameters, four different filters are tuned individually for two temperatures. Compared with the investigations with a fixed set of filter tuning and ECM parameters, the four filters show a similar estimation accuracy and transient behaviour for both temperatures.

It is observed that the filter tuning and the ECM parameters are significant for the estimation performance, but the filter type is not. Advantages of the different filters arise in the mathematical calculation methods, which may result in a lower computational effort or memory usage. However, it is shown that different filter types require different tuning for optimal estimation results.

In this chapter the correct OCV for all experiments was assumed. However, the OCV of the

investigated cell (Section 6.3) changes during lifetime. For this reason the following chapter shows the influence of a changed OCV on the state estimation with a KF.

8 Influence of change in open circuit voltage on the state of charge estimation

In the previous Chapter 7, the influence of the ECM parameters on the state estimation is shown. Therefore, the correct OCV is used at the corresponding temperature. However, according to Section 6.3 the OCV has a non-negligible dependency on the temperature and changes during lifetime. The scope of this chapter is to show the influence of the change in OCV on the SOC estimation.
Given that different KFs provide similar results (Chapter 7), the EKF with the one RC term ECM is selected for the following investigations because of its common use. The experiments are performed with cells of CG1 (validation profiles) and CG2 (OCVs). Based on the results of Section 6.3 the IC-OCV is used due to high influences of the impedance of aged cells to the CC-OCV. Due to invalid estimation results for the old cell (SOH=82.5 %) at −10 °C, this temperature is ignored within this study.

First in this chapter, the SOC deviations resulting from an incorrect OCV–SOC relation are shown ($\Delta SOC_{\mathrm{OCV}}$, Section 8.1). Afterwards, these deviations are compared to the influence on the SOC estimation with the EKF ($\Delta SOC_{\mathrm{Est}}$, Section 8.2).

Parts of this chapter were previously published in [167].

8.1 State of charge determination by the open circuit voltage

In this section, the temperature and ageing influence of the SOC determination by the IC-OCV is presented. Therefore, the SOC deviation resulting from two OCVs in different ageing states is defined as:

$$\Delta SOC_{\mathrm{OCV,Z}xy} = \mathrm{SOC}(\mathrm{OCV_{Z}}x) - \mathrm{SOC}(\mathrm{OCV_{Z}}y) \tag{8.1}$$

whereby, Z_x and Z_y correspond to the OCV at the different ageing state. Similar to Fig. 6.8b, Fig. 8.1a shows the OCV at different temperatures (0 °C, 40 °C) and ageing states ($\mathrm{OCV_{Z1}}$, $\mathrm{OCV_{Z3}}$). It can be seen that, except the $\mathrm{OCV_{Z3}}$ at 0 °C, all curves are overlapping until a SOC of approximately 20 %.
The SOC deviation between $\mathrm{OCV_{Z1}}$ and $\mathrm{OCV_{Z2}}$ ($\Delta SOC_{\mathrm{OCV,Z12}}$) as well as $\mathrm{OCV_{Z1}}$ and $\mathrm{OCV_{Z3}}$ ($\Delta SOC_{\mathrm{OCV,Z13}}$) at 40 °C and 0 °C are shown in Fig. 8.1b. At 40 °C the deviation of $\Delta SOC_{\mathrm{OCV,Z12}}$ and $\Delta SOC_{\mathrm{OCV,Z13}}$ increases with decreasing SOC until 20 %. Between 0 %

and 20 % the deviation decreases again, whereby at a SOC of 20 % the maximum deviation is approximately −3.7 %. Due to the lower gradient of the OCV at 0 °C (Fig. 6.8a), the overall deviation ΔSOC is higher than at 40 °C and decreases with decreasing SOC. At a SOC lower than 30 %, ΔSOC is comparable to the SOC deviation at 40 °C for both ageing stages. The maximum deviation of $\Delta SOC_{\mathrm{OCV,Z12}}$ and $\Delta SOC_{\mathrm{OCV,Z13}}$ at 0 °C is approximately −6 % and −8.9 % at a SOC between 70 % and 90 %, respectively.

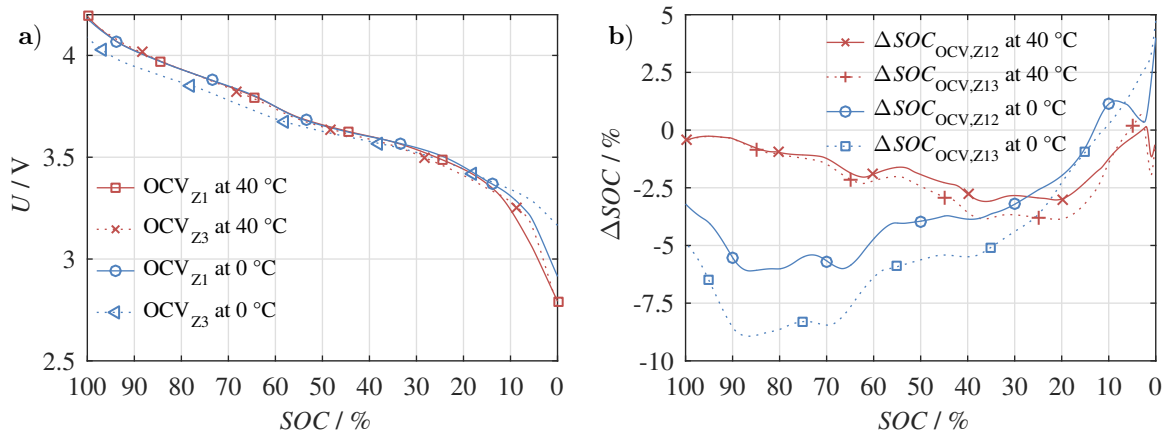

Figure 8.1: Temperature and ageing dependency of the OCV determined by the IC method: (a) OCV of the new (Z1) and old cell (Z3) at 40 °C and 0 °C; (b) SOC error at 40 °C and 0 °C of the aged cells (Z2, Z3) based on the OCV of the new cell (Z1) at 40 °C.

8.2 State of charge estimation by the Kalman filter

As the focus of this chapter is the influence of the change in OCV on the estimation accuracy at different ageing states, further investigations regarding estimation accuracy, transient behaviour or failure stability of the EKF are beyond the scope of this study.

To investigate the influence of the OCV at different ageing states, the following experiments are performed. First, the used cells (Section 4.1) are surveyed with the measurement setup introduced in Section 4.3. In this way, the OCV is determined (Section 4.4.2). Secondly, the validation profile B (Chapter 5) of the new cell of CG1 (Chapter 7) at different temperatures is used for all experiments in this chapter to be comparable to the previous results. The EKF is initialised at every temperature with the corresponding ECM parameters of the used cell. Furthermore, the filter tuning is fixed to the same initial tuning parameters as used in Chapter 7 (Appendix D Table D.1). In addition, these parameters are not changed for different temperatures or ageing states. For the simulations, the OCV–LUTs at the different ageing states are varied. So, the OCV is the only changing parameter, hence, the OCV influence on the estimation is isolated.

In Fig. 8.2a the results of the EKF with the three different OCVs at the different ageing states at 0 °C are shown. Additionally, the reference (Ref) determined by the Coulomb counter of

the CTS is depicted. Here, a parallel offset of the SOC estimation with $\mathrm{OCV_{Z2}}$ and $\mathrm{OCV_{Z3}}$ is observable.

Fig. 8.2b gives the deviation from the reference (ΔSOC). The EKF using the OCV of the new cell Z1 shows almost identical behaviour compared to the reference. The difference between the filter and the reference is approximately $\pm 1\,\%$, whereas higher deviations are observable at very low SOCs. The RMS error between the reference and the estimation is smaller than $0.6\,\%$ for this ageing scenario. For the estimation with $\mathrm{OCV_{Z2}}$ and $\mathrm{OCV_{Z3}}$ the RMS error increases to $5.56\,\%$ and $8.05\,\%$, respectively. At a SOC lower than $20\,\%$ the estimated SOC starts to decline. This behaviour can be explained by the increasing resistances $R_{\mathrm{dc1\,s}}$ and R_1 (Chapter 6). Consequently, the KF adjusts the SOC to lower values to compensate the resulting increase of overpotentials, although it is observed that this behaviour is dependent on the filter tuning as well.

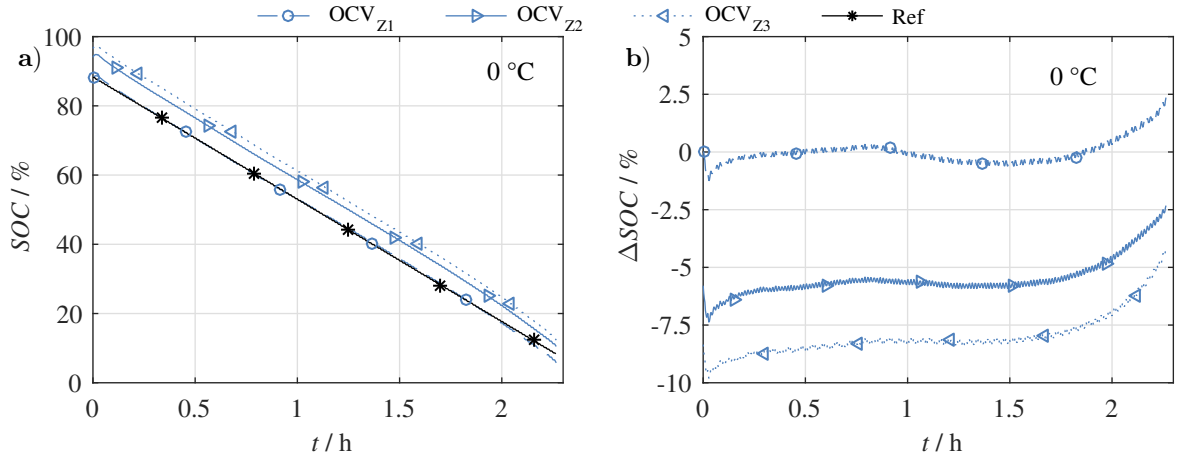

Figure 8.2: SOC estimation results with profile B of the new cell of CG1 at 0 °C: (a) estimation with the OCV of Z1, Z2 and Z3 and the reference; (b) SOC deviation between the estimation and the reference.

As one can see in Fig. 8.1b, the ageing dependency of the OCV increases with decreasing temperature. In Fig. 8.3a this influence on the estimation at 0 °C and 40 °C is shown. To allow a better comparability with Fig. 8.1, and due to different test lengths at 0 °C and 40 °C, the x-axis is represented in SOC estimated with $\mathrm{OCV_{Z1}}$. $\Delta SOC_{\mathrm{Est,Z12}}$ and $\Delta SOC_{\mathrm{Est,Z13}}$ corresponds to the deviation between the estimation by the EKF with $\mathrm{OCV_{Z1}}$ and the estimation by the EKF with $\mathrm{OCV_{Z2}}$ and $\mathrm{OCV_{Z3}}$, respectively. The estimation at 0 °C shows the maximum deviation of $-8.6\,\%$ at a SOC of $90\,\%$ and decreases to $-6.5\,\%$ with decreasing SOC. In case of the estimation at 40 °C the deviation increases with decreasing SOC from $-0.55\,\%$ to $-2.4\,\%$. By comparing $\Delta SOC_{\mathrm{Est,Z12}}$ and $\Delta SOC_{\mathrm{Est,Z13}}$ at 0 °C and 40 °C an inverse behaviour can be observed. At 0 °C the difference between $\Delta SOC_{\mathrm{Est,Z12}}$ and $\Delta SOC_{\mathrm{Est,Z13}}$ decreases, whereas the difference increases at 40 °C. It is notable, that in Fig. 8.1b a similar behaviour is observed.

In order to compare the RMS deviation of the SOC determination by the OCV–SOC relation (Fig. 8.1b) with the estimation by the EKF (Fig. 8.3a), the results are summarised in Fig. 8.3b

over the investigated temperature range. Here, an increase of $\Delta SOC_{\mathrm{RMS}}$ with decreasing temperature is observable. However, the deviation of the estimation by the EKF ($\Delta SOC_{\mathrm{Est}}$) shows higher values. At 0 °C the difference between $\Delta SOC_{\mathrm{OCV,Z12}}$ and $\Delta SOC_{\mathrm{Est,Z12}}$ or $\Delta SOC_{\mathrm{OCV,Z13}}$ and $\Delta SOC_{\mathrm{Est,Z13}}$ increases for 2 % or 3 %, respectively. For the SOC estimation by the EKF ($\Delta SOC_{\mathrm{Est}}$) the RMS error increases to 4.2 % and 6.5 % for the estimation with $\mathrm{OCV_{Z2}}$ and $\mathrm{OCV_{Z3}}$, respectively. This behaviour can be explained by additional model uncertainties at low temperatures and the constant filter tuning (Chapter 7).

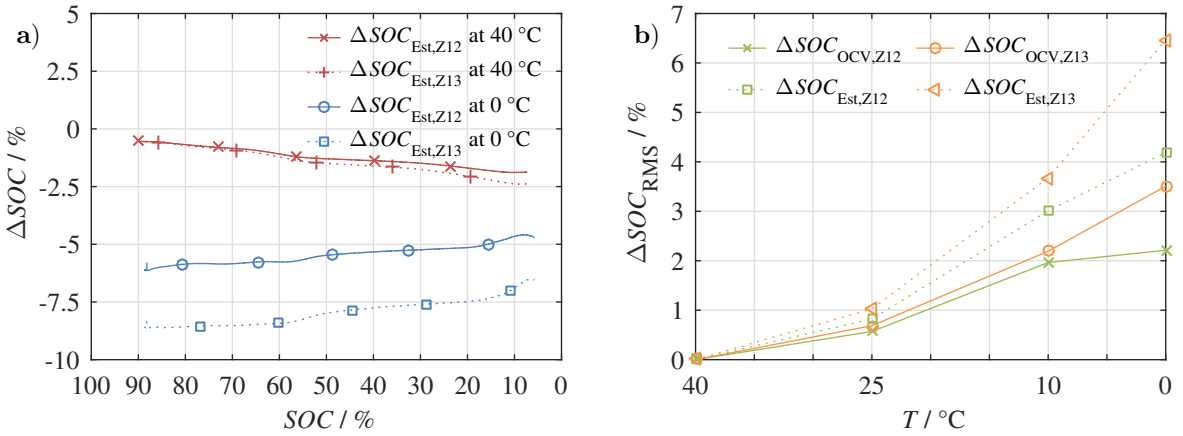

Figure 8.3: SOC estimation results: (a) SOC deviation between the estimation with $\mathrm{OCV_{Z3}}$ and the estimation with $\mathrm{OCV_{Z3}}$ and $\mathrm{OCV_{Z3}}$ at 0 °C and at 40 °C; (b) RMS deviation $\Delta SOC_{\mathrm{OCV}}$ and $\Delta SOC_{\mathrm{Est}}$ in the investigated temperature range.

The EKF uses not only the cell voltage for the state estimation, but also the Coulomb counter. The weighting of these two inputs is set by the filter tuning. Here, a compromise between accuracy and the ability to correct initialisation and measurement errors has to be found (Section 3.3). With the filter tuning of Table D.1 (Appendix D) both requirements are fulfilled (Chapter 7). If the weighting of the voltage measurement is increased by setting the process noise Q_{SOC} from 10^{-15} to 10^{-11}, the estimated SOC reacts more sensitively to a change in the terminal voltage U, which is dependent on the OCV.
Repeating the experiment and comparing Fig. 8.4a with Fig. 8.1c a similar behaviour can be observed. Consequently, the influence of the OCV–SOC correlation on the estimation is increased.
Fig. 8.4b compares the RMS deviation of the SOC determination by the OCV–SOC correlation with the estimation by the EKF over the investigated temperature range. Compared to Fig. 8.3b, the difference between $\Delta SOC_{\mathrm{OCV,Z12}}$ and $\Delta SOC_{\mathrm{Est,Z12}}$, or $\Delta SOC_{\mathrm{OCV,Z13}}$ and $\Delta SOC_{\mathrm{Est,Z13}}$ at 0 °C is reduced from 2 % or 3 % to 0.34 % or 0.54 %, respectively.

As one can see, the ageing of the OCV results in an influence on the estimation depending on the filter tuning. This in turn leads to high estimation errors in an application, if the cell ages and the OCV is not adapted to the cells condition.

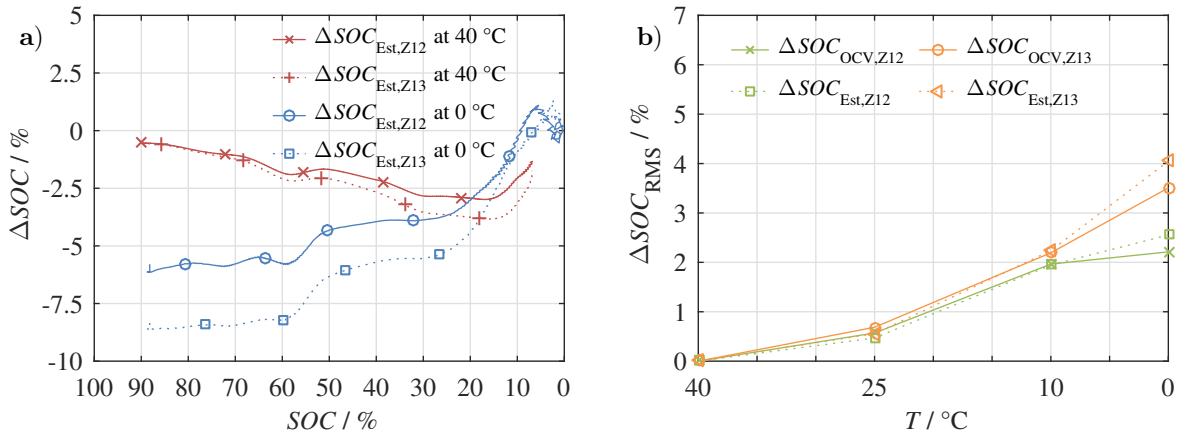

Figure 8.4: SOC estimation results with changed filter tuning: (a) SOC deviation between the estimation with OCV_{Z3} and the estimation with OCV_{Z3} and OCV_{Z3} at 0 °C and 40 °C; (b) RMS deviation ΔSOC_{OCV} and ΔSOC_{Est} in the investigated temperature range.

8.3 Conclusion

The EKF is a common algorithm for state of charge estimation of LICs. Therefore, the filter uses the OCV–SOC relation as a reference. Consequently, the accuracy of this relation is a requirement for an accurate and stable SOC estimation. Therefore, the temperature and ageing dependency of the OCV–SOC relation at 0 °C, 10 °C, 25 °C and 40 °C with three cells at different ageing states (SOH of 98.3 %, 90.4 % and 82.5 %) is investigated.

The results show a RMS deviation of approximately 3.5 % and 0.7 % in SOC at 0 °C and 25 °C, respectively, when the OCV–SOC relation of the new cell is compared to that of the aged cell. By using the validation method based on the SLC, it is shown that the deviation of the SOC estimation by the EKF increases to a RMS deviation of 6.5 % and 1 % at 0 °C and 25 °C, respectively. This deviation is further affected by the filter tuning. Changing the filter tuning increases the influence of the OCV on the SOC estimation.

This chapter showes the influence of the changed OCV, due to ageing, on the state estimation. To get a deeper insight into the progress of OCV changes during ageing, the next chapter presents an ageing study with a focus on the OCV.

9 Ageing behaviour of open circuit voltage at single cell and module level

In this chapter the results of the ageing study at single cell and module level according to Section 4.6 are discussed. However, a detailed investigation of ageing effects is not the focus of this work.
Firstly, Section 9.1 shows the observations at cell level (CG3). Here, the loss of capacity, increase of impedance and the OCV development over the cell's lifetime is presented. Then, Section 9.2 shows the results of the ageing study at module level. Therefore, two modules are constructed with cells from CG4 according to Section 4.2. This ageing study is compared to the results from [163] (CG5) to assess the ageing scalability from single cell to module level. In addition to the capacity and impedance development, temperature distribution within the modules, balancing effort and the SOI over lifetime is shown. The change in OCV is presented at the modules end of life (EOL) and compared to the OCV at the EOL at cell level (CG3).

Parts of this chapter were previously published in [162].

9.1 Ageing at single cell level

9.1.1 Capacity and resistance development

The experimental results comprise 30 months of testing, which corresponds to 2500 EFC and a driven distance of approximately 250 000 km. Fig. 9.1 illustrates the capacity fade and the increase in resistance of single cells at 40 °C, 25 °C and 10 °C (calendar ageing only) at the low SOC level L (3.7 V) and high SOC level H (4.1 V) (Section 4.6). Therefore, the results are normalised (C_{norm}, R_{norm}) to the first corresponding value. Except at 10 °C all experiments are performed with two cells. Due to a rather identical ageing behaviour the results of only one cell are shown with respect to clarity.
For the long-term cycling (Fig. 9.1a), the graph shows a slower ageing of the cells cycled at the low SOC level. At 2500 EFC the capacity loss at 25 °C results to 12.4 % compared to 14.8 % at 40 °C. For the cells cycled at a higher SOC level, the capacity degradation is increased. After 2500 EFC the capacity is reduced to 84.6 % at 25 °C. This corresponds to a 3 percentage points higher degradation compared to the capacity degradation at lower SOC. The cell cycled at high SOC at 40 °C reached the EOL criteria of 80 % SOH at approximately 2000 EFC. At this point, the cell cycled at lower SOC retained 86.5 % of the capacity, which decreases to 85.1 % at 2500 EFC.

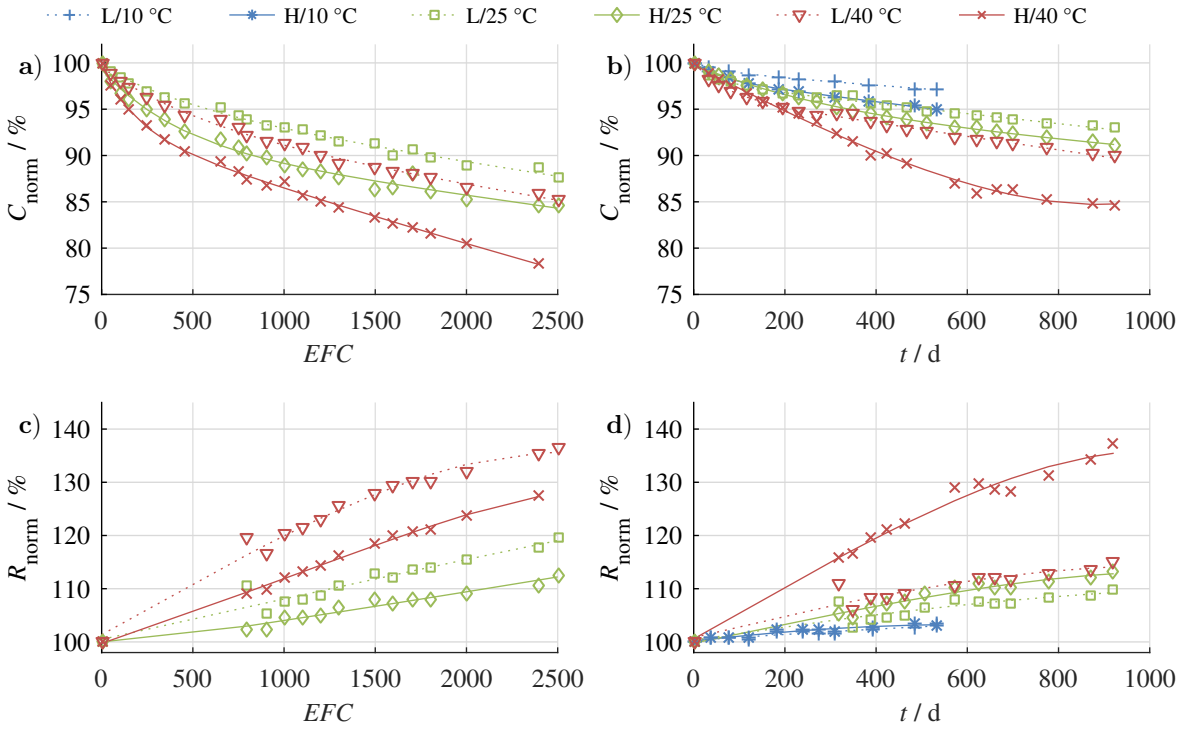

Figure 9.1: Ageing at the cell level at low (L) and high (H) SOC at 10 °C (calendar ageing only), 25 °C and 40 °C: (a) capacity degradation during cycling ageing; (b) capacity degradation during calendar ageing; (c) resistance increase during cycling ageing; (d) resistance increase during calendar ageing.

In Fig. 9.1b the capacity loss during calendar ageing is shown. The ageing experiments for the cells at 10 °C started approximately one year after the experiments at 25 °C and 40 °C. Similarly to the cycling ageing, the degradation of the cell increases with increasing temperature. However, the loss of capacity is lower than during cyclic ageing. At 25 °C and 40 °C at low SOC the degradation after the time duration of 2500 EFC (920 days) is 7 % and 10 %, respectively. This corresponds, approximately, to a 5 percentage point lower ageing at both temperatures.

Fig. 9.1c and Fig. 9.1d show the resistance increase during cyclic and calendar ageing, respectively. Interestingly, the resistance increase during cyclic ageing (Fig. 9.1c) at low SOC is higher than at high SOC, but the capacity loss behaves contrarily. This result is shown with both cells in this ageing condition and also in [175]. The reason for this behaviour could arise from a destroyed SEI during cycling and a subsequent reaction of the electrolyte with lithiated graphite (LiC_6) lithium cations. This leads predominantly to a growing layer of inorganic lithium salts, which is linked to an impedance increase [107; 113, p. 30].

The calendar ageing (Fig. 9.1d) shows how the resistance typically increases faster with rising temperatures and SOC. Nevertheless, the resistance of the cell aged at 40 °C and high SOC shows more intensive ageing than that of the cyclic ageing. This may be caused by migrated cathodic oxidation products to the anode, which favour the production of highly resistive compounds during the SEI growth [98; 113; 115, p. 30].

9.1.2 Changes of the open circuit voltage

Now, the ageing influence on the OCV is shown. Therefore, Fig. 9.2 shows the voltage change over the SOC range from 0 % to 100 % compared to the OCV in the new state. The results are related to the last measurement point of each ageing condition and the OCVs are determined by the CC method.

Fig. 9.2a presents the voltage difference $\Delta U = \mathrm{OCV}_{\mathrm{new}} - \mathrm{OCV}_{\mathrm{old}}$ for the cyclic ageing study. In [123] a shift in the electrode balancing during calendar ageing is observed. This is also assumed during cyclic ageing. As a consequence the OCV changes and results in a flatter shape [146]. This change is noticed as SOC dependent waves in Fig. 9.2a, with three remarkable local maxima at approximately 80 %, 50 % and 10 %. The decline between 60 % and 50 % SOC as wells as between 20 % and 10 % SOC indicate a transition between the voltage plateaus of the anode potentials, whereas the decline between 90 % and 80 % SOC can be assigned to a transition between a voltage plateau of the cathode potential [123]. The position of the peaks depends on the electrode balancing [123]. Furthermore, the voltage difference shows an decreasing trend from 100 % to approximately 10 % SOC, then the difference decreases in the strongly declining voltage of the OCV. The voltage difference increases with decreasing capacity. For the cycled cell at 40 °C and high SOC, ΔU results to a maximum voltage difference of −66 mV at a SOC of 12 %.
Similar results are observable during the calendar ageing study (Fig. 9.2b). Due to the lower capacity degradation compared to the cyclic ageing study, the voltage differences are lower. However, the maximum difference is observed in the same ageing condition at approximately the same SOC of 10 % (ΔU=−41 mV). Similar to the capacity degradation, the voltage difference correlates with the temperature and SOC level during ageing.

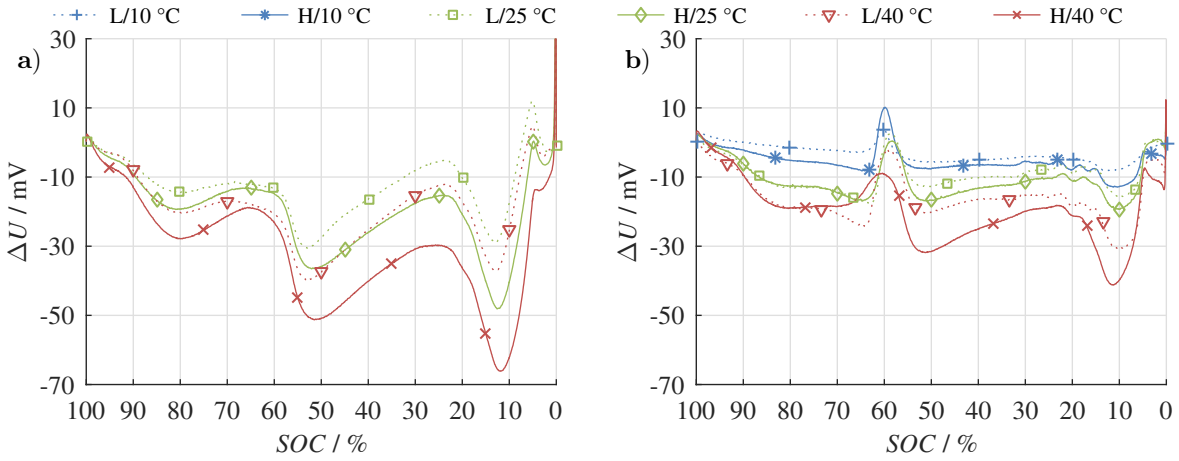

Figure 9.2: Voltage difference between new and aged OCV for different temperatures and SOC levels: (a) cyclic ageing; (b) calendar ageing.

Fig. 9.3a shows the voltage difference of cells with a retained capacity of approximately 90 %. Furthermore, the mean difference of these is illustrated. It can be seen that the cycled cells

show a similar behaviour. The small deviations arise from the unequal ageing state of 90 %. However, the calendar aged cells differ from the cycled cells.
These differences are more clearly observable with the DVA (Section 4.5.4) in Fig. 9.3b. Compared to the DVA of the cycled cells, the DVA from the calendar aged cells shows a remarkable peak at approximately 60 % SOC and two additional peaks between 20 % and 10 % SOC. Calendar ageing is mainly provoked by a shift in the electrode balancing [123], which is visible by the moving peak at a SOC of approximately 60 %. It is shown in [121] that during cyclic ageing these peaks decrease further.

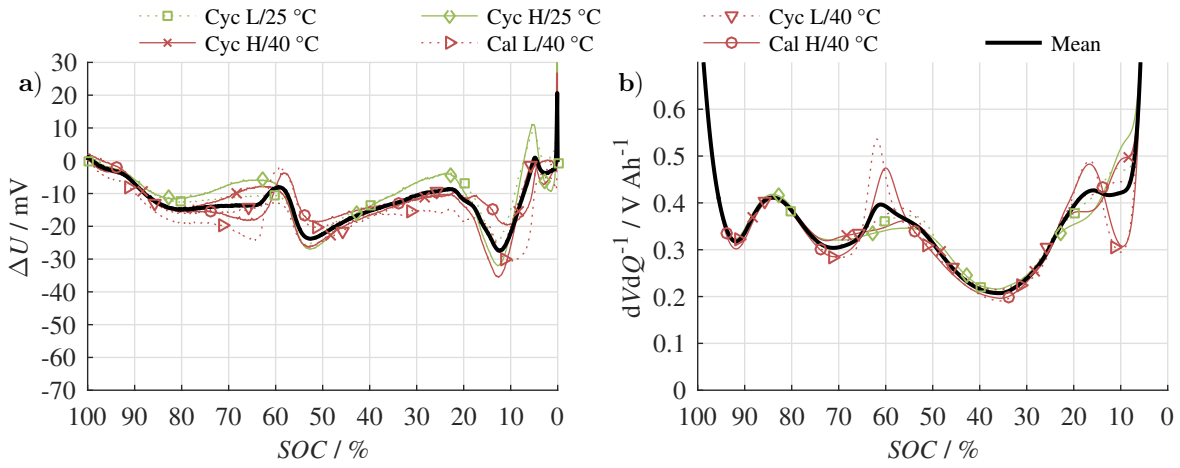

Figure 9.3: (a) Voltage difference between new and aged OCV: cyclic and calendar ageing at a retained capacity at approximately 90 %; (b) differential voltage analysis of aged cells: cyclic and calendar ageing at a retained capacity at approximately 90 %.

To emphasise the influence of the change in OCV on the SOC determination by the OCV–SOC relation, Fig. 9.4a shows the increasing SOC error during cyclic ageing at 40 °C and high SOC.

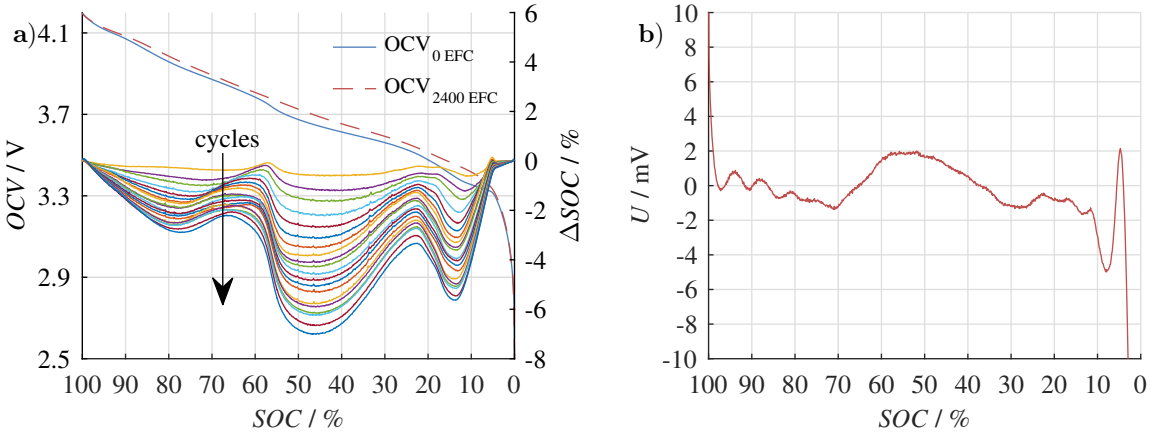

Figure 9.4: (a) impact of a change in OCV to the OCV–SOC relationship (left axis: OCV, right axis: SOC deviation); (b) difference of the CC-OCV and the IC-OCV method (for OCV determination see Section 4.4.2) at 25 °C at the cells EOL.

Therefore, the SOC difference ΔSOC is defined as the difference between the OCV-based

SOC at 25 °C of the new cell and the OCV-based SOC of the cell after 2400 EFC at the same voltage:

$$\Delta SOC = \mathrm{SOC}(\mathrm{OCV}_{0\mathrm{EFC}}) - \mathrm{SOC}(\mathrm{OCV}_{2400\mathrm{EFC}}) \tag{9.1}$$

Similarly to the voltage differences, three local maxima are visible at 80 %, 50 % and 10 %. As one can see, the error resulting from the changing OCV–SOC relation increases to 7 % and 5.6 % at a SOC of approximately 40 % and 10 %, respectively.
As previously mentioned in Section 6.3, Fig. 9.4b verifies that at the cell's EOL, the difference between the CC and the IC method at 25 °C is negligible. The mean error over the complete SOC range is 2 mV.

Due to the need for an accurate SOC, especially at a low SOC, the peak between 20 % and 10 % is investigated in more detail. Therefore, Fig. 9.5 shows the correlation between ΔSOC and the EFC, time or C_{act}. Fig. 9.5a and Fig. 9.5b show the increase of ΔSOC during cyclic and calendar ageing, respectively. The exponentially decreasing behaviour is quite similar to the capacity degradation shown in Fig. 9.1.

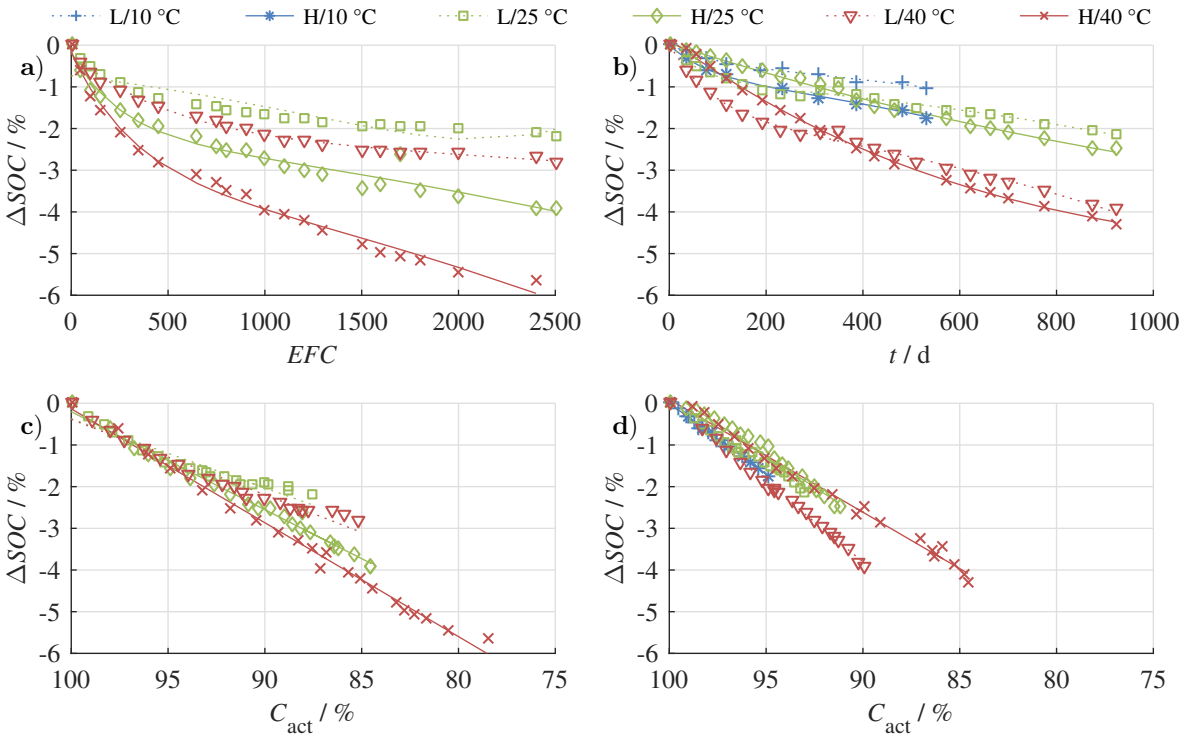

Figure 9.5: Development of the SOC error between 10 % and 20 % SOC resulting from a changing OCV over lifetime: (a) vs. EFC (cyclic ageing); (b) vs. time (calendar ageing); (c) vs. actual capacity C_{act} (cyclic ageing); (d) vs. actual capacity C_{act} (calendar ageing)

Fig. 9.5c and Fig. 9.5d show the correlation between ΔSOC and the corresponding actual capacity C_{act}. In order to analyse the correlation, regression curves are calculated for each ageing condition. It can be observed that during cyclic ageing, at high SOC the error increases linearly with C_{act}. However, the cells cycled at low SOC show a linear behaviour up to

95 %, then the decline decreases (Fig. 9.5d) and consequently the regression value (Table 9.1) decreases too. For the calendar ageing only, at high SOC and at 25 °C, the gradient changes at 95 % which results in a decreasing regression value. In contrast to the peak at a SOC of 50 % and 10 %, the peak at 80 % shows a weak correlation.

Table 9.1: Regression value r of the correlation between SOC error and capacity degradation

	L/10 °C	H/10 °C	L/25 °C	H/25 °C	L/40 °C	H/40 °C
Cyclic ageing	-	-	0.962	0.993	0.977	0.997
Calendar ageing	0.996	0.999	0.991	0.988	0.998	0.995

In order to identify a general trend in the error development with the capacity degradation, this ageing matrix is not sufficient. Further experiments are required to model the OCV change during lifetime. However, these results emphasise the importance of a correct OCV–SOC relation for OCV based algorithms. Furthermore, it should be investigated if the findings are applicable to other LIB technologies.

9.2 Ageing at module level

9.2.1 Capacity and resistance development of modules

Fig. 9.6a shows the normalised capacity fade of the ageing experiment. At the beginning, the development at the module level shows good agreement with the one at the single cell level. From 600 EFC a slower ageing behaviour is observed for the modules which, however, shows stronger fluctuation. This may have originated from temperature fluctuations during the check-ups in the self-made temperature chamber, because of fluctuating room temperature, or from a different short-term cell history before the capacity measurement was performed. A different history may have arisen from a varying time difference between cycling and check-up. It is observed that a longer rest between cycling and check-up results in a higher capacity. The dependency on the rest duration is also observed at the block level. The deviations between the modules and the single cell at 1200 EFC are 2.01 % and 1.21 % for M1 and M2, respectively.

In Fig. 9.6b, the resistance evolution of M1 and M2 is compared with the one at the cell level. The resistance trend of M1 is similar to the single cell. At 1200 EFC, the deviation between M1 and the single cell is 5 %. The offset between cell and module is caused by the slower ageing behaviour at the beginning of the experiment at the cell level. In contrast, the resistance of M2 increases faster. This is mainly caused by the resistance of one block (Fig. 9.7d). The deviation between the module and the cell resistance is 20.3 %. The higher resistance also explains the lower capacity of M2 because the cut-off voltage during check-up is reached earlier and so less charge is obtained. Because of the CCCV check-up at the block level, the capacity development is not influenced by the higher resistance (Fig. 9.7b).

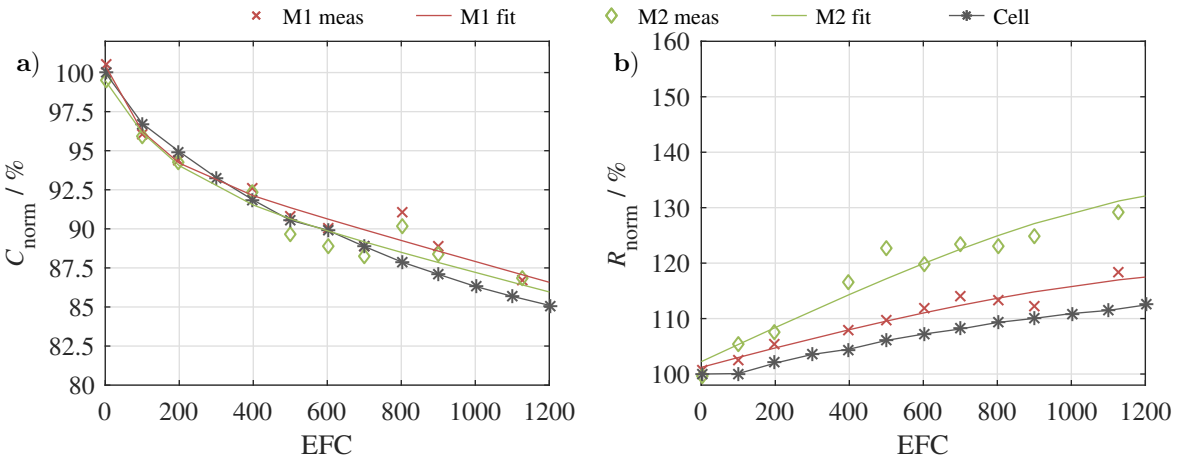

Figure 9.6: Capacity and resistance development during cyclic ageing at 40 °C: a) module capacities; b) module resistances.

9.2.2 Capacity and resistance of single blocks

In Fig. 9.7a and Fig. 9.7b, the capacity degradation for each block of M1 and M2 is depicted. At the block level, the capacities for both modules are higher because of the additional CV phase during check-ups. According to Section 4.5.1, such a CV phase is not possible at module level. After 1200 EFC, the average differences between the remaining capacities of the eight blocks and the result from the ageing study at the cell level is 2.42 % and 2.59 % for M1 and M2, respectively.

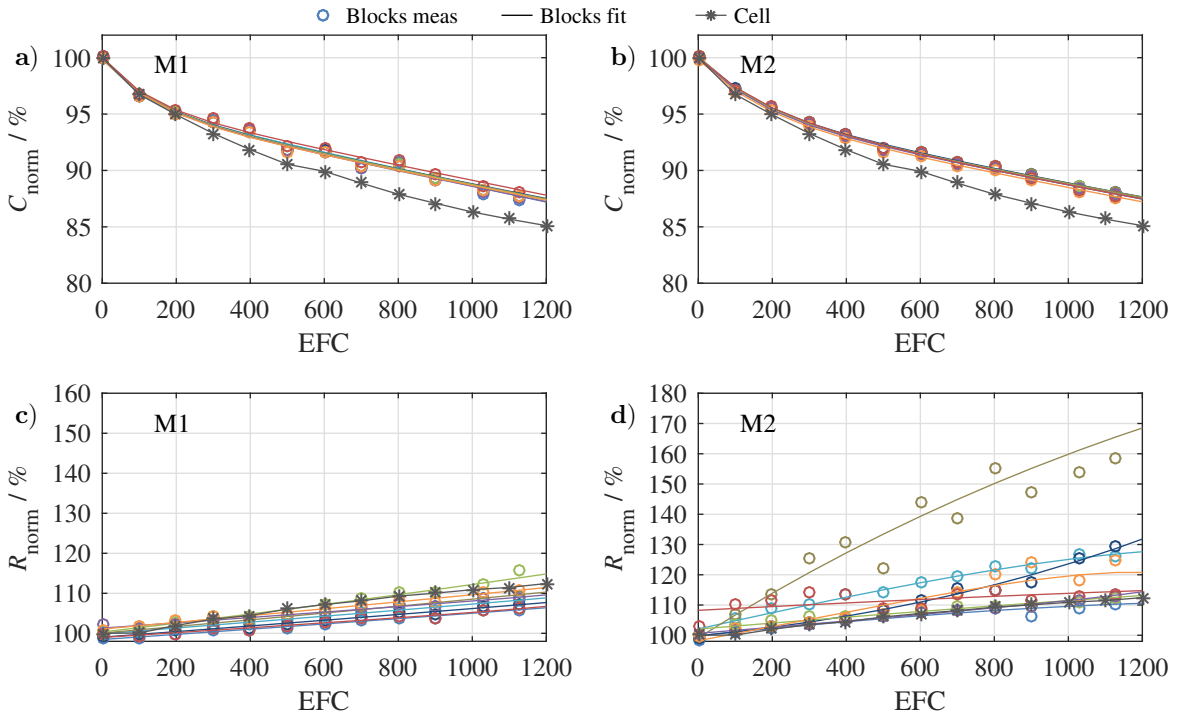

Figure 9.7: Capacity and resistance development during cyclic ageing at 40 °C: a) block capacities of module 1; b) block capacities of module 2; c) block resistances of module 1; d) block resistances of module 2.

Finally, capacity losses at the cell level were higher than these at the module level and especially higher than these at the block level. The deviation can be explained by two reasons:

Reason 1: During the capacity measurements, the temperature increases because of the discharge current of more than 1 C. In the module, the temperature increases substantially more than at the cell level because of heat accumulation. At the beginning of the ageing study, the maximum temperature in each block was approximately 10 K higher during the module check-ups compared with single cell check-ups. During the progress of ageing, the mean module temperature during check-ups also increased owing to the increasing resistance. The maximum temperature difference between each block and single cells rises to 15 K. This may lead to the higher capacity measured during check-ups of modules as improved cell kinetics and decreased resistances would be expected to allow for additional capacity to be extracted from the cell before reaching the cut-off voltage.
In contrast to that, the temperature at the cell level remains approximately constant during the progress of ageing, despite an increasing cell resistance, because a single cell exhibits a much better heat transfer to the ambient air compared to a module. To evaluate the influence of the elevated temperature during capacity measurements, a check-up at 1200 EFC with only one block was performed. This resulted in a maximal temperature of 35 °C compared with 47 °C when all blocks were measured together. The difference of 12 K led to a measured capacity decrease of 0.3 %. The temperature dependency of the capacity of LIC has e.g. been reported in [83; 122] and shown in Chapter 6.

Reason 2: The average temperature of the module is lower compared with that of the single cell, which was cycled at constant 40 °C. This leads to a slower ageing behaviour at the module level. At the beginning of the ageing experiment, the minimum block temperature of M1 is 36.5 °C during the cycling procedure. Because of increasing cell resistances, the dissipated heat also increases. At 1200 EFC, the minimum temperature reaches 38.5 °C and the maximum block temperature increases from 38.5 °C to 40.5 °C. For M2 the minimum temperature increases from 37.5 °C to 39 °C and the maximum temperature from 39.5 °C to 41.5 °C. The ageing behaviour at elevated temperatures is mainly caused by calendar ageing effects [163] and has also been observed for NMC based cells [100; 176].
From the calendar ageing investigations at the single cell level (CG5 [163]), the influence of a deviation of 2 K in the mean temperature during cycling can be derived: Fig. 9.8 reveals the usage-independent calendar ageing, in terms of capacity fade, in relation to cell temperature at the high SOC, which corresponds to the start SOC of the cycle life study. As one can see, usage-independent calendar ageing increases clearly for temperatures above 30 °C. Each additional degree increases the degradation notably. The slope of the usage-independent capacity fade at 40 °C reveals that a variation in temperature of 1 K leads to a difference in the remaining capacity of 0.18 % and 0.3 % after 5 and 12 months of storage, respectively. Regarding the "12 months" curve, a deviation in temperature of 2 K leads to a difference in capacity fade of 0.6 %. Hence, variations in temperature are observed to have a considerable impact on the cycle life for high-temperature operating conditions.

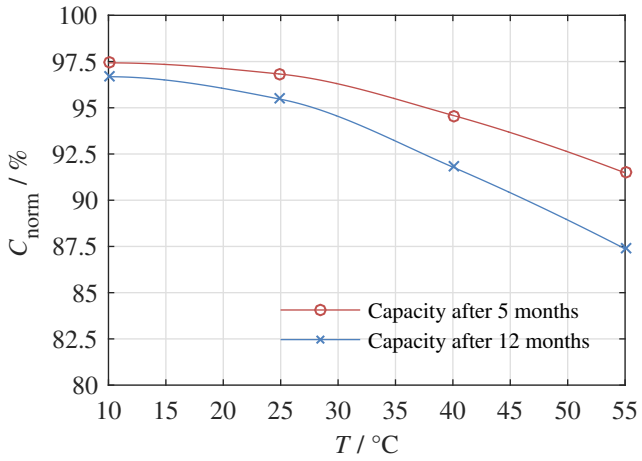

Figure 9.8: Ageing at the cell level at high SOC: influence of temperature on calendar ageing.

The higher temperature during check-ups and the lower mean temperature during cycling have a total effect of 0.9 %, which can reduce the deviation between the single cell and the block level to 1.52 % and 1.69 % for M1 and M2, respectively.

Fig. 9.7c and Fig. 9.7d show the resistance increase at the block level. Similar to the module level, the resistance evolution of M1 is in good agreement with the ageing behaviour of the single cell. After 1200 EFC the mean difference between the resistance increase of the eight blocks and the single cell is 2.8 %. The deviation is lower than at the module level because of the missing copper rails and bolted connections between blocks.
For M2, a strong spread of resistances is observable. Blocks two, three and four in particular display a massive resistance increase compared with the other blocks. In total, there is a mean deviation of 13.2 % caused by the three outlier blocks in the module. Regarding the capacity ageing behaviour, a faster degradation of these blocks is not observable. This might be caused by a bad welding spot, resulting in a relatively higher contact resistance, which would also provoke an increased generation of heat on the tab, which in turn leads to a faster corrosion of the welded connections between cell tab and Hilumin, as well as between Hilumin and copper. Hence, it can be assumed that the resistance increase mainly originates from the deteriorated connections, in contrast to a distinct cell ageing. This unpredictable resistance increase can lead to an unstable estimation behaviour of SKFs and DKFs, caused by an ECM and filter tuning not designed for this failure case.
After disassembling M2 back to the single cell level by mechanically removing the Hilumin and copper connectors, this assumption could be confirmed. The measured resistance of block four at 1200 EFC is 2.93 mΩ and the sum, according to Eq. 4.2, of the single cell resistances is 1.82 mΩ. The difference between these values corresponds to the approximate contact resistance of 1.11 mΩ. Similar values are calculated for blocks two (0.78 mΩ) and three (1.05 mΩ). The other contact resistances are around 0.5 mΩ, which can be regarded as the resistance of a proper connection.

The results show that the ageing at the module level does not progress faster than at the single cell level and weak welding spots can continuously deteriorate the module performance. The reasons behind the slower ageing of the module need to be investigated in more detail, although, temperature and contact resistances have been identified as influencing factors.

9.2.3 State of inhomogeneity during the progress of ageing

Fig. 9.9a and Fig. 9.9b show the development of the capacity and resistance SOI of the blocks of both modules, respectively (Section 4.5.3). The parameter α represents the SOI of the selected 112 single cells of both modules in the new state, before assembly calculated by Eq. 4.3. For the capacities (Fig. 9.9a), the SOI_{C} of the individual cells is 0.63 % for M1 and 0.57 % for M2. For the resistances (Fig. 9.9b), the cell-based SOI_{R} results in 3.53 % and 3.15 % for M1 and M2, respectively.
In the next step, the cells are connected and then the SOI calculation is repeated at the block level for both modules (eight blocks). When the cells were selected by coincidence, the calculated SOI_{C} and SOI_{R} would result in 0.12 % and 0.55 %, respectively, for both modules (β in Fig. 9.9). These values represent the computed mean of 1000 coincident cell selections. Capacity-based cell matching (Section 4.2.3) reduces the theoretical ideal SOI_{C} to 0.032 % and 0.014 % for M1 and M2, respectively. This ideal matching is represented by the parameter γ in Fig. 9.9. For the resistances, which are not matched actively, the SOI_{R} results in 0.5 % and 1 % for M1 and M2, respectively. In the end, a capacity-based matching results in a lower SOI_{C}, but can lead to a higher SOI_{R} (compare β and γ of M2).

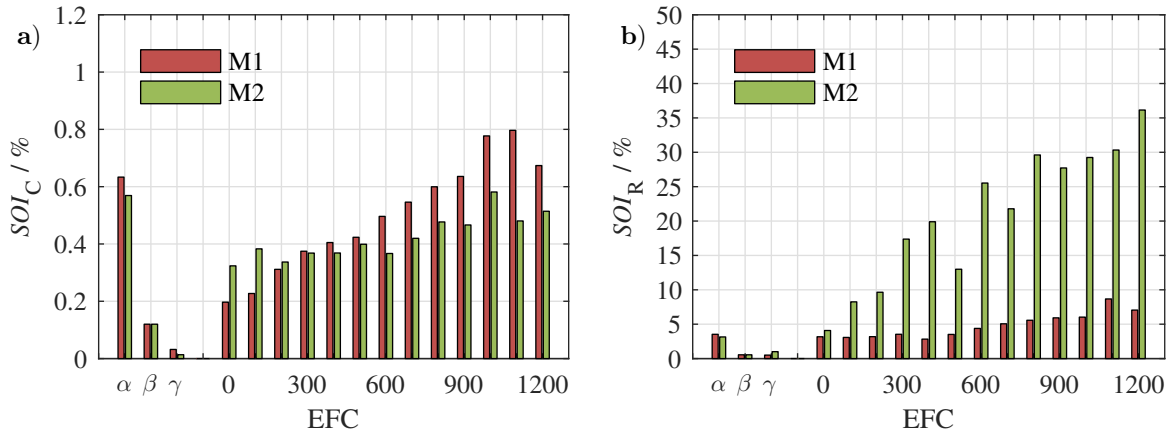

Figure 9.9: Spread of parameters over the entire ageing study: α represents the inhomogeneity for the unconnected cells, β represents the inhomogeneity of the modules with coincidently selected cells, γ represents the inhomogeneity for perfectly matched modules. The remaining bars illustrate the actual inhomogeneities in the constructed modules throughout the entire ageing procedure for (a) block capacity and (b) block resistance.

When measuring the capacities and resistances of the single blocks after the assembly of the modules, the SOI increases because of temperature gradients during module check-ups and variations in the additional contact resistances. The measured SOI_{C} rises to 0.20 %

and 0.32 % for M1 and M2, respectively. Additionally, the SOI_{R} is increased to 3.17 % and 4.08 %, respectively. Assuming that the SOI_{C} would have increased by the same amount for coincidently selected cells, capacity-based cell matching reduced the SOI_{C} by 8.8 % and 10.6 % for M1 and M2, respectively. Compared with the SOI_{C}, the SOI_{R} value is observed to decrease for M1 but to increase for M2. Here, the contact resistances distorted the block resistances. The high value for SOI_{R} of M2 is a result of the worse cell connections.
Fig. 9.9 also shows the development of the SOI during the course of ageing. Here, a linear increase of the spread between the maximal and minimal block capacity is observed (Fig. 9.9a). The SOI_{C} increases from its initial value of 0.2 % to 0.67 % and from 0.32 % to 0.51 % for M1 and M2, respectively. The SOI_{C} of M1 increases faster than that of M2, which is in accordance with a higher SOI_{C} of M1 in the new state at the single cell level. A link between the lithium-ion cell-to-cell parameter variation in the new and the aged state is reported in [132]. In Section 9.1.2 a correlation between the capacity deterioration and the change in OCV is shown. With the increasing SOI_{C} this change may differ in the blocks and can influence the state estimation on module level.
However, the block resistances behave differently. For M1, the SOI_{R} stays approximately constant until 400 EFC, after which, it starts to increase. In contrast to that, M2 is observed to increase linearly from the beginning of the experiment. Due to the higher resistance of blocks two, three and four, the SOI_{R} is also approximately five times higher than that of M1. With the outlier blocks, the SOI_{R} increases up to 36 %. Without these blocks, the SOI_{R} after 1200 EFC is 6.9 %, compared with 7 % for M1.
As M2 is disassembled after 1200 EFC, α can be calculated for the aged single cells. Then α corresponds to 3.4 % (increase by factor 6) and 17.6 % (increase by factor 5.5) for capacities and resistances, respectively. The SOI_{C} inside the blocks of M2 is in the range of 0.69 % (Block 5) to 3.08 % (Block 7). The SOI_{R} is in the range of 3.32 % (Block 2) to 15.77 % (Block 7).

9.2.4 Correlation of ageing and temperature

In Fig. 9.10a and Fig. 9.10b, the capacity degradation of the blocks of both modules are compared with the corresponding mean temperature. Until 600 EFC, the degradation correlates well with the temperature distribution. The blocks in the border areas of the modules have a lower temperature and hence a lower degradation. From 600 EFC to 1200 EFC, the behaviour changes for both modules, whereby border block one ages faster than blocks five to seven where the temperature is higher. The reason for this could be an increased influence of cell-to-cell variation [128; 132].
The cell-to-cell variation in the new state is comparably low so the inhomogeneous temperature distribution dominates the ageing behaviour. During the course of ageing, the cell-to-cell variation becomes more influential than the temperature deviation of 2 K. Thus, the blocks show a decreasing correlation between capacity fade and temperature. All in all, the differences are rather low, since the capacities have diverged less than 1 % after 1200 EFC.

The resistance increase for M1 is, except for block six, in good correlation with the temperature at 600 EFC and 1200 EFC (Fig. 9.10c). For M2, however, no correlation can be observed (Fig. 9.10d). Here, cell-to-cell and contact resistance variation might have more effect on the ageing behaviour than temperature gradients within the module.

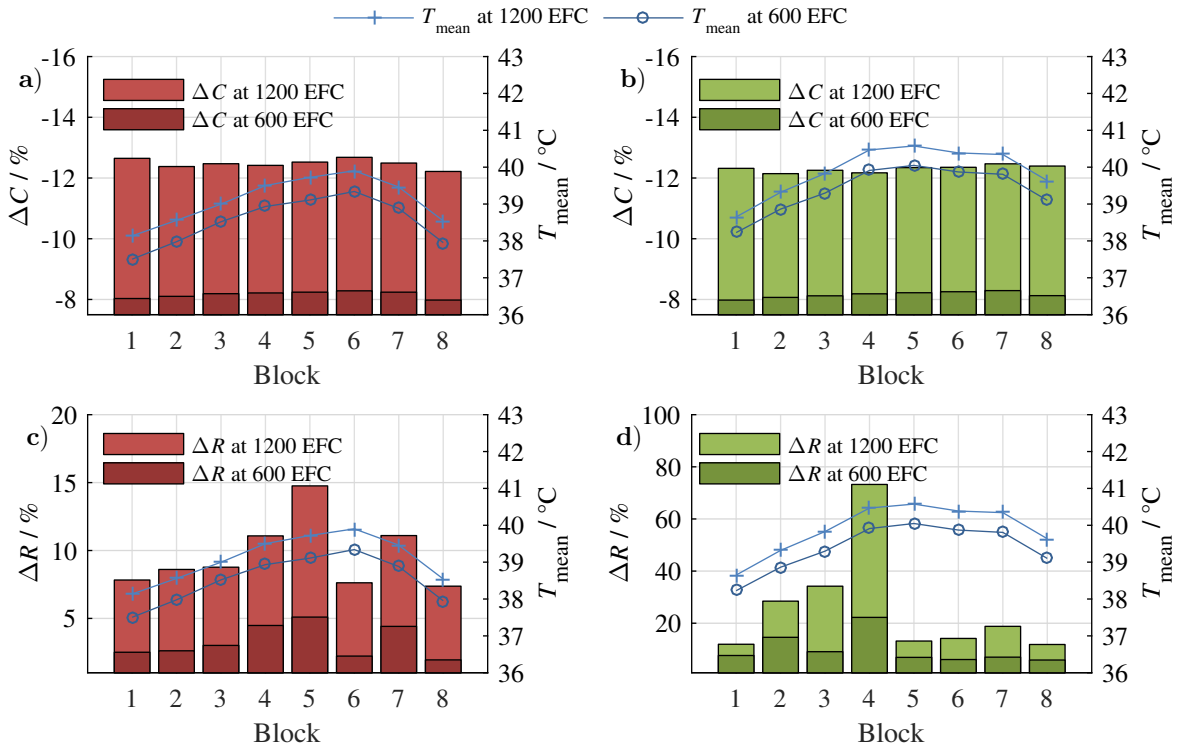

Figure 9.10: Capacity degradation (a, b) and resistance increase (c, d) with the corresponding temperature distribution at 600 EFC and 1200 EFC (please notice the different scaling of the ΔR axis).

9.2.5 Energy efficiency

Fig. 9.11 shows the energy efficiency at the cell and the module level. Because of the additional contact resistances, the energy efficiency at the system level is lower than at the cell level. It is calculated by dividing of the energy in the discharge direction by that of the charge direction. The energy efficiency of M1 decreases by 0.6 % to η_{M1}=95.03 %. In comparison, M2 decreases by 0.4 % to η_{M2}=95.23 %, which is slightly higher than η_{M1}. Due to the increase in resistance, η is observed to decrease during the course of ageing. Moreover, while M1 exhibits a parallel offset compared with the single cell, M2 decreases faster as a result of the accelerated increasing resistances. The decreased energy efficiency at the module level at 1200 EFC is 94.3 % and 94.2 % for M1 and M2, respectively, compared with an energy efficiency at the single cell level of 94.9 %.

The energy consumption of the BMS can be neglected because it was supplied by an external power source. The balancing influence on the energy efficiency is also negligible: the calculated mean difference between the energy efficiency with and without balancing is 0.0072 %. The fluctuation of M2 results from balancing faults, which is explained in the next section.

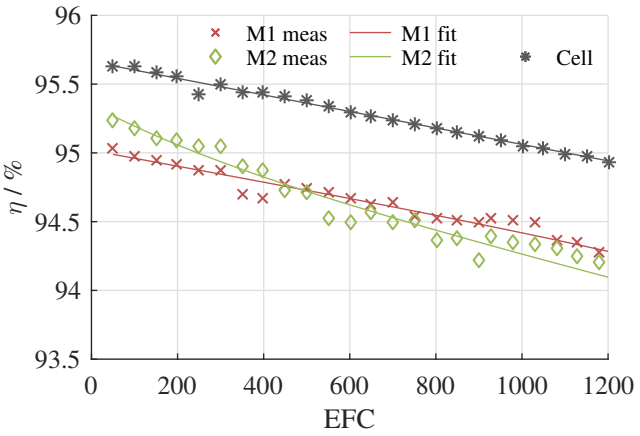

Figure 9.11: Energy efficiency

9.2.6 Cell balancing

In Fig. 9.12, the balancing behaviour of M1 and M2 during the course of ageing is shown. Every point depicts the accumulated balancing charge of all cells during 50 EFC. At the beginning, this accumulated balancing charge is 1.21 A h and 0.82 A h for M1 and M2, respectively. Therefore, the BMS balanced in large parts during the charging process after the two driving cycles (Section 4.6). At the end of the charging phase, the blocks were balanced again. After 500 EFC, the balancing charge of M2 starts to increase up to 37.1 A h, while the charge for M1 stays constant. This is also noticeable in the energy efficiency development. The balancing fault leads to a decrease in energy efficiency of:

$$\Delta\eta = \frac{\sum_{i=1}^{8} Q_{\mathrm{bal},i} \cdot \bar{U}_{\mathrm{block}}}{50\,\mathrm{EFC} \cdot \bar{Q}_{\mathrm{M2,900\,EFC}} \cdot \bar{U}_{\mathrm{block}} \cdot 8} = \frac{37.1\,\mathrm{Ah}}{50\,\mathrm{EFC} \cdot 35.79\,\mathrm{Ah} \cdot 8} = 0.26\,\% \tag{9.2}$$

Thereby, Q_{bal} is the balancing charge of every block and $\bar{U}_{\mathrm{block}}$ the mean block voltage during cycling. This is also visible in Fig. 9.11. The BMS measured the cell voltage between two cells on the copper rails (Fig. 4.1b). If the bolted connection was not tightened correctly, the BMS would also measure the voltage drop over the connection and perform balancing by mistake. Despite the use of a torque wrench to tighten the bolts in a reproducible manner, stable connection resistances could not be guaranteed. The reasons for this behaviour could have originated from polluted or oxidized contact surfaces. At 900 EFC, the contact surface appears to be clean again and the balancing behaviour returns to the level of M1, at which point, M2 follows M1 again and stays constant. The mean balancing amount from 900 EFC to 1200 EFC is 0.89 A h and 1.07 A h for M1 and M2, respectively.
The mean balancing amount of all blocks $\bar{Q}_{\mathrm{bal}}$ for M1 is 1.13 A h and the mean energy amount is 4.5 W h per 50 EFC. This corresponds to:

$$\frac{\bar{Q}_{\mathrm{bal}}}{\bar{Q}_{50\,\mathrm{EFC}}} = \frac{1.13\,\mathrm{Ah}}{3863\,\mathrm{Ah}} = 0.3\,\frac{\mathrm{mAh}}{\mathrm{Ah}} \tag{9.3}$$

or

$$\frac{\bar{E}_{\mathrm{bal}}}{\bar{E}_{50\,\mathrm{EFC}}} = \frac{4.5\,\mathrm{Wh}}{118\,\mathrm{kWh}} = 38\,\frac{\mathrm{mWh}}{\mathrm{kWh}} \tag{9.4}$$

Therefore, $\bar{Q}_{50\,\mathrm{EFC}}$ and $\bar{E}_{50\,\mathrm{EFC}}$ correspond to the mean charge and energy throughput per 50 EFC, respectively. Despite the increased SOI_{R} of M1 and particularly M2, the balancing amount did not increase in the same trend. In fact, the balancing charge of M1 is even observed to decrease. It is assumed that the variation of contact resistances has a greater influence on the balancing behaviour than inhomogeneous cell resistances and capacities.

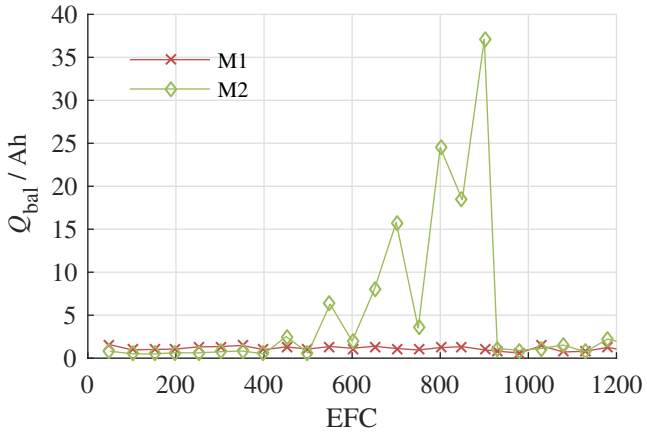

Figure 9.12: Ageing impact on cell balancing.

As one can see, due to varying contact resistances, voltage-based balancing can lead to balancing faults during ageing. A balancing strategy based on the SOC estimated by a KF could be more robust against such disturbances. Due to the low balancing activity in the faultless case, the influence of balancing on the state estimation can be neglected.

9.2.7 Changes of the open circuit voltage

In order to compare the change in OCV at module level with that at the cell level, M1 is aged till the EOL criteria (SOH=80 %) is reached. To accelerate the module ageing, the number of subsequent driving cycles was increased from two to five. Consequently, the DOD was increased from 25 % to 62.5 %, resulting in a faster degradation. The OCVs shown in this section are determined by the CC method as the IC method is not feasible at module level due to the required CCCV phase (Section 4.4.2). As already shown in Fig. 9.4, the difference of the CC and the IC method is negligible at a temperature of 25 °C.

Fig. 9.13a shows the OCV of the module, one block and one single cell. Therefore, the module was disassembled to perform the measurements at single cell level and the module voltage is scaled to cell level. The differences between cell and block as well as cell and module are illustrated in Fig. 9.13b. Here, a strong increasing deviation between cell and module is

observed at a SOC lower than approximately 5 %. This could arise from differing block SOCs as a result of differing block capacities in the module. The SOI for the capacity distribution increased to 0.8 % at the modules EOL. The deviations higher than 5 % SOC are in the range of the measurement uncertainties of the HPS (Appendix B Table B.2).

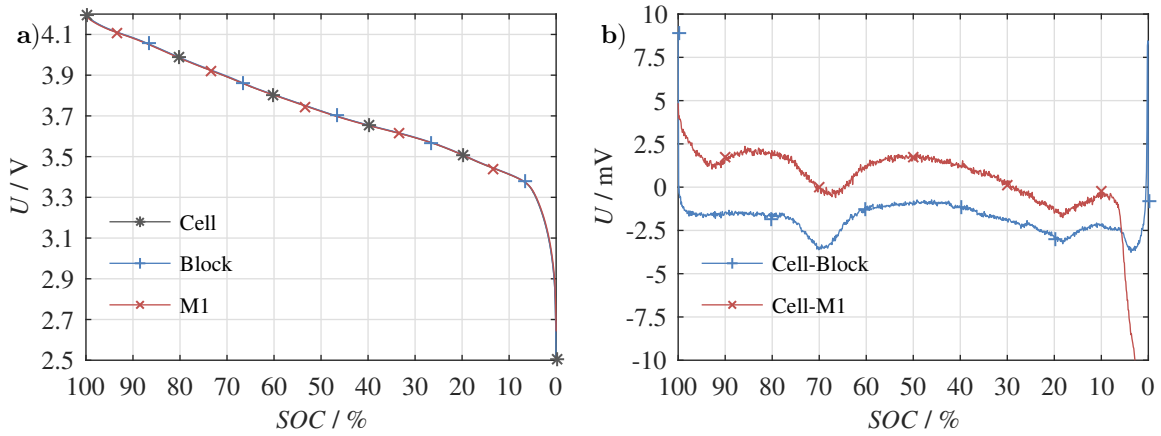

Figure 9.13: OCV at the EOL: (a) OCV at cell, block and module level (scaled to cell level); (b) difference between cell and block as well as cell and module.

Comparable to Fig. 9.3, Fig. 9.14 shows the OCV difference between single cell and module level at a SOH of approximately 80 % compared to the new state. Therefore, the module is compared to the cell from the OCV ageing study (CG3). Here, a rather similar behaviour is observed in Fig. 9.14a. Furthermore, the DVA Fig. 9.14b also shows no remarkable distinctions. The negligible differences could arise from non-identical SOHs.

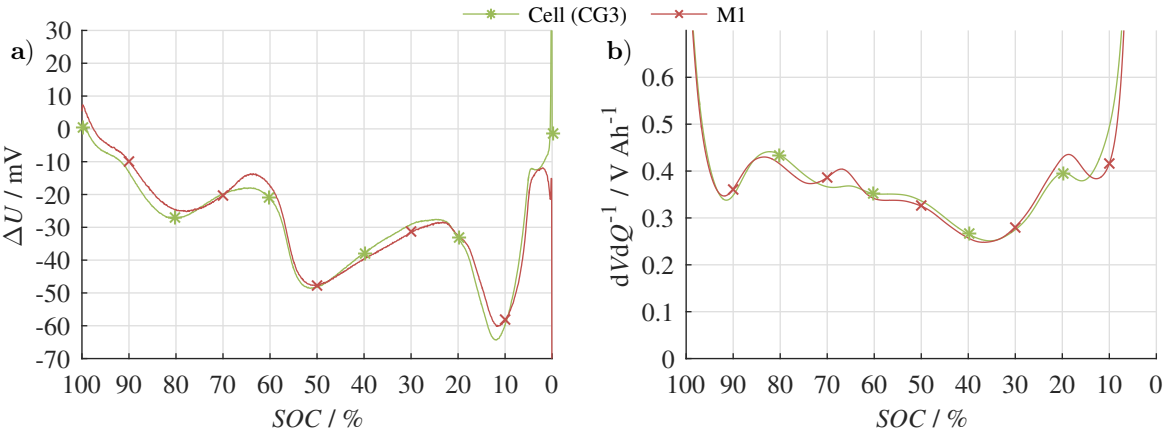

Figure 9.14: (a) Voltage difference between the OCV of the new cell from CG3 and the OCV at module level (scaled) at EOL; (b) differential voltage analysis of the cell and module OCV.

This shows, that the OCV at the single cell and module level changes during lifetime independently from the ageing condition . Moreover, due to the low SOI_C, the change in OCV can be scaled to module level during ageing. For modules with an increased inhomogeneous ageing distribution this scalability may not possible.

9.3 Conclusion

In this chapter, an ageing study of LICs is performed and the ageing of LIB modules is compared with that of single LICs. The focus of the ageing study at single cell level is the investigation of the changing OCV over lifetime, whereas the ageing study at module level investigates the ageing scalability, including the OCV.

The results at cell level show the typical behaviour at different temperatures and SOCs during cyclic and calendar ageing. The capacity degradation increases with increasing temperatures and SOCs. At a SOH of approximately 90 % the cells of all ageing conditions showed the same changes in OCV. Due to the shift in the electrode balancing during ageing, the OCV curve results in a flatter shape. As a consequence, the SOC determination, based on the OCV–SOC relation, results in a SOC dependent error of a maximum of 7 % at the EOL. This error shows linear correlation with the capacity degradation.

To accomplish the ageing study at module level, two modules with 112 cells each were built in an 8s14p cell interconnection topology. Before the cells were connected by ultrasonic and spot welding, a capacity-based cell matching procedure was performed. Thereby, the already small capacity variation of consumer cells could be further reduced, which lowered the newly defined state of inhomogeneity regarding capacity and resistance. After 1200 EFC, a capacity fade of about 12 % has been observed. In spite of resistance variations from welding and inhomogeneous temperature distributions during module check-ups, the module SOI_{C} is still lower than 1 % after 1200 EFC. This shows fairly homogeneous ageing behaviour of the used commercial high quality cells.

Initially, the ageing behaviour of the modules appeared to be quite similar to the ageing behaviour of single cells (CG5). However, the modules and their respective blocks were observed to age slower than the single cell, due to temperature influences. Test temperatures of the module ageing study were slightly lower than in the single cell ageing study. Furthermore, the capacity distribution of the module correlated with the temperature gradients for the first 600 EFC, but cell-to-cell variation seemed to dominate the ageing behaviour for the next 600 EFC.
The contact resistances were also observed to have an influence on the ageing behaviour. A higher contact resistance leads to a higher temperature development, which might accelerate the corrosion of the contact, which in turn could lead again to increased contact resistance. So, the cell resistances only seemed to be higher. The disassembling of one module confirmed that the contact resistances and not the cell resistances increased substantially. The contact resistances of the weak blocks were about twice as high as these of the other blocks. However, this appeared to have no impact on capacity loss. Furthermore, the additional contact resistances were a stronger influence on the balancing behaviour of the BMS than the spreading of capacities and resistances. Therefore, the charge amount during the equalisation process stayed approximately constant over lifetime, while the SOI of capacity and resistance was observed to increase.

The investigations into balancing also showed that dissipative balancing is sufficient for modules with a capacity which is typical for BEV applications.

To compare the OCV at EOL at module level with the OCV at the single cell level, the DOD in the module ageing study is increased to accelerate the ageing. After disassembling the module, the scalability of the OCV from single cell to module level is shown and the OCV is compared to the cell ageing study with the cells of CG3. At EOL a rather identical change in OCV is observed. This is the requirement for scaled state estimation at module level.

Part IV

Final Conclusion

10 Summary and further work

To finally conclude this doctoral thesis, the key messages of each chapter are summarised in Section 10.1. Therefore, new findings regarding the objectives defined in the introduction (Chapter 1) are given to answer the main topic about the "*Practical feasibility of Kalman filters for the state estimation of lithium-ion batteries*". Furthermore, Section 10.2 recommends further research topics for Kalman filtering in the field of batteries.

10.1 Summary

Part I: Literature and Fundamentals

Chapter 1 introduced the Kalman filter by a simple example about estimating the altitude and velocity of a falling object. This example is compared to the application of a Kalman filter in the field of batteries. Therefore, non-linear and varying model uncertainties are identified as the main concerns. Based on the literature research into the key issues regarding Kalman filtering, four objectives for this thesis are identified:

Objective 1: Lithium-ion cell modelling and experimental investigation of the cell behaviour
Objective 2: Influence of equivalent circuit model parameters on different Kalman filters
Objective 3: Influence of the open circuit voltage on the state estimation
Objective 4: Changes in open circuit voltage during lifetime at cell and module level

Based on the literature research of Section 1.2.1, Chapter 2 introduced the subsequently used equivalent circuit models, consisting of: the open circuit voltage, an ohmic resistance, and one or two RC terms. Therefore, the dependencies and behaviour of each equivalent circuit model element is described by physicochemical effects, whereby the main dependencies identified are: state of charge, temperature, current and age. Variations or changes in these dependencies cause model uncertainties in a real-life application, which need to be considered when applying a Kalman filter. Moreover, this chapter derived and discretised the equations of the equivalent circuit model with nRC terms, for the use with a Kalman filter in a discrete system such as a battery management system.

The literature review about Kalman filters (Section 1.2.2) identified several variations of this algorithm. Therefore, Chapter 3 introduces the general Kalman filter implementation and calculation sequence and presented the differences between the various types. Here, three

different algorithm groups are discovered:

- filter for linear models, assuming Gaussian distributed noise
- filter for non-linear models, assuming Gaussian distributed noise
- filter for non-linear models, assuming non Gaussian distributed noise

For the second point a dual estimator and a noise adapting type is also presented. Nevertheless, all Kalman filters require an initial guess for the measurement noise, process noise (representing model uncertainties) and covariance matrices. Furthermore, this chapter introduces the filter tuning process to find these initial guesses. This chapter aims to show the mathematical differences of the Kalman filter variations. However, in the result and discussion Part III the differences during applications are presented.

Part II: Solution Approach

In Chapter 4 the experimental part is presented. Alongside the introduction of the used lithium-ion cell and the battery module design, the methodology for the experiments performed in this work is described. In order to conduct the different measurements, five cell groups are defined for the single experiments.

In Chapter 5 a generalised validation and benchmark method for state estimation algorithms is developed. Therefore, identified shortcomings of present methods (Section 1.2.3) are eliminated and required test conditions based on the cell behaviour (Section 2.1) are defined. Based on a frequency analysis of 149 standardised driving cycles, a synthetic load cycle is derived for an independent validation of the low- and high-dynamic behaviour as well as long-term stability in the temperature range from $-10\,°C$ to $40\,°C$. Therefore, the measurement data for the algorithm is provided by a BMS, whereas the reference data is provided by a battery testing system. To ensure comparability, a quantitative rating technique is introduced for estimation accuracy, transient behaviour, drift behaviour, failure stability, temperature stability and residual charge estimation to evaluate the performance of different state estimation algorithms. This method is used in the result and discussion Part III to compare different Kalman filters and to investigate the influence of equivalent circuit model parameters.

Part III: Results and Discussion

In the results and discussion part the objectives identified in Part I are investigated:

Objective 1: Lithium-ion cell modelling and experimental investigation of the cell behaviour

To compare the recorded behaviour with equivalent circuit model parameters presented in literature (Section 2.1), Chapter 6 investigates the dependencies regarding state of charge, temperature, current and age. Objective 1 aims to evaluate the parameters of a one and two RC term equivalent circuit model and to compare the results with these presented in

literature:

- Compared to the ohmic resistance, the RC term exhibits a high dependency on the state of charge and an increased dependency on current with decreasing temperature.
- Temperature dependency of the RC term time constant is dependent on state of charge.
- Temperature dependency of the resistance measured one second after a current pulse and the actual capacity changes during lifetime.
- The two considered open circuit voltage determining methods show a temperature dependency over the state of charge. The state of charge error based on the open circuit voltage–state of charge relation increases during lifetime, especially at low temperatures.
- These deviations are lowered by using the incremental-open circuit voltage method.
- The results of this work are in accordance with these presented in literature.

Objective 2: Influence of equivalent circuit model parameters on different Kalman filters

Chapter 7 investigates the influence of the cell behaviour on the state of charge estimation with different Kalman filters introduced in Chapter 3. Accordingly, the validation and benchmark method described in Chapter 5 is used and all filters are initialised with the same filter tuning. Comparing the Kalman filters with these presented in literature is not possible due to varying validation methods and conditions, as well as different initialisations of the measurement noise, process noise and covariance matrices. Objective 2 aims to compare the introduced algorithms under identical test conditions and to investigate the influence of equivalent circuit models and parameters:

- Equivalent circuit model parameters have a strong influence on the state estimation independently from the Kalman filter type.
- The equivalent circuit model influence decreases during a low-dynamic load and increases with decreasing temperature.
- The estimation performance is optimal at the temperature at which the equivalent circuit model is initialised.
- An additional parameter estimation leads to enhanced performance of the state estimation, dependent on temperature and dynamic. The parameter estimation is more precise with the lower complex equivalent circuit model.
- All algorithms show a similar behaviour and the most accurate and stable Kalman filter is not distinguishable.
- To evaluate the importance of the filter tuning parameters, an individual filter tuning further decreased the differences between the Kalman filters and the overall performance is increased.
- It is reasoned that whilst the filter type is not significant for the estimation performance, the correct equivalent circuit model parameters and the filter tuning certainly are.

Objective 3: Influence of the open circuit voltage on the state estimation

In contrast to Chapter 7, Chapter 8 investigates the influence of change in open circuit voltage, due to ageing, on the state of charge estimation. Subsequently, the open circuit voltages of three cells in different ageing states are applied to a Kalman filter at temperatures in the range of 0 °C to 40 °C. Objective 3 aims to consider both methods and to investigate the error in state of charge estimation based on the open circuit voltage–state of charge relation and the error during estimation with a Kalman filter:

- Compared to a new cell, the open circuit voltage–state of charge relation shows an increasing error as the cells ages, especially at decreasing temperatures.
- The influence of the aged open circuit voltages on the state estimation with a Kalman filter increases with decreasing temperature and shows higher errors when compared to the investigations of the open circuit voltage–state of charge relation.
- The influence of the open circuit voltage is dependent on the filter tuning.

Objective 4: Changes in open circuit voltage during lifetime at single cell and module level

In order to emphasise the presented influence of a change in open circuit voltage, due to ageing, on the estimation performance, the changing open circuit voltage is observed during lifetime. Therefore, an ageing study at single cell level is performed. The growing number of cells in a battery pack require a state estimation at module or pack level, due to the limited calculation power and memory of a battery management system. Therefore, an additional ageing study on module level is performed, to investigate the scalability of the ageing behaviour of the open circuit voltage. Objective 4 aims to perform the ageing studies and to investigate the change in open circuit voltage and the resulting increase in state of charge error at cell and module level:

- An increasing state of charge dependent open circuit voltage change leads to an increasing error in the open circuit voltage–state of charge relation.
- Differential voltage analysis shows that this changing progress is independent from the ageing condition.
- The changes in the open circuit voltage shape correlates with the capacity degradation.
- The state of inhomogeneity affects the open circuit voltage of the module at very low SOCs.
- At the single cell's and module's end of life, both open circuit voltages show a rather identical shape.

Fig. 10.1 summarises all results by considering the correlation between temperature and age, regarding the influence on the estimation performance. The four objectives of this thesis show that a Kalman filter, independent from its type, estimates the state of charge accurately close to the initial conditions. Assuming constant equivalent circuit model parameters and

filter tuning, the estimation performance decreases at temperatures different from the initial temperature. In addition, the equivalent circuit model parameters change during lifetime. As a result the temperature dependency also increases, and consequently, the loss of estimation performance is further enhanced. Neither a dual estimation of state of charge nor equivalent circuit model parameters can reduce this performance loss, due to the lack of filter tuning knowledge. Filter tuning is associated with the dynamic of the cell and the model uncertainties, which change with temperature and age. Regarding the state estimation at module level, production tolerances at single cell and module level, inhomogeneous temperature distributions within modules and contact resistances further increase model uncertainties.

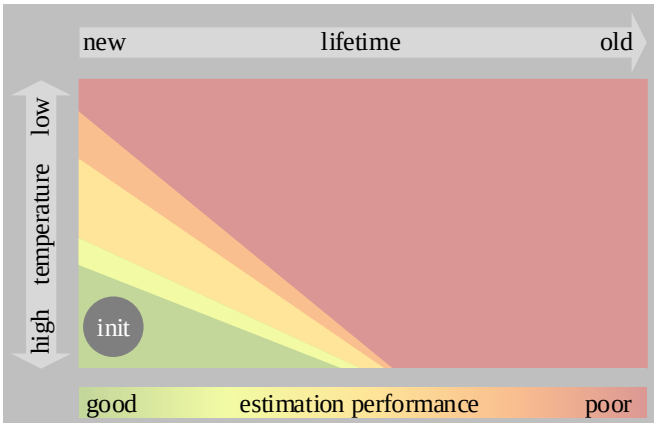

Figure 10.1: Scheme of the correlation between temperature and age regarding the influence on the estimation performance.

These facts conclude that the performance of the Kalman filter on cell and module level in a real application during the lifetime of a battery is significantly lower compared to the laboratory environment with its high constrains. Possibilities to extend the green area of Fig. 10.1 and consequently to enhance the feasibility are discussed in the next section.

10.2 Recommendation and outlook

The feasibility of a Kalman filter is limited due to the strong constraints of cell temperature and age. However, profound knowledge about the equivalent circuit model parameters and the behaviour during lifetime can extend the green area of Fig. 10.1.
Therefore, the equivalent circuit model requires the correct parameter values for all possible conditions (temperature, state of charge, age). Consequently, look-up tables or analytical relations of cell parameters must be available on a battery management system, which results in high memory or computational power requirements.
Implementing a Kalman filter with a parameter estimation can also extend the green area, but the filter tuning has to be adapted during the lifetime. Experiments, beyond the scope of this work, showed that the state of charge and temperature dependent gradient of the equivalent circuit model parameter can support the filter tuning procedure. Therefore, it is assumed that

higher gradients result in increased model uncertainty due to the fast changing nature of the cell behaviour. However, these parameters are based on fitting algorithms, which in turn are also dependent on parameters. If these gradients are assumed to be approximately constant, this method reduces memory or computational power requirements of a battery management system, compared to the changing equivalent circuit model parameters over lifetime.
A more suitable method is to reduce the estimation complexity and/or increase the model accuracy by updating model parameters and the OCV, based on signal analysis. Determining, for example, the resistance measured one second after a current pulse, based on the voltage and current relation (Ohm's law) reduces the parameter estimation by one dimension and/or increases the model accuracy and consequently the estimation performance. However, high demands on online signal filtering are required.

References

[1] W. Waag, C. Fleischer, and D. U. Sauer. "Critical review of the methods for monitoring of lithium-ion batteries in electric and hybrid vehicles". In: *J. Power Sources* 258 (2014), pp. 321–339. DOI: 10.1016/j.jpowsour.2014.02.064.

[2] R. E. Kalman. "A New Approach to Linear Filtering and Prediction Problems". In: *J. Basic Engineering* 82.1 (1960), p. 35. DOI: 10.1115/1.3662552.

[3] G. L. Plett. "Extended Kalman filtering for battery management systems of LiPB-based HEV battery packs Part 1. Background". In: *J. Power Sources* 134.2 (2004), pp. 252–261. DOI: 10.1016/j.jpowsour.2004.02.031.

[4] G. L. Plett. "Extended Kalman filtering for battery management systems of LiPB-based HEV battery packs Part 2. Modeling and identification". In: *J. Power Sources* 134.2 (2004), pp. 262–276. DOI: 10.1016/j.jpowsour.2004.02.032.

[5] G. L. Plett. "Extended Kalman filtering for battery management systems of LiPB-based HEV battery packs Part 3. State and parameter estimation". In: *J. Power Sources* 134.2 (2004), pp. 277–292. DOI: 10.1016/j.jpowsour.2004.02.033.

[6] P. Zarchan and H. Musoff. *Fundamentals of Kalman filtering: A practical approach.* 3rd ed. Vol. 232. Progress in astronautics and aeronautics. Reston and Va: American Institute of Aeronautics and Astronautics, 2009.

[7] W. Waag, S. Käbitz, and D. U. Sauer. "Experimental investigation of the lithium-ion battery impedance characteristic at various conditions and aging states and its influence on the application". In: *Appl. Energy.* 102 (2013), pp. 885–897. DOI: 10.1016/j.apenergy.2012.09.030.

[8] R. Garcia-Valle and J. A. Peças Lopes. *Electric Vehicle Integration into Modern Power Networks.* New York, NY: Springer New York, 2013. DOI: 10.1007/978-1-4614-0134-6.

[9] X. Han, M. Ouyang, L. Lu, and J. Li. "Simplification of physics-based electrochemical model for lithium ion battery on electric vehicle. Part II: Pseudo-two-dimensional model simplification and state of charge estimation". In: *J. Power Sources* 278 (2015), pp. 814–825. DOI: 10.1016/j.jpowsour.2014.08.089.

[10] A. P. Schmidt, M. Bitzer, Á. W. Imre, and L. Guzzella. "Model-based distinction and quantification of capacity loss and rate capability fade in Li-ion batteries". In: *J. Power Sources* 195.22 (2010), pp. 7634–7638. DOI: 10.1016/j.jpowsour.2010.06.011.

[11] S. Santhanagopalan and R. E. White. “Online estimation of the state of charge of a lithium ion cell”. In: *J. Power Sources* 161.2 (2006), pp. 1346–1355. DOI: 10.1016/j.jpowsour.2006.04.146.

[12] A. M. Bizeray, S. Zhao, S. R. Duncan, and D. A. Howey. “Lithium-ion battery thermal-electrochemical model-based state estimation using orthogonal collocation and a modified extended Kalman filter”. In: *J. Power Sources* 296 (2015), pp. 400–412. DOI: 10.1016/j.jpowsour.2015.07.019.

[13] C. F. Chiasserini and R. R. Rao. “Pulsed battery discharge in communication devices”. In: *Proceedings of the 5th International Conference on Mobile Computing and Networking* (1999), pp. 88–95. DOI: 10.1145/313451.313488.

[14] P. Singh and A. Nallanchakravarthula. “Fuzzy Logic Modeling of Unmanned Surface Vehicle (USV) Hybrid Power System”. In: *Proceedings of the 13th International Conference on Intelligent Systems Application to Power Systems* (2005), pp. 261–267. DOI: 10.1109/ISAP.2005.1599273.

[15] J. Zhang, S. Ci, H. Sharif, and M. Alahmad. “An enhanced circuit-based model for single-cell battery”. In: *25th annual IEEE Applied Powr Electronics Conference and Exposition* (2010), pp. 672–675. DOI: 10.1109/APEC.2010.5433597.

[16] K. Fang, D. Mu, S. Chen, B. Wu, and F. Wu. “A prediction model based on artificial neural network for surface temperature simulation of nickel–metal hydride battery during charging”. In: *J. Power Sources* 208 (2012), pp. 378–382. DOI: 10.1016/j.jpowsour.2012.02.059.

[17] J. Kim, S. Lee, and B. H. Cho. “Complementary Cooperation Algorithm Based on DEKF Combined With Pattern Recognition for SOC/Capacity Estimation and SOH Prediction”. In: *IEEE T Power Electr* 27.1 (2012), pp. 436–451. DOI: 10.1109/TPEL.2011.2158554.

[18] Z. Chen, S. Qiu, M. Masrur, and Y. L. Murphey. “Battery state of charge estimation based on a combined model of Extended Kalman Filter and neural networks”. In: *International Joint Conference on Neural Networks (IJCNN 2011 - San Jose)*. 2011, pp. 2156–2163. DOI: 10.1109/IJCNN.2011.6033495.

[19] J. Han, D. Kim, and M. Sunwoo. “State-of-charge estimation of lead-acid batteries using an adaptive extended Kalman filter”. In: *J. Power Sources* 188.2 (2009), pp. 606–612. DOI: 10.1016/j.jpowsour.2008.11.143.

[20] F. Sun, X. Hu, Y. Zou, and S. Li. “Adaptive unscented Kalman filtering for state of charge estimation of a lithium-ion battery for electric vehicles”. In: *Energy* 36.5 (2011), pp. 3531–3540. DOI: 10.1016/j.energy.2011.03.059.

[21] Y. He, X. Liu, C. Zhang, and Z. Chen. “A new model for State-of-Charge (SOC) estimation for high-power Li-ion batteries”. In: *Appl. Energy.* 101 (2013), pp. 808–814. DOI: 10.1016/j.apenergy.2012.08.031.

[22] Y. Wang, C. Zhang, and Z. Chen. “A method for joint estimation of state-of-charge and available energy of LiFePO4 batteries”. In: *Appl. Energy.* 135 (2014), pp. 81–87. DOI: 10.1016/j.apenergy.2014.08.081.

[23] Y. Wang, C. Zhang, and Z. Chen. “A method for state-of-charge estimation of Li-ion batteries based on multi-model switching strategy”. In: *Appl. Energy.* 137 (2015), pp. 427–434. DOI: 10.1016/j.apenergy.2014.10.034.

[24] Y. Wang, C. Zhang, and Z. Chen. “State-of-charge Estimation of Lithium-ion Batteries Based on Multiple Filters Method”. In: *Energy Procedia* 75 (2015), pp. 2635–2640. DOI: 10.1016/j.egypro.2015.07.354.

[25] Y. Wang, C. Zhang, Z. Chen, J. Xie, and X. Zhang. “A novel active equalization method for lithium-ion batteries in electric vehicles”. In: *Appl. Energy.* 145 (2015), pp. 36–42. DOI: 10.1016/j.apenergy.2015.01.127.

[26] F. Yang, Y. Xing, D. Wang, and K.-L. Tsui. “A comparative study of three model-based algorithms for estimating state-of-charge of lithium-ion batteries under a new combined dynamic loading profile”. In: *Appl. Energy.* 164 (2016), pp. 387–399. DOI: 10.1016/j.apenergy.2015.11.072.

[27] L. Wang, L. Wang, C. Liao, and J. Liu. “Sigma-point Kalman filter application on estimating battery SOC”. In: *IEEE Vehicle Power and Propulsion Conference (VPPC).* 2009, pp. 1592–1595. DOI: 10.1109/VPPC.2009.5289604.

[28] G. L. Plett. “Sigma-point Kalman filtering for battery management systems of LiPB-based HEV battery packs Part 2: Simultaneous state and parameter estimation”. In: *J. Power Sources* 161.2 (2006), pp. 1369–1384. DOI: 10.1016/j.jpowsour.2006.06.004.

[29] J. Lee, O. Nam, and B. H. Cho. “Li-ion battery SOC estimation method based on the reduced order extended Kalman filtering”. In: *J. Power Sources* 174.1 (2007), pp. 9–15. DOI: 10.1016/j.jpowsour.2007.03.072.

[30] S. Lee, J. Kim, J. Lee, and B. H. Cho. “State-of-charge and capacity estimation of lithium-ion battery using a new open-circuit voltage versus state-of-charge”. In: *J. Power Sources* 185.2 (2008), pp. 1367–1373. DOI: 10.1016/j.jpowsour.2008.08.103.

[31] J. Kim and B. H. Cho. “State-of-Charge Estimation and State-of-Health Prediction of a Li-Ion Degraded Battery Based on an EKF Combined With a Per-Unit System”. In: *IEEE T Veh Technol* 60.9 (2011), pp. 4249–4260. DOI: 10.1109/TVT.2011.2168987.

[32] H. He, R. Xiong, and H. Guo. “Online estimation of model parameters and state-of-charge of LiFePO4 batteries in electric vehicles”. In: *Appl. Energy.* 89.1 (2012), pp. 413–420. DOI: 10.1016/j.apenergy.2011.08.005.

[33] X. Hu, S. Li, H. Peng, and F. Sun. “Robustness analysis of State-of-Charge estimation methods for two types of Li-ion batteries”. In: *J. Power Sources* 217 (2012), pp. 209–219. DOI: 10.1016/j.jpowsour.2012.06.005.

[34] M. Charkhgard and H. Gholizade-Narm. “Lithium-ion battery state of charge estimation based on square-root unscented Kalman filter”. In: *IET Power Electronics* 6.9 (2013), pp. 1833–1841. DOI: 10.1049/iet-pel.2012.0706.

[35] H. He, H. Qin, X. Sun, and Y. Shui. “Comparison Study on the Battery SoC Estimation with EKF and UKF Algorithms”. In: *Energies* 6.10 (2013), pp. 5088–5100. DOI: 10.3390/en6105088.

[36] G. Walder, C. Campestrini, S. Kohlmeier, M. Lienkamp, and A. Jossen. “Functionality and Behaviour of an Dual Kalman Filter implemented on a Modular Battery-Management-System”. In: *Conference on Future Automotive Technology: Focus Electromobility*. Ed. by Bayern Innovativ. 2013.

[37] R. Xiong, H. He, F. Sun, X. Liu, and Z. Liu. “Model-based state of charge and peak power capability joint estimation of lithium-ion battery in plug-in hybrid electric vehicles”. In: *J. Power Sources* 229 (2013), pp. 159–169. DOI: 10.1016/j.jpowsour.2012.12.003.

[38] R. Xiong, F. Sun, X. Gong, and H. He. “Adaptive state of charge estimator for lithium-ion cells series battery pack in electric vehicles”. In: *J. Power Sources* 242 (2013), pp. 699–713. DOI: 10.1016/j.jpowsour.2013.05.071.

[39] C. Campestrini, G. Walder, A. Jossen, and M. Lienkamp. “Temperature Influences on State and Parameter Estimation Based on a Dual Kalman Filter”. In: *Conference on Future Automotive Technology Focus Electromobility*. Ed. by Bayern Innovativ. 2014.

[40] H. Fang, X. Zhao, Y. Wang, Z. Sahinoglu, T. Wada, S. Hara, and de Callafon, Raymond A. “Improved adaptive state-of-charge estimation for batteries using a multi-model approach”. In: *J. Power Sources* 254 (2014), pp. 258–267. DOI: 10.1016/j.jpowsour.2013.12.005.

[41] F. Sun, R. Xiong, and H. He. “Estimation of state-of-charge and state-of-power capability of lithium-ion battery considering varying health conditions”. In: *J. Power Sources* 259 (2014), pp. 166–176. DOI: 10.1016/j.jpowsour.2014.02.095.

[42] G. Walder, C. Campestrini, M. Lienkamp, and A. Jossen. “Adaptive State and Parameter Estimation of Lithium-Ion Batteries based on a Dual Linear Kalman Filter”. In: *The Second International Conference on Technological Advances in Electrical, Electronics and Computer Engineering*. Ed. by Asia Pacific University of Technology and Innovation. 2014, pp. 16–24.

[43] H. He, Z. Liu, and Y. Hua. “Adaptive Extended Kalman Filter Based Fault Detection and Isolation for a Lithium-Ion Battery Pack”. In: *Energy Procedia* 75 (2015), pp. 1950–1955. DOI: 10.1016/j.egypro.2015.07.230.

[44] H. He, R. Xiong, and J. Peng. “Real-time estimation of battery state-of-charge with unscented Kalman filter and RTOS uCOS-II platform”. In: *Appl. Energy.* (2015). DOI: 10.1016/j.apenergy.2015.01.120.

[45] J. Klee Barillas, J. Li, C. Günther, and M. A. Danzer. "A comparative study and validation of state estimation algorithms for Li-ion batteries in battery management systems". In: *Appl. Energy.* 155 (2015), pp. 455–462. DOI: 10.1016/j.apenergy.2015.05.102.

[46] Y. Zou, X. Hu, H. Ma, and S. E. Li. "Combined State of Charge and State of Health estimation over lithium-ion battery cell cycle lifespan for electric vehicles". In: *J. Power Sources* 273 (2015), pp. 793–803. DOI: 10.1016/j.jpowsour.2014.09.146.

[47] G. Dong, Z. Chen, J. Wei, C. Zhang, and P. Wang. "An online model-based method for state of energy estimation of lithium-ion batteries using dual filters". In: *J. Power Sources* 301 (2016), pp. 277–286. DOI: 10.1016/j.jpowsour.2015.10.011.

[48] K. Lim, H. A. Bastawrous, V.-H. Duong, K. W. See, P. Zhang, and S. X. Dou. "Fading Kalman filter-based real-time state of charge estimation in LiFePO4 battery-powered electric vehicles". In: *Appl. Energy.* 169 (2016), pp. 40–48. DOI: 10.1016/j.apenergy.2016.01.096.

[49] Y. Wang, C. Zhang, and Z. Chen. "An adaptive remaining energy prediction approach for lithium-ion batteries in electric vehicles". In: *J. Power Sources* 305 (2016), pp. 80–88. DOI: 10.1016/j.jpowsour.2015.11.087.

[50] D. V. Do, C. Forgez, El Kadri Benkara, K., and G. Friedrich. "Impedance Observer for a Li-Ion Battery Using Kalman Filter". In: *IEEE T Veh Technol* 58.8 (2009), pp. 3930–3937. DOI: 10.1109/TVT.2009.2028572.

[51] J. T. B. A. Kessels, B. Rosca, H. J. Bergveld, and van den Bosch,P. P. J. "On-line battery identification for electric driving range prediction". In: *Vehicle Power and Propulsion Conference* (2011), pp. 1–6. DOI: 10.1109/VPPC.2011.6043022.

[52] H. Dai, X. Wei, Z. Sun, J. Wang, and W. Gu. "Online cell SOC estimation of Li-ion battery packs using a dual time-scale Kalman filtering for EV applications". In: *Appl. Energy.* 95 (2012), pp. 227–237. DOI: 10.1016/j.apenergy.2012.02.044.

[53] C. Zhang, J. Jiang, W. Zhang, and S. M. Sharkh. "Estimation of State of Charge of Lithium-Ion Batteries Used in HEV Using Robust Extended Kalman Filtering". In: *Energies* 5.12 (2012), pp. 1098–1115. DOI: 10.3390/en5041098.

[54] D. Andre, C. Appel, T. Soczka-Guth, and D. U. Sauer. "Advanced mathematical methods of SOC and SOH estimation for lithium-ion batteries". In: *J. Power Sources* 224 (2013), pp. 20–27. DOI: 10.1016/j.jpowsour.2012.10.001.

[55] J. Li, J. Klee Barillas, C. Guenther, and M. A. Danzer. "A comparative study of state of charge estimation algorithms for LiFePO4 batteries used in electric vehicles". In: *J. Power Sources* 230 (2013), pp. 244–250. DOI: 10.1016/j.jpowsour.2012.12.057.

[56] R. Xiong, X. Gong, C. C. Mi, and F. Sun. "A robust state-of-charge estimator for multiple types of lithium-ion batteries using adaptive extended Kalman filter". In: *J. Power Sources* 243 (2013), pp. 805–816. DOI: 10.1016/j.jpowsour.2013.06.076.

[57] S. Sepasi, R. Ghorbani, and B. Y. Liaw. “A novel on-board state-of-charge estimation method for aged Li-ion batteries based on model adaptive extended Kalman filter”. In: *J. Power Sources* 245 (2014), pp. 337–344. DOI: 10.1016/j.jpowsour.2013.06.108.

[58] S. Sepasi, R. Ghorbani, and B. Y. Liaw. “Improved extended Kalman filter for state of charge estimation of battery pack”. In: *J. Power Sources* 255 (2014), pp. 368–376. DOI: 10.1016/j.jpowsour.2013.12.093.

[59] A. Singh, A. Izadian, and S. Anwar. “Model based condition monitoring in lithium-ion batteries”. In: *J. Power Sources* 268 (2014), pp. 459–468. DOI: 10.1016/j.jpowsour.2014.06.052.

[60] Y. Tian, B. Xia, M. Wang, W. Sun, and Z. Xu. “Comparison Study on Two Model-Based Adaptive Algorithms for SOC Estimation of Lithium-Ion Batteries in Electric Vehicles”. In: *Energies* 7.12 (2014), pp. 8446–8464. DOI: 10.3390/en7128446.

[61] Di Li, J. Ouyang, H. Li, and J. Wan. “State of charge estimation for LiMn2O4 power battery based on strong tracking sigma point Kalman filter”. In: *J. Power Sources* 279 (2015), pp. 439–449. DOI: 10.1016/j.jpowsour.2015.01.002.

[62] S. Tong, M. P. Klein, and J. W. Park. “On-line optimization of battery open circuit voltage for improved state-of-charge and state-of-health estimation”. In: *J. Power Sources* 293 (2015), pp. 416–428. DOI: 10.1016/j.jpowsour.2015.03.157.

[63] B. Xia, H. Wang, Y. Tian, M. Wang, W. Sun, and Z. Xu. “State of Charge Estimation of Lithium-Ion Batteries Using an Adaptive Cubature Kalman Filter”. In: *Energies* 8.6 (2015), pp. 5916–5936. DOI: 10.3390/en8065916.

[64] B. Fridholm, T. Wik, and M. Nilsson. “Robust recursive impedance estimation for automotive lithium-ion batteries”. In: *J. Power Sources* 304 (2016), pp. 33–41. DOI: 10.1016/j.jpowsour.2015.11.033.

[65] M. A. Roscher and D. U. Sauer. “Dynamic electric behavior and open-circuit-voltage modeling of LiFePO4-based lithium ion secondary batteries”. In: *J. Power Sources* 196.1 (2011), pp. 331–336. DOI: 10.1016/j.jpowsour.2010.06.098.

[66] X. Hu, S. Li, and H. Peng. “A comparative study of equivalent circuit models for Li-ion batteries”. In: *J. Power Sources* 198 (2012), pp. 359–367. DOI: 10.1016/j.jpowsour.2011.10.013.

[67] Rudolph van der Merwe. “Sigma-Point Kalman Filters for Probabilistic Inference in Dynamic State-Space Models”. PhD thesis. Oregon: Oregon Health & Science University, 2004.

[68] G. L. Plett. “Sigma-point Kalman filtering for battery management systems of LiPB-based HEV battery packs Part 1: Introduction and state estimation”. In: *J. Power Sources* 161.2 (2006), pp. 1356–1368. DOI: 10.1016/j.jpowsour.2006.06.003.

[69] Y. Tian, B. Xia, W. Sun, Z. Xu, and W. Zheng. “A modified model based state of charge estimation of power lithium-ion batteries using unscented Kalman filter”. In: *J. Power Sources* 270 (2014), pp. 619–626. DOI: 10.1016/j.jpowsour.2014.07.143.

[70] E. A. Wan and van der Merwe, Rudolph. “The unscented Kalman Filter”. In: *Kalman filtering and neural networks*. Ed. by S. S. Haykin. Adaptive and learning systems for signal processing, communications, and control. New York: Wiley, 2001, pp. 221–280.

[71] Y. Xing, W. He, M. Pecht, and K. L. Tsui. “State of charge estimation of lithium-ion batteries using the open-circuit voltage at various ambient temperatures”. In: *Appl. Energy.* 113 (2014), pp. 106–115. DOI: 10.1016/j.apenergy.2013.07.008.

[72] X. Zheng and H. Fang. “An integrated unscented kalman filter and relevance vector regression approach for lithium-ion battery remaining useful life and short-term capacity prediction”. In: *Rliab eng syst safe* 144 (2015), pp. 74–82. DOI: 10.1016/j.ress.2015.07.013.

[73] J. Remmlinger, M. Buchholz, T. Soczka-Guth, and K. Dietmayer. “On-board state-of-health monitoring of lithium-ion batteries using linear parameter-varying models”. In: *J. Power Sources* 239 (2013), pp. 689–695. DOI: 10.1016/j.jpowsour.2012.11.102.

[74] M.-A. Beyer. “Methodische Evaluierung von wahrscheinlichkeitstheoretischen Inferenzverfahren für dynamische Systeme”. PhD thesis. Bochum: Ruhr-Universität, 2008.

[75] E. A. Wan and Van Der Merwe, R. “The unscented Kalman filter for nonlinear estimation”. In: *Adaptive Systems for Signal Processing, Communications, and Control Symposium 2000. AS-SPCC. The IEEE 2000* (2000), pp. 153–158. DOI: 10.1109/ASSPCC.2000.882463.

[76] Y. He, W. Liu, and B. J. Koch. “Battery algorithm verification and development using hardware-in-the-loop testing”. In: *J. Power Sources* 195.9 (2010), pp. 2969–2974. DOI: 10.1016/j.jpowsour.2009.11.036.

[77] E. A. Wan and A. T. Nelson. “Dual extended Kalman Filter methods”. In: *Kalman filtering and neural networks*. Ed. by S. S. Haykin. Adaptive and learning systems for signal processing, communications, and control. New York: Wiley, 2001, pp. 123–172.

[78] X. Liu, Y. He, and Z. Chen. “State-of-Charge Estimation for Power Li-ion Battery Pack Using Vmin-EKF”. In: *2nd International Conference on Software Engineering and Data Mining*. 2010, pp. 27–31.

[79] M. Saha, B. Goswami, and R. Ghosh. “Two novel metrics for determining the tuning parameters of the Kalman Filter”. In: *Conference Proceedings of Advances in Control and Optimization of Dynamic Systems*. 2012.

[80] S. Schwunk, N. Armbruster, S. Straub, J. Kehl, and M. Vetter. “Particle filter for state of charge and state of health estimation for lithium–iron phosphate batteries”. In: *J. Power Sources* 239 (2013), pp. 705–710. DOI: 10.1016/j.jpowsour.2012.10.058.

[81] L. Kang, X. Zhao, and J. Ma. “A new neural network model for the state-of-charge estimation in the battery degradation process”. In: *Appl. Energy.* 121 (2014), pp. 20–27. DOI: 10.1016/j.apenergy.2014.01.066.

[82] V. V. Viswanathan, D. Choi, D. Wang, W. Xu, S. Towne, R. E. Williford, J.-G. Zhang, J. Liu, and Z. Yang. “Effect of entropy change of lithium intercalation in cathodes and anodes on Li-ion battery thermal management”. In: *J. Power Sources* 195.11 (2010), pp. 3720–3729. DOI: 10.1016/j.jpowsour.2009.11.103.

[83] B. Pattipati, B. Balasingam, G. V. Avvari, K. R. Pattipati, and Y. Bar-Shalom. “Open circuit voltage characterization of lithium-ion batteries”. In: *J. Power Sources* 269 (2014), pp. 317–333. DOI: 10.1016/j.jpowsour.2014.06.152.

[84] I.-S. Kim. “The novel state of charge estimation method for lithium battery using sliding mode observer”. In: *J. Power Sources* 163.1 (2006), pp. 584–590. DOI: 10.1016/j.jpowsour.2006.09.006.

[85] F. Zheng, Y. Xing, J. Jiang, B. Sun, J. Kim, and M. Pecht. “Influence of different open circuit voltage tests on state of charge online estimation for lithium-ion batteries”. In: *Appl. Energy.* 183 (2016), pp. 513–525. DOI: 10.1016/j.apenergy.2016.09.010.

[86] T.-H. Kim, J.-S. Park, S. K. Chang, S. Choi, J. H. Ryu, and H.-K. Song. “The Current Move of Lithium Ion Batteries Towards the Next Phase”. In: *Adv. Energy Mater.* 2.7 (2012), pp. 860–872. DOI: 10.1002/aenm.201200028.

[87] X. Zhang, Y. Wang, D. Yang, and Z. Chen. “An on-line estimation of battery pack parameters and state-of-charge using dual filters based on pack model”. In: *Energy* 115 (2016), pp. 219–229. DOI: 10.1016/j.energy.2016.08.109.

[88] J. Wei, G. Dong, Z. Chen, and Y. Kang. “System state estimation and optimal energy control framework for multicell lithium-ion battery system”. In: 187 (2017), pp. 37–49. DOI: 10.1016/j.apenergy.2016.11.057.

[89] M. Kassem, J. Bernard, R. Revel, S. Pélissier, F. Duclaud, and C. Delacourt. “Calendar aging of a graphite/LiFePO4 cell”. In: *J. Power Sources* 208 (2012), pp. 296–305. DOI: 10.1016/j.jpowsour.2012.02.068.

[90] J. Zhou and P. Notten. “Studies on the degradation of Li-ion batteries by the use of microreference electrodes”. In: *J. Power Sources* 177.2 (2008), pp. 553–560. DOI: 10.1016/j.jpowsour.2007.11.032.

[91] S. Grolleau, A. Delaille, H. Gualous, P. Gyan, R. Revel, J. Bernard, E. Redondo-Iglesias, and J. Peter. “Calendar aging of commercial graphite/LiFePO4 cell – Predicting capacity fade under time dependent storage conditions”. In: *J. Power Sources* 255 (2014), pp. 450–458. DOI: 10.1016/j.jpowsour.2013.11.098.

[92] B. Stiaszny, J. C. Ziegler, E. E. Krauß, M. Zhang, J. P. Schmidt, and E. Ivers-Tiffée. "Electrochemical characterization and post-mortem analysis of aged LiMn2O4 – NMC/graphite lithium ion batteries part II: Calendar aging". In: *J. Power Sources* 258 (2014), pp. 61–75. DOI: 10.1016/j.jpowsour.2014.02.019.

[93] J. C. Burns, A. Kassam, N. N. Sinha, L. E. Downie, L. Solnickova, B. M. Way, and J. R. Dahn. "Predicting and Extending the Lifetime of Li-Ion Batteries". In: *J. Electrochem. Soc.* 160.9 (2013), A1451–A1456. DOI: 10.1149/2.060309jes.

[94] J. Wang, J. Purewal, P. Liu, J. Hicks-Garner, S. Soukazian, E. Sherman, A. Sorenson, L. Vu, H. Tataria, and M. W. Verbrugge. "Degradation of lithium ion batteries employing graphite negatives and nickel–cobalt–manganese oxide + spinel manganese oxide positives: Part 1, aging mechanisms and life estimation". In: *J. Power Sources* 269 (2014), pp. 937–948. DOI: 10.1016/j.jpowsour.2014.07.030.

[95] E. Sarasketa-Zabala, F. Aguesse, I. Villarreal, L. M. Rodriguez-Martinez, C. M. López, and P. Kubiak. "Understanding Lithium Inventory Loss and Sudden Performance Fade in Cylindrical Cells during Cycling with Deep-Discharge Steps". In: *J. Phys. Chem. C* 119.2 (2015), pp. 896–906. DOI: 10.1021/jp510071d.

[96] M. Ouyang, Z. Chu, L. Lu, J. Li, X. Han, X. Feng, and G. Liu. "Low temperature aging mechanism identification and lithium deposition in a large format lithium iron phosphate battery for different charge profiles". In: *J. Power Sources* 286 (2015), pp. 309–320. DOI: 10.1016/j.jpowsour.2015.03.178.

[97] E. Sarasketa-Zabala, I. Gandiaga, E. Martinez-Laserna, L. M. Rodriguez-Martinez, and I. Villarreal. "Cycle ageing analysis of a LiFePO4/graphite cell with dynamic model validations: Towards realistic lifetime predictions". In: *J. Power Sources* 275 (2015), pp. 573–587. DOI: 10.1016/j.jpowsour.2014.10.153.

[98] F. Lin, I. M. Markus, D. Nordlund, T.-C. Weng, M. D. Asta, H. L. Xin, and M. M. Doeff. "Surface reconstruction and chemical evolution of stoichiometric layered cathode materials for lithium-ion batteries". In: *Nat Commun* 5 (2014), p. 3529. DOI: 10.1038/ncomms4529.

[99] T. Waldmann, M. Wilka, M. Kasper, M. Fleischhammer, and M. Wohlfahrt-Mehrens. "Temperature dependent ageing mechanisms in Lithium-ion batteries – A Post-Mortem study". In: *J. Power Sources* 262 (2014), pp. 129–135. DOI: 10.1016/j.jpowsour.2014.03.112.

[100] M. Ecker, N. Nieto, S. Käbitz, J. Schmalstieg, H. Blanke, A. Warnecke, and D. U. Sauer. "Calendar and cycle life study of Li(NiMnCo)O2-based 18650 lithium-ion batteries". In: *J. Power Sources* 248 (2014), pp. 839–851. DOI: 10.1016/j.jpowsour.2013.09.143.

[101] S. F. Schuster, T. Bach, E. Fleder, J. Müller, M. Brand, G. Sextl, and A. Jossen. "Nonlinear aging characteristics of lithium-ion cells under different operational conditions". In: *J. Energy Storage* 1 (2015), pp. 44–53. DOI: 10.1016/j.est.2015.05.003.

[102] R. Wright, J. Christophersen, C. Motloch, J. Belt, C. Ho, V. Battaglia, J. Barnes, T. Duong, and R. Sutula. “Power fade and capacity fade resulting from cycle-life testing of Advanced Technology Development Program lithium-ion batteries”. In: *J. Power Sources* 119-121 (2003), pp. 865–869. DOI: 10.1016/S0378-7753(03)00190-3.

[103] M. Shikano, H. Kobayashi, S. Koike, H. Sakaebe, Y. Saito, H. Hori, H. Kageyama, and K. Tatsumi. “X-ray absorption near-edge structure study on positive electrodes of degraded lithium-ion battery”. In: *J. Power Sources* 196.16 (2011), pp. 6881–6883. DOI: 10.1016/j.jpowsour.2011.01.042.

[104] M. K. Rahman and Y. Saito. “Investigation of positive electrodes after cycle testing of high-power Li-ion battery cells”. In: *J. Power Sources* 174.2 (2007), pp. 889–894. DOI: 10.1016/j.jpowsour.2007.06.222.

[105] N. Dupré, J.-F. Martin, J. Oliveri, P. Soudan, A. Yamada, R. Kanno, and D. Guyomard. “Relationship between surface chemistry and electrochemical behavior of LiNi1/2Mn1/2O2 positive electrode in a lithium-ion battery”. In: *J. Power Sources* 196.10 (2011), pp. 4791–4800. DOI: 10.1016/j.jpowsour.2010.07.049.

[106] J. Vetter, P. Novák, M. R. Wagner, C. Veit, K.-C. Möller, J. O. Besenhard, M. Winter, M. Wohlfahrt-Mehrens, C. Vogler, and A. Hammouche. “Ageing mechanisms in lithium-ion batteries”. In: *J. Power Sources* 147.1-2 (2005), pp. 269–281. DOI: 10.1016/j.jpowsour.2005.01.006.

[107] S.-P. Kim, Duin, Adri C.T. van, and V. B. Shenoy. “Effect of electrolytes on the structure and evolution of the solid electrolyte interphase (SEI) in Li-ion batteries: A molecular dynamics study”. In: *J. Power Sources* 196.20 (2011), pp. 8590–8597. DOI: 10.1016/j.jpowsour.2011.05.061.

[108] J. Schmalstieg, S. Käbitz, M. Ecker, and D. U. Sauer. “A holistic aging model for Li(NiMnCo)O2 based 18650 lithium-ion batteries”. In: *J. Power Sources* 257 (2014), pp. 325–334. DOI: 10.1016/j.jpowsour.2014.02.012.

[109] M. Broussely, P. Biensan, F. Bonhomme, P. Blanchard, S. Herreyre, K. Nechev, and R. J. Staniewicz. “Main aging mechanisms in Li ion batteries”. In: *J. Power Sources* 146.1-2 (2005), pp. 90–96. DOI: 10.1016/j.jpowsour.2005.03.172.

[110] H. J. Ploehn, P. Ramadass, and R. E. White. “Solvent Diffusion Model for Aging of Lithium-Ion Battery Cells”. In: *J. Electrochem. Soc.* 151.3 (2004), A456. DOI: 10.1149/1.1644601.

[111] P. Röder, B. Stiaszny, J. C. Ziegler, N. Baba, P. Lagaly, and H.-D. Wiemhöfer. “The impact of calendar aging on the thermal stability of a LiMn2O4–Li(Ni1 / 3Mn1 / 3Co1 / 3)O2/graphite lithium-ion cell”. In: *J. Power Sources* 268 (2014), pp. 315–325. DOI: 10.1016/j.jpowsour.2014.06.040.

[112] E. Sarasketa-Zabala, I. Gandiaga, L. M. Rodriguez-Martinez, and I. Villarreal. "Calendar ageing analysis of a LiFePO4/graphite cell with dynamic model validations: Towards realistic lifetime predictions". In: *J. Power Sources* 272 (2014), pp. 45–57. DOI: 10.1016/j.jpowsour.2014.08.051.

[113] S. F. Schuster. "Reuse of Automotive Lithium-Ion Batteries: An Assessment from the Cell Aging Perspective". PhD thesis. München: Technische Universität München, 2016.

[114] V. Zinth, C. von Lüders, M. Hofmann, J. Hattendorff, I. Buchberger, S. Erhard, J. Rebelo-Kornmeier, A. Jossen, and R. Gilles. "Lithium plating in lithium-ion batteries at sub-ambient temperatures investigated by in situ neutron diffraction". In: *J. Power Sources* 271 (2014), pp. 152–159. DOI: 10.1016/j.jpowsour.2014.07.168.

[115] M. Wohlfahrt-Mehrens, C. Vogler, and J. Garche. "Aging mechanisms of lithium cathode materials". In: *J. Power Sources* 127.1-2 (2004), pp. 58–64. DOI: 10.1016/j.jpowsour.2003.09.034.

[116] L. Lavigne, J. Sabatier, J. M. Francisco, F. Guillemard, and A. Noury. "Lithium-ion Open Circuit Voltage (OCV) curve modelling and its ageing adjustment". In: *J. Power Sources* 324 (2016), pp. 694–703. DOI: 10.1016/j.jpowsour.2016.05.121.

[117] M. A. Roscher, O. Bohlen, and J. Vetter. "OCV Hysteresis in Li-Ion Batteries including Two-Phase Transition Materials". In: *International Journal of Electrochemistry* 2011.9 (2011), pp. 1–6. DOI: 10.4061/2011/984320.

[118] M. A. Roscher, J. Assfalg, and O. S. Bohlen. "Detection of Utilizable Capacity Deterioration in Battery Systems". In: *IEEE Trans. Veh. Technol.* 60.1 (2011), pp. 98–103. DOI: 10.1109/TVT.2010.2090370.

[119] J. P. Schmidt, H. Y. Tran, J. Richter, E. Ivers-Tiffée, and M. Wohlfahrt-Mehrens. "Analysis and prediction of the open circuit potential of lithium-ion cells". In: *J. Power Sources* 239 (2013), pp. 696–704. DOI: 10.1016/j.jpowsour.2012.11.101.

[120] P. Arora. "Capacity Fade Mechanisms and Side Reactions in Lithium-Ion Batteries". In: *J. Electrochem. Soc.* 145.10 (1998), p. 3647. DOI: 10.1149/1.1838857.

[121] C. Weng, J. Sun, and H. Peng. "A unified open-circuit-voltage model of lithium-ion batteries for state-of-charge estimation and state-of-health monitoring". In: *J. Power Sources* 258 (2014), pp. 228–237. DOI: 10.1016/j.jpowsour.2014.02.026.

[122] M. Dubarry, N. Vuillaume, and B. Y. Liaw. "From single cell model to battery pack simulation for Li-ion batteries". In: *J. Power Sources* 186.2 (2009), pp. 500–507. DOI: 10.1016/j.jpowsour.2008.10.051.

[123] P. Keil and A. Jossen. "Calendar Aging of NCA Lithium-Ion Batteries Investigated by Differential Voltage Analysis and Coulomb Tracking". In: *J. Electrochem. Soc.* 164.1 (2016), A6066–A6074. DOI: 10.1149/2.0091701jes.

[124] P. Keil, S. F. Schuster, J. Wilhelm, J. Travi, A. Hauser, R. C. Karl, and A. Jossen. "Calendar Aging of Lithium-Ion Batteries". In: *J. Electrochem. Soc.* 163.9 (2016), A1872–A1880. DOI: 10.1149/2.0411609jes.

[125] C. Weng, Y. Cui, J. Sun, and H. Peng. "On-board state of health monitoring of lithium-ion batteries using incremental capacity analysis with support vector regression". In: *J. Power Sources* 235 (2013), pp. 36–44. DOI: 10.1016/j.jpowsour.2013.02.012.

[126] V. Pop, H. J. Bergveld, P. P. L. Regtien, J. H. G. Op het Veld, D. Danilov, and P. H. L. Notten. "Battery Aging and Its Influence on the Electromotive Force". In: *J. Electrochem. Soc.* 154.8 (2007), A744. DOI: 10.1149/1.2742296.

[127] S. Wang, J. Wang, L. Vu, J. Purewal, S. Soukiazian, and J. Graetz. "On Line Battery Capacity Estimation Based on Half-Cell Open Circuit Voltages". In: *J. Electrochem. Soc.* 161.12 (2014), A1788–A1793. DOI: 10.1149/2.0271412jes.

[128] S. Paul, C. Diegelmann, H. Kabza, and W. Tillmetz. "Analysis of ageing inhomogeneities in lithium-ion battery systems". In: *J. Power Sources* 239 (2013), pp. 642–650. DOI: 10.1016/j.jpowsour.2013.01.068.

[129] T. Baumhöfer, M. Brühl, S. Rothgang, and D. U. Sauer. "Production caused variation in capacity aging trend and correlation to initial cell performance". In: *J. Power Sources* 247 (2014), pp. 332–338. DOI: 10.1016/j.jpowsour.2013.08.108.

[130] Y. Zheng, M. Ouyang, L. Lu, and J. Li. "Understanding aging mechanisms in lithium-ion battery packs: From cell capacity loss to pack capacity evolution". In: *J. Power Sources* 278 (2015), pp. 287–295. DOI: 10.1016/j.jpowsour.2014.12.105.

[131] M. Dubarry, C. Truchot, A. Devie, and B. Y. Liaw. "State-of-Charge Determination in Lithium-Ion Battery Packs Based on Two-Point Measurements in Life". In: *J. Electrochem. Soc.* 162.6 (2015), A877–A884. DOI: 10.1149/2.0201506jes.

[132] S. F. Schuster, M. J. Brand, P. Berg, M. Gleissenberger, and A. Jossen. "Lithium-ion cell-to-cell variation during battery electric vehicle operation". In: *J. Power Sources* 297 (2015), pp. 242–251. DOI: 10.1016/j.jpowsour.2015.08.001.

[133] S. Santhanagopalan and R. E. White. "Quantifying Cell-to-Cell Variations in Lithium Ion Batteries". In: *International Journal of Electrochemistry* 2012.12 (2012), pp. 1–10. DOI: 10.1155/2012/395838.

[134] B. Kenney, K. Darcovich, D. D. MacNeil, and I. J. Davidson. "Modelling the impact of variations in electrode manufacturing on lithium-ion battery modules". In: *J. Power Sources* 213 (2012), pp. 391–401. DOI: 10.1016/j.jpowsour.2012.03.065.

[135] M. J. Brand, P. A. Schmidt, M. F. Zaeh, and A. Jossen. "Welding techniques for battery cells and resulting electrical contact resistances". In: *J. Energy Storage* 1 (2015), pp. 7–14. DOI: 10.1016/j.est.2015.04.001.

[136] M. Dubarry, N. Vuillaume, and B. Y. Liaw. “Origins and accommodation of cell variations in Li-ion battery pack modeling”. In: *Int. J. Energy Res.* 34.2 (2010), pp. 216–231. DOI: 10.1002/er.1668.

[137] C. T. Love, M. B. Virji, R. E. Rocheleau, and K. E. Swider-Lyons. “State-of-health monitoring of 18650 4S packs with a single-point impedance diagnostic”. In: *J. Power Sources* 266 (2014), pp. 512–519. DOI: 10.1016/j.jpowsour.2014.05.033.

[138] R. Gogoana, M. B. Pinson, M. Z. Bazant, and S. E. Sarma. “Internal resistance matching for parallel-connected lithium-ion cells and impacts on battery pack cycle life”. In: *J. Power Sources* 252 (2014), pp. 8–13. DOI: 10.1016/j.jpowsour.2013.11.101.

[139] A. Nyman, T. G. Zavalis, R. Elger, M. Behm, and G. Lindbergh. “Analysis of the Polarization in a Li-Ion Battery Cell by Numerical Simulations”. In: *J. Electrochem. Soc.* 157.11 (2010), A1236. DOI: 10.1149/1.3486161.

[140] J. Gomez, R. Nelson, E. E. Kalu, M. H. Weatherspoon, and J. P. Zheng. “Equivalent circuit model parameters of a high-power Li-ion battery: Thermal and state of charge effects”. In: *J. Power Sources* 196.10 (2011), pp. 4826–4831. DOI: 10.1016/j.jpowsour.2010.12.107.

[141] C. Campestrini, M. F. Horsche, I. Zilberman, T. Heil, T. Zimmermann, and A. Jossen. “Validation and benchmark methods for battery management system functionalities: State of charge estimation algorithms”. In: *J. Energy Storage* 7 (2016), pp. 38–51. DOI: 10.1016/j.est.2016.05.007.

[142] C. Fleischer, W. Waag, H.-M. Heyn, and D. U. Sauer. “On-line adaptive battery impedance parameter and state estimation considering physical principles in reduced order equivalent circuit battery models”. In: *J. Power Sources* 260 (2014), pp. 276–291. DOI: 10.1016/j.jpowsour.2014.01.129.

[143] S. Seki, N. Kihira, Y. Mita, T. Kobayashi, K. Takei, T. Ikeya, H. Miyashiro, and N. Terada. “AC Impedance Study of High-Power Lithium-Ion Secondary Batteries—Effect of Battery Size”. In: *J. Electrochem. Soc.* 158.2 (2011), A163. DOI: 10.1149/1.3525277.

[144] H. Dai, T. Xu, L. Zhu, X. Wei, and Z. Sun. “Adaptive model parameter identification for large capacity Li-ion batteries on separated time scales”. In: 184 (2016), pp. 119–131. DOI: 10.1016/j.apenergy.2016.10.020.

[145] B. V. Ratnakumar, M. C. Smart, L. D. Whitcanack, and R. C. Ewell. “The impedance characteristics of Mars Exploration Rover Li-ion batteries”. In: *J. Power Sources* 159.2 (2006), pp. 1428–1439. DOI: 10.1016/j.jpowsour.2005.11.085.

[146] D. Andre, M. Meiler, K. Steiner, C. Wimmer, T. Soczka-Guth, and D. U. Sauer. “Characterization of high-power lithium-ion batteries by electrochemical impedance spectroscopy. I. Experimental investigation”. In: *J. Power Sources* 196.12 (2011), pp. 5334–5341. DOI: 10.1016/j.jpowsour.2010.12.102.

[147] S. Buller, M. Thele, R. W. de doncker, and E. Karden. “Supercapacitors and lithium-ion batteries for power electronic applications”. In: *IEEE Ind Appl Mag* 11.2 (2005), pp. 742–747. DOI: 10.1109/MIA.2005.1405828.

[148] A. Jossen and W. Weydanz. *Moderne Akkumulatoren richtig einsetzen: 36 Tabellen.* 1st ed. Neusäß: Ubooks, 2006.

[149] S. Jung. “Mathematical model of lithium-ion batteries with blended-electrode system”. In: *J. Power Sources* 264 (2014), pp. 184–194. DOI: 10.1016/j.jpowsour.2014.04.072.

[150] M. Petzl and M. A. Danzer. “Advancements in OCV Measurement and Analysis for Lithium-Ion Batteries”. In: *IEEE T Energy Conver* 28.3 (2013), pp. 675–681. DOI: 10.1109/TEC.2013.2259490.

[151] A. Barai, W. D. Widanage, J. Marco, A. McGordon, and P. Jennings. “A study of the open circuit voltage characterization technique and hysteresis assessment of lithium-ion cells”. In: *J. Power Sources* 295 (2015), pp. 99–107. DOI: 10.1016/j.jpowsour.2015.06.140.

[152] F. M. Kindermann, A. Noel, S. V. Erhard, and A. Jossen. “Long-term equalization effects in Li-ion batteries due to local state of charge inhomogeneities and their impact on impedance measurements”. In: *Electrochim. Acta* 185 (2015), pp. 107–116. DOI: 10.1016/j.electacta.2015.10.108.

[153] G. Dong, J. Wei, C. Zhang, and Z. Chen. “Online state of charge estimation and open circuit voltage hysteresis modeling of LiFePO4 battery using invariant imbedding method”. In: *Appl. Energy.* 162 (2016), pp. 163–171. DOI: 10.1016/j.apenergy.2015.10.092.

[154] A. Farmann and D. U. Sauer. “A study on the dependency of the open-circuit voltage on temperature and actual aging state of lithium-ion batteries”. In: *J. Power Sources* 347 (2017), pp. 1–13. DOI: 10.1016/j.jpowsour.2017.01.098.

[155] M. Dubarry and B. Y. Liaw. “Development of a universal modeling tool for rechargeable lithium batteries”. In: *J. Power Sources* 174.2 (2007), pp. 856–860. DOI: 10.1016/j.jpowsour.2007.06.157.

[156] S. Nejad, D. T. Gladwin, and D. A. Stone. “A systematic review of lumped-parameter equivalent circuit models for real-time estimation of lithium-ion battery states”. In: *J. Power Sources* 316 (2016), pp. 183–196. DOI: 10.1016/j.jpowsour.2016.03.042.

[157] P. L. Moss, G. Au, E. J. Plichta, and J. P. Zheng. “An Electrical Circuit for Modeling the Dynamic Response of Li-Ion Polymer Batteries”. In: *J. Electrochem. Soc.* 155.12 (2008), A986. DOI: 10.1149/1.2999375.

[158] M. Ecker, J. B. Gerschler, J. Vogel, S. Käbitz, F. Hust, P. Dechent, and D. U. Sauer. "Development of a lifetime prediction model for lithium-ion batteries based on extended accelerated aging test data". In: *J. Power Sources* 215 (2012), pp. 248–257. DOI: 10.1016/j.jpowsour.2012.05.012.

[159] S. S. Haykin, ed. *Kalman filtering and neural networks*. Adaptive and learning systems for signal processing, communications, and control. New York: Wiley, 2001.

[160] G. Pérez, M. Garmendia, J. F. Reynaud, J. Crego, and U. Viscarret. "Enhanced closed loop State of Charge estimator for lithium-ion batteries based on Extended Kalman Filter". In: *Appl. Energy.* 155 (2015), pp. 834–845. DOI: 10.1016/j.apenergy.2015.06.063.

[161] D. Simon. *Optimal state estimation: Kalman, H [infinity] and nonlinear approaches*. Hoboken and N.J: Wiley-Interscience, 2006.

[162] C. Campestrini, P. Keil, S. F. Schuster, and A. Jossen. "Ageing of lithium-ion battery modules with dissipative balancing compared with single-cell ageing". In: *J. Energy Storage* 6 (2016), pp. 142–152. DOI: 10.1016/j.est.2016.03.004.

[163] P. Keil and A. Jossen. "Aging of Lithium-Ion Batteries in Electric Vehicles: Impact of Regenerative Braking". In: *EVS28 - The 28th International Electric Vehicle Symposium*. Ed. by World Electric Vehicle Association. 2015. DOI: 10.13140/RG.2.1.3485.2320.

[164] T. J. Barlow. *A reference book of driving cycles for use in the measurement of road vehicle emissions: Version 3*. Vol. PPR354. Published project report. Bracknell: IHS, 2009.

[165] E. Kirchner. *Leistungsübertragung in Fahrzeuggetrieben: Grundlagen der Auslegung, Entwicklung und Validierung von Fahrzeuggetrieben und deren Komponenten*. VDI. Berlin and New York: Springer, 2007.

[166] S. Buller, M. Thele, E. Karden, and De Doncker, Rik W. "Impedance-based non-linear dynamic battery modeling for automotive applications". In: *J. Power Sources* 113.2 (2003), pp. 422–430. DOI: 10.1016/S0378-7753(02)00558-X.

[167] C. Campestrini, S. Kosch, and A. Jossen. "Influence of change in open circuit voltage on the state of charge estimation with an extended Kalman filter". In: *J. Energy Storage* 12 (2017), pp. 149–156. DOI: 10.1016/j.est.2017.04.011.

[168] Y. Zhang, C.-Y. Wang, and X. Tang. "Cycling degradation of an automotive LiFePO4 lithium-ion battery". In: 196.3 (2011), pp. 1513–1520. DOI: 10.1016/j.jpowsour.2010.08.070.

[169] X. Zhang, Y. Wang, C. Liu, and Z. Chen. "A novel approach of remaining discharge energy prediction for large format lithium-ion battery pack". In: 343 (2017), pp. 216–225. DOI: 10.1016/j.jpowsour.2017.01.054.

[170] I. Snihir, W. Rey, E. Verbitskiy, A. Belfadhel-Ayeb, and P. H. Notten. “Battery open-circuit voltage estimation by a method of statistical analysis”. In: *J. Power Sources* 159.2 (2006), pp. 1484–1487. DOI: 10.1016/j.jpowsour.2005.11.090.

[171] X. Dang, L. Yan, K. Xu, X. Wu, H. Jiang, and H. Sun. “Open-Circuit Voltage-Based State of Charge Estimation of Lithium-ion Battery Using Dual Neural Network Fusion Battery Model”. In: *Electrochim. Acta* 188 (2016), pp. 356–366. DOI: 10.1016/j.electacta.2015.12.001.

[172] X. Tang, Y. Wang, and Z. Chen. “A method for state-of-charge estimation of LiFePO4 batteries based on a dual-circuit state observer”. In: *J. Power Sources* 296 (2015), pp. 23–29. DOI: 10.1016/j.jpowsour.2015.07.028.

[173] A. Farmann, W. Waag, and D. U. Sauer. “Adaptive approach for on-board impedance parameters and voltage estimation of lithium-ion batteries in electric vehicles”. In: *J. Power Sources* 299 (2015), pp. 176–188. DOI: 10.1016/j.jpowsour.2015.08.087.

[174] C. Campestrini, T. Heil, S. Kosch, and A. Jossen. “A comparative study and review of different Kalman filters by applying an enhanced validation method”. In: *J. Energy Storage* 8 (2016), pp. 142–159. DOI: 10.1016/j.est.2016.10.004.

[175] P. Keil, C. von Lüders, and A. Jossen. “Influence of Regenerative Braking on the Aging of the Li-Ion Battery of an Electric Vehicle”. In: *CoFAT* (2014).

[176] S. Käbitz, J. B. Gerschler, M. Ecker, Y. Yurdagel, B. Emmermacher, D. André, T. Mitsch, and D. U. Sauer. “Cycle and calendar life study of a graphite | LiNi1/3Mn1/3Co1/3O2 Li-ion high energy system. Part A: Full cell characterization”. In: *J. Power Sources* 239 (2013), pp. 572–583. DOI: 10.1016/j.jpowsour.2013.03.045.

List of Figures

1.1 Tracking of a falling object: (a) altitude s; (b) velocity v; (c) altitude estimation error; (d) velocity estimation error. 2
1.2 Validation issues: (a) validation with one current sensor (CC discharge); (b) validation with an additional, more accurate, current sensor (CC discharge); (c) shortcomings of discretising and resulting error. 6
1.3 Structure of the work 12

2.1 ECM consisting of one ohmic resistance (R_i), two RC terms (R_1, C_1 and R_2, C_2) and the SOC-dependent OCV U_0 with the corresponding dependencies. U and I correspond to the terminal voltage and current, respectively. 13
2.2 Normalised and interpolated charge transfer resistance R_1 of different commercial 18650 cells (nickel-cobalt-aluminium, nickel-manganese-cobalt and lithium-iron-phosphate) cell at 25 °C (normalised to their maximum value). 14
2.3 OCVs of commercial 18650 lithium-ion cells with graphite vs. different conventional cathode materials at 25 °C, measured by averaging the cell voltage of a constant current charge and discharge. 15

3.1 Calculation sequence of a Kalman filter 22

4.1 Design of the modules in 8s14p topology: (a) schematic representation which illustrates the disassembly points (dashed red lines); technical drawings in top (b) and front view (c), illustrating the positions of the temperature and voltage measurements. 28
4.2 Cell matching: (a) normal distribution of capacities at the cell level; (b) normal distribution of ohmic resistances (measured at 1 kHz) at the cell level. 30
4.3 Cell matching at 25 °C: measured and calculated capacities of (a) module 1 and (b) module 2; measured and calculated ohmic resistances (measured at 1 kHz) of (c) module 1 and (d) module 2. 31
4.4 Measurement setup on cell level 32
4.5 Scheme of the module ageing test bench: (a) cycling configuration; (b) check-up configuration. 33
4.6 US06 highway driving cycle: (a) velocity profile; (b) load current at the cell level with unrestricted regenerative braking and without regenerative braking. [163] 36

4.7 Overview of the performed experiments on cell and module level. Cell group 5 correspond to results of [163]. 38

5.1 Creating an application-independent test profile: dominant frequencies after a local peak search of the *Artemis HighMot urbdense total* driving cycle 42
5.2 Creating an application-independent test profile: the discrete profile with the corresponding sample rates (Eq. 5.2). 44
5.3 Validation profiles for a NCA cell: sequence of the validation process for each profile (1: capacity measurement and initial SOC conditioning; 2: profile A, B or C; 3: residual charge measurement; 4: capacity measurement). The variable x depends on the duration of the profiles. 44
5.4 Validation profiles for a NCA cell: profile A for low-dynamic. 45
5.5 Validation profiles for a NCA cell: profile B for high-dynamic. 46
5.6 Validation profiles for a NCA cell: one of the seven cycles of profile C for the long-term test (temperature cycle start: t_S; temperature cycle end: t_E). 46
5.7 Validation principle: evaluation of the estimation accuracy (example with profile B and error boundary ε=$\pm$0.5 %, not all boundaries shown). 47
5.8 Validation principle: (a) estimation with drift (example with profile B, not all boundaries shown); (b) linear regression of the estimation error gives the average drift error $P(\varepsilon_{1\,\mathrm{h}})$ 48
5.9 Validation principle: evaluation of the transient behaviour (example with profile B, not all boundaries shown). 50

6.1 Parameters of NCR18650PD: (a) ohmic resistance R_i and (b) $R_{\mathrm{dc1\,s}}$ (measured after a $-0.5\,\mathrm{C}$ current pulse) at different temperatures. Markers symbolise measurement points. 56
6.2 Parameters of NCR18650PD: charge transfer resistance R_1 at different current rates at (a) 0 °C and (b) 40 °C. Markers symbolise measurement points. 56
6.3 Parameters of NCR18650PD: (a) time constant τ_1 at different current rates at 0 °C. Markers symbolise measurement points; (b) interpolated temperature dependency at 10 %, 50 % and 90 % with a current rate of $-0.25\,\mathrm{C}$. 57
6.4 Validation of the two RC term ECM and parameters: (a) extract of the total simulation at 25 °C; (b) extract of the total simulation at 0 °C; (c) deviation at 25 °C; (d) deviation at 0 °C 58
6.5 Parameters of the investigated cell in three different ageing states: (a) SOC dependency of the $R_{\mathrm{dc1\,s}}$ resistance measured after one second at $-10\,^\circ\mathrm{C}$ and 40 °C; (b) temperature dependency of $R_{\mathrm{dc1\,s}}$ at a SOC of 50 %. Markers symbolise measurement points. 59
6.6 Parameters of the investigated cell in three different ageing states: temperature dependency of the actual capacity C_act determined by the CCCV discharge (Section 4.5.1). Markers symbolise measurement points. 59

6.7 Temperature and SOC dependency of a new cell: (a) CC-OCV and (b) IC-OCV (left axis) and temperature influence at the corresponding SOC (right axis). . . 60
6.8 OCV determination methods: (a) OCV in charge and discharge direction of the new and old cell at −10 °C and 40 °C measured by the incremental and constant-current method; (b) interpolated and averaged OCVs. 61
6.9 OCV determination methods: (a) OCV deviation between the IC method and the CC method of the new and old cell at −10 °C and 40 °C, (b) voltage at 100 % SOC and 0 % SOC at different temperatures and ageing states. 62

7.1 SOC estimation results and the deviation from the reference (ΔSOC) of the SKF (one RC term) with correct initialisation: (a) profile A at 40 °C; (b) profile B at 40 °C. 64
7.2 SOC estimation results and the deviation from the reference (ΔSOC) of the SKF (one RC term) with correct initialisation: (a) profile A at 0 °C; (b) profile B at 0 °C. 65
7.3 Voltage estimation results U and voltage error ΔU of the SKF (one RC term) with correct initialisation: estimated and measured voltage of profile A (during a SLC at approximately 50 % SOC) at 0 °C. 66
7.4 SOC estimation results and the deviation from the reference (ΔSOC) of the SKF (one RC term) with correct initialisation: profile C. 67
7.5 SOC estimation results and the deviation from the reference (ΔSOC) of the SKF (one RC term): (a) transient behaviour during high-dynamic discharge (first 10 % of time of profile B at 25 °C); (b) influence of an incorrect parameter ($R_{\mathrm{dc1\,s}}$, profile B at 40 °C). 68
7.6 SOC estimation results and the deviation from the reference (ΔSOC) of the SKF (one RC term): influence of a current offset on profile C. 69
7.7 Estimation score K_{est} of the SKFs with one and two RC terms at different temperatures: (a) during low-dynamic load (profile A) with the ECM initialised at 25 °C; (b) during low-dynamic load (profile A) with the ECM initialised at 10 °C; (c) during high-dynamic load (profile B) with the ECM initialised at 25 °C; (d) during high-dynamic load (profile B) with the ECM initialised at 10 °C. 70
7.8 Benchmark results of the SKF with one and two RC terms (ECM initialised at 25 °C): (a) transient behaviour K_{trans} during high-dynamic discharge (profile B) at different temperatures; (b) estimation score K_{est}, drift score K_{drift}, failure stability score K_{fail} and residual charge determination score K_{res} during the long-term test (profile C) with varying temperature. 71
7.9 Results of the DKF (one RC term) and the deviation from the reference (ΔSOC): (a) profile A at 0 °C; (b) voltage error of profile A (during a SLC at approximately 50 % SOC) at 0 °C. 71

7.10 Results of the DKF (one RC term) and the deviation from the reference (ΔSOC): influence of an incorrect parameter ($R_{\mathrm{dc1\,s}}$, profile B at 25 °C). 72
7.11 Performance change of a DKF compared to the corresponding single KF: (a) estimation score ΔK_{est} at different temperatures during low-dynamic load (profile A); (b) ΔK_{est} at different temperatures during high-dynamic load (profile B); (c) transient behaviour during high-dynamic discharge (profile B) at different temperatures $\Delta K_{\mathrm{trans}}$; (d) ΔK_{est}, drift score $\Delta K_{\mathrm{drift}}$, failure stability score ΔK_{fail} and residual charge determination score ΔK_{res} during the long-term test (profile C) with varying temperature. 73
7.12 Comparison of the $R_{\mathrm{dc1\,s}}$ estimation by the DKF with one (a) and two (b) RC terms at 0 °C and 25 °C (Profile B). 74
7.13 Net diagram with the final scores of all investigated KFs: (a) low-dynamic load (profile A); (b) high-dynamic load (profile B); (c) long-term test (profile C). . . 75
7.14 Benchmark results with correct parameters and individual filter tuning at 0 °C and 25 °C during profile B: (a) estimation score K_{est}; (b) transient behaviour K_{trans}. 76

8.1 Temperature and ageing dependency of the OCV determined by the IC method: (a) OCV of the new (Z1) and old cell (Z3) at 40 °C and 0 °C; (b) SOC error at 40 °C and 0 °C of the aged cells (Z2, Z3) based on the OCV of the new cell (Z1) at 40 °C. 80
8.2 SOC estimation results with profile B of the new cell of CG1 at 0 °C: (a) estimation with the OCV of Z1, Z2 and Z3 and the reference; (b) SOC deviation between the estimation and the reference. 81
8.3 SOC estimation results: (a) SOC deviation between the estimation with $\mathrm{OCV_{Z3}}$ and the estimation with $\mathrm{OCV_{Z3}}$ and $\mathrm{OCV_{Z3}}$ at 0 °C and at 40 °C; (b) RMS deviation $\Delta SOC_{\mathrm{OCV}}$ and $\Delta SOC_{\mathrm{Est}}$ in the investigated temperature range. . . 82
8.4 SOC estimation results with changed filter tuning: (a) SOC deviation between the estimation with $\mathrm{OCV_{Z3}}$ and the estimation with $\mathrm{OCV_{Z3}}$ and $\mathrm{OCV_{Z3}}$ at 0 °C and 40 °C; (b) RMS deviation $\Delta SOC_{\mathrm{OCV}}$ and $\Delta SOC_{\mathrm{Est}}$ in the investigated temperature range. 83

9.1 Ageing at the cell level at low (L) and high (H) SOC at 10 °C (calendar ageing only), 25 °C and 40 °C: (a) capacity degradation during cycling ageing; (b) capacity degradation during calendar ageing; (c) resistance increase during cycling ageing; (d) resistance increase during calendar ageing. 86
9.2 Voltage difference between new and aged OCV for different temperatures and SOC levels: (a) cyclic ageing; (b) calendar ageing. 87
9.3 (a) Voltage difference between new and aged OCV: cyclic and calendar ageing at a retained capacity at approximately 90 %; (b) differential voltage analysis of aged cells: cyclic and calendar ageing at a retained capacity at approximately 90 %. 88

9.4 (a) impact of a change in OCV to the OCV–SOC relationship (left axis: OCV, right axis: SOC deviation); (b) difference of the CC-OCV and the IC-OCV method (for OCV determination see Section 4.4.2) at 25 °C at the cells EOL. . 88
9.5 Development of the SOC error between 10 % and 20 % SOC resulting from a changing OCV over lifetime: (a) vs. EFC (cyclic ageing); (b) vs. time (calendar ageing); (c) vs. actual capacity C_{act} (cyclic ageing); (d) vs. actual capacity C_{act} (calendar ageing) 89
9.6 Capacity and resistance development during cyclic ageing at 40 °C: a) module capacities; b) module resistances. 91
9.7 Capacity and resistance development during cyclic ageing at 40 °C: a) block capacities of module 1; b) block capacities of module 2; c) block resistances of module 1; d) block resistances of module 2. 91
9.8 Ageing at the cell level at high SOC: influence of temperature on calendar ageing. 93
9.9 Spread of parameters over the entire ageing study: α represents the inhomogeneity for the unconnected cells, β represents the inhomogeneity of the modules with coincidently selected cells, γ represents the inhomogeneity for perfectly matched modules. The remaining bars illustrate the actual inhomogeneities in the constructed modules throughout the entire ageing procedure for (a) block capacity and (b) block resistance. 94
9.10 Capacity degradation (a, b) and resistance increase (c, d) with the corresponding temperature distribution at 600 EFC and 1200 EFC (please notice the different scaling of the ΔR axis). 96
9.11 Energy efficiency 97
9.12 Ageing impact on cell balancing. 98
9.13 OCV at the EOL: (a) OCV at cell, block and module level (scaled to cell level); (b) difference between cell and block as well as cell and module. 99
9.14 (a) Voltage difference between the OCV of the new cell from CG3 and the OCV at module level (scaled) at EOL; (b) differential voltage analysis of the cell and module OCV. 99

10.1 Scheme of the correlation between temperature and age regarding the influence on the estimation performance. 107

A.1 Data-sheet of the Panasonic NCR18650PD NCA cell 133

List of Tables

2.1 SOC, temperature T, current I and ageing dependencies of the ECM elements in literature. 16

4.1 Matrix of the cyclic and calendar ageing experiments at single cell and module level. L corresponds to the low SOC level (3.7 V), H corresponds to the high SOC level (4.1 V). The green tick symbolises the amount of cells or modules per ageing condition, the red cross symbolises conditions not considered. 37
4.2 Cell history and SOH of the investigated cells (Z1, Z2 and Z3) in CG2. 39

5.1 Major time constants and sample rates for discretisation. 43
5.2 Possible relationship between K_{est} and K_{drift} 49
5.3 Benchmark categories and their requirements. 52

6.1 Comparison of the investigated SOC, temperature T, current I and ageing dependencies of the ECM elements with the literature in Section 2.1. The green tick symbolises the accordance to the literature research. 62

7.1 RMS error of the sigma point and square root KF for profile B at 25 °C 67

9.1 Regression value r of the correlation between SOC error and capacity degradation 90

B.1 Resolution and accuracy of the measurement equipment on cell level 134
B.2 Resolution and accuracy of the measurement equipment on module level 134
C.1 Parameters of the vehicle model 135
D.1 Initial tuning and ECM parameters of the filters at 25 °C 136
D.2 Actual capacity C_{act} at −10 °C, 0 °C, 10 °C, 25 °C and 40 °C. 137
D.3 Initial ECM parameters at 0 °C. 137
D.4 Changed tuning parameters at 0 °C and 25 °C. 137

Appendix

A Data-sheet of the Panasonic NCR18650PD NCA cell

TENTATIVE

High Capacity & High Power

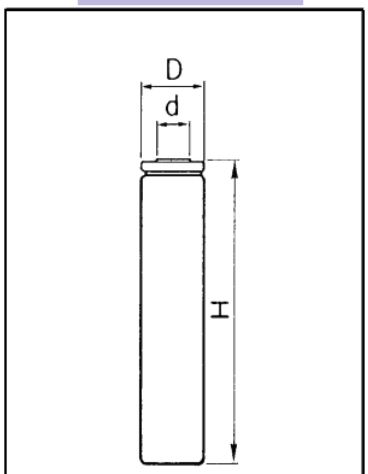

Dimensions (Max.) with tube		
	H	65.3mm
	D	18.5mm
	d	7.9 mm

Discharged State after Assembling

Cell Type NCR18650PD

Specifications

Rated Capacity	*at 20deg.C	.2680mAh
Nominal Capacity	*at 25deg.C	Min.2730mAh
		Typ.2880mAh
Nominal Voltage		3.6V
Charging Method		Constant Current -Constant Voltage
Charging Voltage		4.2V
Charging Current		Std.1365mA
Charging Time		4.0hrs.
Ambient Temperature	Charge	10～+45℃
	Discharge	-20～+60℃
	Storage	-20～+50℃
Weight (Max.)		44.5g
Volumetric Energy Density		567Wh/l
Gravimetric Energy Density		217Wh/kg

Panasonic ideas for life

Figure A.1: Data-sheet of the Panasonic NCR18650PD NCA cell

B Measurement equipment

Table B.1: Resolution and accuracy of the measurement equipment on cell level

Device	Resolution	Accuracy
CTS Voltage	0.3 mV	1 mV
CTS Current	0.2 mA	1 mA
CTS Temperature	0.01 °C	±2 °C
BMS Voltage	1.5 mV	2.5 mV
BMS Current	3 mA	±0.4 A
BMS Temperature	0.1 °C	3 °C

Table B.2: Resolution and accuracy of the measurement equipment on module level

Device	Resolution	Accuracy
HPS Voltage	1 mV	12 mV
HPS Current	1.6 mA	55 mA
BSD Voltage	1 mV	50 mV
BSD Current	1.6 mA	2.2 A
BSD Temperature	0.05 °C	2 °C
XCTS Voltage	0.3 mV	±3 mV
XCTS Current	2.5 mA	±100 mA
CMU Voltage	0.2 mV	2.5 mV
CMU Temperature	0.1 °C	3 °C
PXI Temperature	60 µ°C	0.35 °C
HIOKI BT3562	3 mΩ range: 0.1 mΩ	0.015 mΩ
	30 Ω range: 1 mΩ	0.15 Ω

C Vehicle model parameters

Table C.1: Parameters of the vehicle model

Parameter	Value
Gravitation	$9.81\,\mathrm{m/s^2}$
Density of air	$1.225\,\mathrm{kg/m^3}$
Ambient temperature	$25\,^{\circ}\mathrm{C}$
Relative ambient humidity	0.6
Vehicle mass (excluding battery)	$1200\,\mathrm{kg}$
Battery pack mass	$500\,\mathrm{kg}$
Additional mass	$150\,\mathrm{kg}$
Air drag coefficient	0.31
Vehicle frontal area	$2.24\,\mathrm{m}$
Tire roll resistance factor	0.013
Rotational mass factor	1.05
Additional consumption	$0.4\,\mathrm{W}$
Motor efficiency	$0.94\,\%$
Inverter efficiency	$0.97\,\%$
Efficiency factor transmission	$0.95\,\%$
Recuperation efficiency	$0.5\,\%$

D Kalman filter initialisation

Table D.1: Initial tuning and ECM parameters of the filters at 25 °C

Parameter		1RC	2RC
Covariance $\mathbf{P}$	U_1	10^{-12}	10^{-12}
	U_2	-	10^{-12}
	SOC	$5 \cdot 10^{-4}$	$5 \cdot 10^{-4}$
Covariance $\mathbf{P}_\theta$	$R_{\mathrm{dc1\,s}}$	10^{-5}	10^{-5}
	C_{act}	10^{-10}	10^{-10}
	R_1	10^{-5}	10^{-5}
	C_1	10^{-5}	10^{-5}
	R_2	-	10^{-5}
	C_2	-	10^{-5}
Process noise $\mathbf{Q}$	U_1	10^{-9}	10^{-9}
	U_2	-	10^{-9}
	SOC	10^{-15}	10^{-15}
Process noise $\mathbf{Q}_\theta$	$R_{\mathrm{dc1\,s}}$	10^{-9}	10^{-9}
	C_{act}	10^{-6}	10^{-6}
	R_1	10^{-9}	10^{-9}
	C_1	10^{-3}	10^{-3}
	R_2	-	10^{-9}
	C_2	-	10^{-1}
Measurement noise r	r	$5 \cdot 10^{-7}$	$5 \cdot 10^{-7}$
	r_θ	0.0013	0.0013
ECM parameter at 90 % for profile B	U_1	0 V	0 V
	U_2	-	0 V
	$R_{\mathrm{dc1\,s}}$	42.7 mΩ	42.7 mΩ
	R_1	22.8 mΩ	17.2 mΩ
	C_1	1242 F	1.9 F
	R_2	-	22.8 mΩ
	C_2	-	1230 F
ECM parameter at 50 % for profile A and C	U_1	0 V	0 V
	U_2	-	0 V
	$R_{\mathrm{dc1\,s}}$	39.5 mΩ	39.5 mΩ
	R_1	35.4 mΩ	13.8 mΩ
	C_1	958 F	2.4 F
	R_2	-	34.9 mΩ
	C_2	-	931 F
Window size AKF	ϕ	10	10
Sigma Point	λ_1	0.5	0.5
	λ_2	2	2
	λ_3	0	0
	h	$\sqrt{3}$	$\sqrt{3}$

Table D.2: Actual capacity C_{act} at −10 °C, 0 °C, 10 °C, 25 °C and 40 °C.

	−10 °C	0 °C	10 °C	25 °C	40 °C
C_{act}	2.23 A h	2.46 A h	2.72 A h	2.8 A h	2.82 A h

Table D.3: Initial ECM parameters at 0 °C.

Parameter	1RC	2RC
$R_{\text{dc1 s}}$	131.7 mΩ	131.7 mΩ
R_1	51.7 mΩ	111 mΩ
C_1	453.6 F	2.19 F
R_2	-	36.1 mΩ
C_2	-	427.1 F

Table D.4: Changed tuning parameters at 0 °C and 25 °C.

Temp.	Parameter	SLKF 2RC	SEKF 1RC	SAEKF 1RC	DEKF 1RC
0 °C	Covariance U_1	$1.4 \cdot 10^{-4}$	10^{-7}	10^{-15}	10^{-9}
	Covariance U_2	10^{-5}	-	-	-
	Covariance	$2 \cdot 10^{-2}$	$9 \cdot 10^{-3}$	10^{-2}	$7 \cdot 10^{-5}$
	Process noise U_1	10^{-5}	10^{-9}	10^{-11}	10^{-9}
	Process noise U_2	10^{-5}	-	-	-
	Process noise SOC	10^{-14}	10^{-15}	10^{-13}	10^{-17}
25 °C	Covariance U_1	$4 \cdot 10^{-7}$	10^{-12}	10^{-12}	10^{-12}
	Covariance U_2	10^{-5}	-	-	-
	Covariance	$1.5 \cdot 10^{-7}$	$5 \cdot 10^{-4}$	$5 \cdot 10^{-4}$	$5 \cdot 10^{-4}$
	Process noise U_1	10^{-9}	10^{-9}	10^{-9}	10^{-9}
	Process noise U_2	10^{-9}	-	-	-
	Process noise SOC	10^{-15}	10^{-15}	10^{-15}	10^{-15}